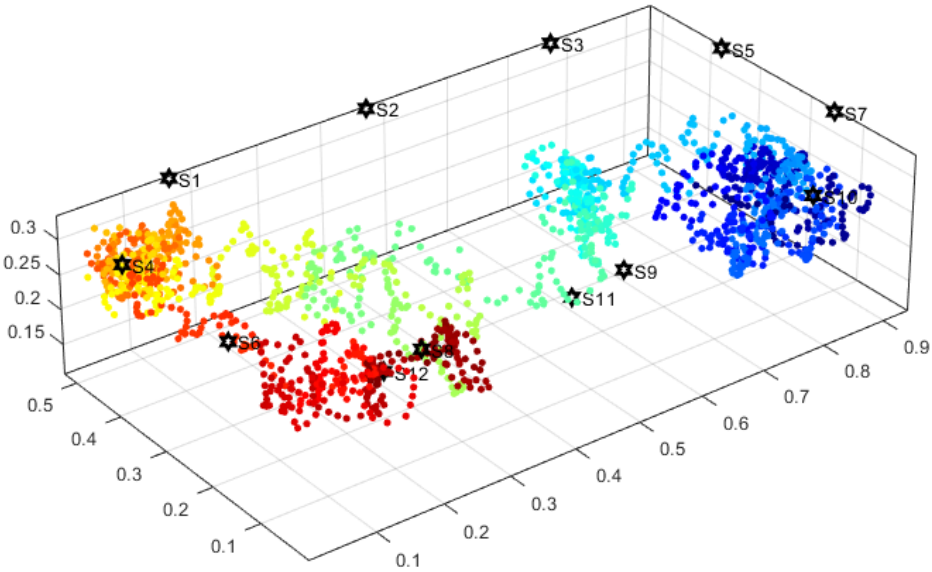

Characterization of Fuel Mixing in a Fluidized Bed Cold Model

An Experimental Study Using Magnetic Particle Tracking

Master's thesis in Innovative and Sustainable Chemical Engineering

JON AHLGREN, PONTUS WAGEBORN

DEPARTMENT OF SPACE, EARTH AND ENVIRONMENT
CHALMERS UNIVERSITY OF TECHNOLOGY
Gothenburg, Sweden 2021
www.chalmers.se

Master's thesis 2021

Characterization of Fuel Mixing in a Fluidized Bed Cold Model

An Experimental Study Using Magnetic Particle Tracking

JON AHLGREN
PONTUS WAGEBORN

Department of Space, Earth and Environment
Division of Energy Technology
Fluidization Group
Chalmers University of Technology
Gothenburg, Sweden 2021

Characterization of Fuel Mixing in a Fluidized Bed Cold Model
An Experimental Study Using Magnetic Particle Tracking
JON AHLGREN, PONTUS WAGEBORN

Supervisor: Diana Carolina Guío-Pérez
Examiner: David Pallarès

Master's Thesis 2021
Fluidization Group
Division of Energy Technology
Department of Space, Earth and Environment
Chalmers University of Technology
SE-412 96 Gothenburg
Telephone +46 31 772 1000

Cover: Visualisations of the movements of a fluidized tracer particle constructed in Matlab showing positions of the tracer during one minute at a superficial air velocity of 0.43 $\frac{m}{s}$.

Typeset in LaTeX
Printed by Chalmers Reproservice
Gothenburg, Sweden 2021

Characterization of Fuel Mixing in a Fluidized Bed Cold Model
An Experimental Study Using Magnetic Particle Tracking
JON AHLGREN, PONTUS WAGEBORN
Department of Space, Earth and Environment
Division of Energy Technology
Chalmers University of Technology

Abstract

An experimental study of the mixing of fuel particles in fluidized beds has been conducted. The study was performed using magnetic particle tracking sensors to track a magnetic tracer particle in a downscaled cold model of an industrial boiler. The fluid dynamical scaling was applied using Glicksman's simplified scaling laws. Mixing characteristics of the tracer particles were evaluated and mixing cells were studied. The lateral dispersion coefficient was calculated using Einsteins equation for Brownian motion and measuring the residence time in the mixing cells for three different bed height. This resulted in lateral dispersion coefficient values in the range of $3.3 - 7.6 \times 10^{-3}$ $\frac{m^2}{s}$ for mixing cell sizes between 0.04 and 0.08 m. Dispersion calculations based on mixing cells were performed using larger mixing cell size estimations (between 0.131 and 0.214 m), and the calculated lateral dispersion values converged towards the same values as the Brownian motion calculations when time filtering was applied. By comparing dispersion data from 20 minute and 5 minute measurements it was concluded that the shorter 5 minute measurements gave enough data to properly characterize the mixing. Movement patterns similar to mixing cells could be observed although they were disrupted by the construction of the cold model units distributor plate. No mixing cells unaffected by walls or the mentioned disruption were identified. The tracer particle did not cover the entire bed at the low bed height which indicates that defluidized zones were present.

Keywords: Solids mixing, fluidization, fluidized bed, bubbling bed, lateral dispersion, magnetic particle tracking

Nomenclature

D	Diameter of the bed particles, $[m]$
D_l	Lateral dispersion coefficient, $[\frac{m^2}{s}]$
D_{cell}	Depth of a mixing cell, $[m]$
G_s	Massflux of circulated solids, $[\frac{kg}{sm^2}]$
L	Characteristic length of the geometry, $[m]$
L_{cell}	Average length on a mixing cell, $[m]$
W_{cell}	Width of a mixing cell, $[m]$
μ_p	Viscosity of the fluidizing medium, $[Pa\ s]$
ρ_b	Density of the bed material, $[\frac{kg}{m^3}]$
ρ_f	Density of the fluidizing medium, $[\frac{kg}{m^3}]$
ρ_p	Density of the bed particles, $[\frac{kg}{m^3}]$
ρ_{fp}	Density of a fuel particle, $[\frac{kg}{m^3}]$
τ	Residence time in a mixing cell, $[s$
g	Gravitational constant, $[\frac{m}{s^2}]$
u_0	Superficial velocity, the air velocity on top of the riser, $[\frac{m}{s}]$
u_{mf}	Minimum fluidization velocity, i.e. the velocity at which minimum fluidization of a bed is achieved, $[\frac{m}{s}]$
MPT	Magnetic Particle Tracking

Acknowledgements

We would like to say a big thank you to our supervisor Carolina, who have helped and supported us a lot through the entire work. We appreciate you willingness to always discuss and bring new insights to the results. Also to our examiner David for insightful discussions and guidance during the work.

A big thanks to Fredrik and Jakob at RISE who have made this work possible by designing the MPT-equipment and helping us with the 3D-printing.

We would also like to thank Rustan for installing the new bottom section in S13 and helping us with our problems in the lab.

Finally a big thank you to the entire fluidization group for all your previous and ongoing work which has been of big help during our own work and for the warm welcome you have given us.

Jon Ahlgren and Pontus Wageborn, Gothenburg, June 2021

"I don't like sand. It's coarse
and rough and irritating
and it gets everywhere."
- Anakin Skywalker

Contents

List of figures **xiii**

List of tables **xxi**

1 Introduction **1**

2 Theory **3**
2.1 Fluidization 3
2.2 Solids mixing 4
2.3 Fluid-dynamical scaling 6

3 Methods **9**
3.1 Experimental setup 9
3.1.1 Downscaling in the S13 unit 9
3.1.2 The cold model fluidized bed - S13 11
3.1.3 MPT-sensors 13
3.1.4 Tracer particles 14
3.2 Measurement procedures 16
3.2.1 Standard measurement procedure 16
3.2.2 Evaluation of tracer bed coverage and location of mixing cells 17
3.3 Data analysis 20
3.3.1 Procedure for data collection 20
3.3.2 Final experimental design 20
3.3.3 Calculation methods 21
3.3.3.1 Brownian motion 21
3.3.3.2 Mixing cells 23

4 Results **25**
4.1 High bed height 25
4.1.1 Tracer bed coverage 25
4.1.2 Measurements with the GVC tracer 28
4.1.3 Mixing cell residence time 29
4.1.4 Dispersion calculations for the high bed 31
4.2 Medium bed height 40
4.3 Low bed height 52

5 Conclusions and further remarks **65**

Bibliography **67**

A Scaling calculations **I**

B Calculations for evaluation of simplified scaling laws **III**

B.1 Comparison Between the Cold Model Glass Bead Bed and the Superficial Hot Boiler . . . III

B.1.1 Froude number . . . III

B.1.2 Density ratio between bed material and fluidizing medium . . III

B.1.3 Ratio between minimum and maximum fluidization velocity . III

B.2 Comparison between the copper powder bed and the hot boiler IV

B.2.1 Froude number . . . IV

B.2.2 Density ratio between bed material and fluidizing medium . . IV

B.2.3 Ratio between minimum and maximum fluidization velocity . IV

C Plastic shield calculations **V**

D Pressure graphs from S13 **VII**

E Confidence intervals for Brownian motion calculations for the high bed **IX**

F Confidence intervals for mixing cell calculations for the high bed **XV**

G Confidence intervals for Brownian motion calculations at medium bed height **XXI**

H Confidence intervals for mixing cell calculations for at medium bed height **XXVII**

I Confidence intervals for Brownian motion calculations for the low bed **XXXVII**

J Confidence intervals for mixing cell calculations for the low bed **XLV**

List of figures

2.1 Diagram of the different sections of. The rising gas bubbles are illustrated as white circles and the bed material is colored orange. 4
2.2 Diagram of a mixing cell. The rising gas bubbles are illustrated as white circles, the solids movement (bulk solids and fuel particles) as black arrows and the mixing cell edges as dotted lines. The bed zones are also indicated. 5

3.1 Schematic picture of the S13 unit and its control system created by Djerf [24]. 12
3.2 Schematic of the bottom section of the S13 unit. 12
3.3 The sensor setup and placement around S13. 13
3.4 The placement of the MPT sensors and the approximate position of the distributor plate relative to the sensors in S13. 14
3.5 Two examples of tracers particles. The left one is the GVC tracer and the right one is the CLC tracer with a cylindrical magnet in one of the halves. 15
3.6 Two measurements comparing a case with good coverage and a case with bad coverage. 18
3.7 Example of the positional data and a corresponding velocity field plot for a 10 minute measurement at 0.43 $\frac{m}{s}$. 19
3.8 Demonstrates how the Matlab script calculates the dispersion using Einstein's equation of Brownian motion for a simple movement. . . . 22
3.9 Demonstrates how the Matlab script calculates the dispersion using Einstein's equation of Brownian motion for general tracer movement. 22

4.1 The velocity field for a measurement using the GMC tracer for 10 minutes at a superficial velocity of 0.43 $\frac{m}{s}$. Most of the bed has not been covered by the tracer. 25
4.2 The combined velocity field of 50 minutes of measurements using the GMC tracer for the glass beads at a superficial velocity of 0.43 $\frac{m}{s}$. A significant portion of the bed has not been covered by the tracer. . . . 26
4.3 The velocity field observed for a measurement using the GVC tracer particle for the glass beads for 10 minutes at a superficial velocity of 0.43 $\frac{m}{s}$. This resulted in almost full coverage of the bed. 27
4.4 The velocity field using the GVC tracer particle for the glass beads for a combined 30 minutes at a superficial velocity of 0.43 $\frac{m}{s}$. 27

4.5 Velocity field plot using 2 hours collected for the GVC tracer at high bed height and a superficial velocity of 0.43 $\frac{m}{s}$. The mixing cells are marked in black. . . . 28
4.6 Histogram showing the number of samples measured in each mixing cell identified in the bed for the high bed and a superficial velocity of 0.43 $\frac{m}{s}$. . . . 29
4.7 Normalized residence time for each mixing cell for the high bed and a superficial velocity of 0.43 $\frac{m}{s}$. . . . 30
4.8 Dispersion coefficient values from the measurements for the high bed calculated with Einstein's equation for Brownian motion. Every individual measurement is 15 minutes long. . . . 31
4.9 Mean values of the dispersion coefficient for the high bed calculated with Einstein's equation for Brownian motion. A total amount of 1 hour and 45 minutes of data was used. . . . 32
4.10 Values of the dispersion coefficient for the high bed and shorter individual measurement times calculated using mixing cells. The total measurement time is 80 minutes for (a) and 40 minutes for (b). . . . 33
4.11 Values of the dispersion coefficient for the high bed and shorter individual measurement times calculated with Einstein's equation for Brownian motion. The total measurement time is 70 minutes for (a) and 35 minutes for (b). . . . 35
4.12 Dispersion coefficient values from the measurements for the high bed calculated using mixing cells. Every individual measurement is 15 minutes long. . . . 36
4.13 Mean values of the dispersion coefficient for the high bed calculated using mixing cells. A total amount of 2 hours of data was used. . . . 37
4.14 Values of the dispersion coefficient for the high bed and shorter individual measurement times calculated using mixing cells. The total measurement time is 80 minutes for (a) and 40 minutes for (b). . . . 39
4.15 Positional data for one 20 minute measurement at medium bed height and a superficial velocity of 0.44 $\frac{m}{s}$. . . . 40
4.16 Velocity field for 2 hours and 40 minutes of measurements at medium bed height and a superficial velocity of 0.44 $\frac{m}{s}$. Mixing cells are present, but the structure is complex. The assigned mixing cells are marked in black. . . . 41
4.17 Histogram showing the number of point measured for each section of the bed at medium bed height and a superficial velocity of 0.44 $\frac{m}{s}$. . . 41
4.18 Dimensionless residence time for each mixing cell at medium bed height and a superficial velocity of 0.44 $\frac{m}{s}$. . . . 42
4.19 Dispersion coefficient values from the measurements for the medium height bed calculated with Einstein's equation for Brownian motion. Every individual measurement is 20 minutes long. . . . 43
4.20 Mean values of the dispersion coefficient for the medium height bed calculated with Einstein's equation for Brownian motion. A total amount of 2 hours and 20 minutes of data was used. . . . 44

4.21 Values of the dispersion coefficient for the medium high bed and shorter individual measurement times calculated with Einstein's equation for Brownian motion. The total measurement time is 105 minutes for (a), 70 minutes for (b) and 35 minutes for (c). 46
4.22 Dispersion coefficient values from the measurements for the medium bed height calculated using mixing cells. Every individual measurement is 20 minutes long. 48
4.23 Mean values of the dispersion coefficient for the medium bed height calculated using mixing cells. A total amount of 2 hours and 40 minutes of data was used. 49
4.24 Values of the dispersion coefficient for the medium high bed and shorter individual measurement times calculated using mixing cells. The total measurement time is 120 minutes for (a), 80 minutes for (b) and 40 minutes for (c). 51
4.25 The positional data for two measurements at the low height bed and a superficial velocity of 0.433. $\frac{m}{s}$. 52
4.26 Velocity field for 4 hours of measurements at low bed height with a superficial velocity of 0.433 $\frac{m}{s}$. Mixing cells are marked with black crosses. 53
4.27 Histogram showing the number of samples measured in each area of the bed at low bed height with a superficial velocity of 0.433 $\frac{m}{s}$. . . . 53
4.28 Velocity field for 1 hour of combined measurements for a low bed height and superficial velocity of 0.548 $\frac{m}{s}$. 54
4.29 Dimensionless residence time for each mixing cell at low bed height at low bed height with a superficial velocity of 0.433 $\frac{m}{s}$. 55
4.30 Dispersion coefficient values from the measurements for the low bed height calculated with Einstein's equation for Brownian motion. Every individual measurement is 20 minutes long. 56
4.31 Mean values of the dispersion coefficient for the low bed calculated with Einstein's equation for Brownian motion. A total amount of 3 hours and 40 minutes of data was used. 57
4.32 Values of the dispersion coefficient for the low bed and shorter measurements calculated with Einstein's equation for Brownian motion at low bed height. The total measurement time is 165 minutes for (a), 110 minutes for (b) and 55 minutes for (c). 59
4.33 Dispersion coefficient values from the measurements for the low bed height calculated with the mixing cell equation. Every individual measurement is 20 minutes long. 61
4.34 Mean values of the dispersion coefficient for the low bed calculated using mixing cells. A total amount of 4 hours of data was used. . . . 62
4.35 Values of the dispersion coefficient for the low bed and shorter individual measurements calculated using mixing cells equation at low bed height. The total measurement time is 180 minutes for (a), 120 minutes for (b) and 60 minutes for (c). 63

D.1 Pressure graph for the high bed. VII

D.2 Pressure graph for the medium bed. VIII
D.3 Pressure graph for the low bed. VIII

E.1 Brownian motion dispersion values with 95% confidence intervals for A1 for the high bed. IX
E.2 Brownian motion dispersion values with 95% confidence intervals for A2 for the high bed. X
E.3 Brownian motion dispersion values with 95% confidence intervals for A3 for the high bed. X
E.4 Brownian motion dispersion values with 95% confidence intervals for A4 for the high bed. XI
E.5 Brownian motion dispersion values with 95% confidence intervals for all data on side A for the high bed. XI
E.6 Brownian motion dispersion values with 95% confidence intervals for B1 for the high bed. XII
E.7 Brownian motion dispersion values with 95% confidence intervals for B2 for the high bed. XII
E.8 Brownian motion dispersion values with 95% confidence intervals for B3 for the high bed. XIII
E.9 Brownian motion dispersion values with 95% confidence intervals for B4 for the high bed. XIII
E.10 Brownian motion dispersion values with 95% confidence intervals for all data on side B for the high bed. XIV

F.1 Mixing cell dispersion values with 95% confidence intervals for A1 for the high bed. XV
F.2 Mixing cell dispersion values with 95% confidence intervals for A2 for the high bed. XVI
F.3 Mixing cell dispersion values with 95% confidence intervals for A3 for the high bed. XVI
F.4 Mixing cell dispersion values with 95% confidence intervals for A4 for the high bed. XVII
F.5 Mixing cell dispersion values with 95% confidence intervals for all data on side A for the high bed. XVII
F.6 Mixing cell dispersion values with 95% confidence intervals for B1 for the high bed. XVIII
F.7 Mixing cell dispersion values with 95% confidence intervals for B2 for the high bed. XVIII
F.8 Mixing cell dispersion values with 95% confidence intervals for B3 for the high bed. XIX
F.9 Mixing cell dispersion values with 95% confidence intervals for B4 for the high bed. XIX
F.10 Mixing cell dispersion values with 95% confidence intervals for all data on side B for the high bed. XX

G.1 Brownian motion dispersion values with 95% confidence intervals for A1 at medium bed height. XXI

G.2 Brownian motion dispersion values with 95% confidence intervals for A2 at medium bed height. XXII
G.3 Brownian motion dispersion values with 95% confidence intervals for A3 at medium bed height. XXII
G.4 Brownian motion dispersion values with 95% confidence intervals for A4 at medium bed height. XXIII
G.5 Brownian motion dispersion values with 95% confidence intervals for all data on side A at medium bed height. XXIII
G.6 Brownian motion dispersion values with 95% confidence intervals for B1 at medium bed height. XXIV
G.7 Brownian motion dispersion values with 95% confidence intervals for B2 at medium bed height. XXIV
G.8 Brownian motion dispersion values with 95% confidence intervals for B3 at medium bed height. XXV
G.9 Brownian motion dispersion values with 95% confidence intervals for B4 at medium bed height. XXV
G.10 Brownian motion dispersion values with 95% confidence intervals for all data on side B at medium bed height. XXVI

H.1 Mixing cell dispersion values with 95% confidence intervals for A1 at medium bed height. XXVII
H.2 Mixing cell dispersion values with 95% confidence intervals for A2 at medium bed height. XXVIII
H.3 Mixing cell dispersion values with 95% confidence intervals for A3 at medium bed height. XXIX
H.4 Mixing cell dispersion values with 95% confidence intervals for A4 at medium bed height. XXX
H.5 Mixing cell dispersion values with 95% confidence intervals for all data on side A at medium bed high. XXXI
H.6 Mixing cell dispersion values with 95% confidence intervals for B1 at medium bed height. XXXII
H.7 Mixing cell dispersion values with 95% confidence intervals for B2 at medium bed height. XXXIII
H.8 Mixing cell dispersion values with 95% confidence intervals for B3 at medium bed height. XXXIV
H.9 Mixing cell dispersion values with 95% confidence intervals for B4 at medium bed height. XXXV
H.10 Mixing cell dispersion values with 95% confidence intervals for all data on side B at medium bed height. XXXVI

I.1 Brownian motion dispersion values with 95% confidence intervals for A1 at low bed height. XXXVII
I.2 Brownian motion dispersion values with 95% confidence intervals for A2 at low bed height. XXXVIII
I.3 Brownian motion dispersion values with 95% confidence intervals for A3 at low bed height. XXXVIII

I.4 Brownian motion dispersion values with 95% confidence intervals for A4 at low bed height. XXXIX
I.5 Brownian motion dispersion values with 95% confidence intervals for A4 at low bed height. XXXIX
I.6 Brownian motion dispersion values with 95% confidence intervals for A4 at low bed height. XL
I.7 Brownian motion dispersion values with 95% confidence intervals for all data on side A at low bed height. XL
I.8 Brownian motion dispersion values with 95% confidence intervals for B1 at low bed height. XLI
I.9 Brownian motion dispersion values with 95% confidence intervals for B2 at low bed height. XLI
I.10 Brownian motion dispersion values with 95% confidence intervals for B3 at low bed height. XLII
I.11 Brownian motion dispersion values with 95% confidence intervals for B4 at low bed height. XLII
I.12 Brownian motion dispersion values with 95% confidence intervals for B5 at low bed height. XLIII
I.13 Brownian motion dispersion values with 95% confidence intervals for B6 at low bed height. XLIII
I.14 Brownian motion dispersion values with 95% confidence intervals for all data on side B at low bed height. XLIV

J.1 Mixing cell dispersion values with 95% confidence intervals for A1 at low bed height. XLV
J.2 Mixing cell dispersion values with 95% confidence intervals for A2 at low bed height. XLVI
J.3 Mixing cell dispersion values with 95% confidence intervals for A3 at low bed height. XLVII
J.4 Mixing cell dispersion values with 95% confidence intervals for A4 at low bed height. XLVIII
J.5 Mixing cell dispersion values with 95% confidence intervals for A5 at low bed height. XLIX
J.6 Mixing cell dispersion values with 95% confidence intervals for A6 at low bed height. L
J.7 Mixing cell dispersion values with 95% confidence intervals for all data on side A at low bed high. LI
J.8 Mixing cell dispersion values with 95% confidence intervals for B1 at low bed height. LII
J.9 Mixing cell dispersion values with 95% confidence intervals for B2 at low bed height. LIII
J.10 Mixing cell dispersion values with 95% confidence intervals for B3 at low bed height. LIV
J.11 Mixing cell dispersion values with 95% confidence intervals for B4 at low bed height. LV

J.12 Mixing cell dispersion values with 95% confidence intervals for B5 at low bed height. LVI
J.13 Mixing cell dispersion values with 95% confidence intervals for B5 at low bed height. LVII
J.14 Mixing cell dispersion values with 95% confidence intervals for all data on side B at low bed height. LVIII

List of tables

2.1 Presentation and description of the parameters used in Glicksman's full set scaling laws. 7
2.2 Presentation and description of the parameters used in Glicksman's simplified scaling laws. 7

3.1 Scaling parameters used for the downscaling of the bed with glass beads. 9
3.2 Scaling parameters used for the downscaling of the bed with copper powder. 10
3.3 Comparison of the parameters included in Glicksman's simplified scaling laws between the cold glass bead bed and the superficial hot boiler. 10
3.4 Comparison of the parameters included in Glicksman's simplified scaling laws between the cold copper powder bed and the hot boiler. . . . 11
3.5 The properties of the different tracer particles used in the glass bead bed. 16
3.6 The properties of the different tracer particles used in the copper powder bed. 16
3.7 Overview of the data from the final sets of measurements with the GVC tracer. 21

1
Introduction

In order to combat climate change, the dependency and usage of fossil feedstocks must be decreased and alternative fuels need to be used instead. Biomass is an abundant renewable energy resource and a higher and more efficient utilization of it can decrease the rate of green house gas emissions. Even if combusted, biomass is often considered a CO_2 neutral fuel since the carbon cycle is short enough for biomass to be continuously available [1].

Biomass often has heterogeneous physical and chemical characteristics and is therefore difficult to convert into thermal energy in conventional boilers in a way that is efficient and economical. It is therefore beneficial to use fluidized beds for its conversion [2]. Some advantages of using fluidized beds are the improved mixing of the fuel particles, the elimination of temperature gradients inside the furnace and the reduction of excess air needed for combustion, which increases the efficiency of the process [3, 4]. Given the complexity of the chemical and physical processes that take place in this type of unit, further knowledge of the actual bed behaviour of the solids is needed in order to develop mathematical models that can predict its performance [5].

During combustion insufficient lateral mixing leads to an uneven distribution of fuel particles across the bed. This requires an increased excess air ratio to combust the fuel particles in the zones of high concentration and thus a less efficient operation and high costs [6]. During indirect gasification too much lateral mixing leads to a decreased residence time due to increased fuel entrainment in the gas since the lateral mixing is proportional to the gas flow. Since the gasification process is slow this can result in incomplete gasification of the lighter fuel particles. Counteracting these effects requires further understanding of the mixing [6, 7] and studying in detail the parameters that govern the particles dynamics of fluidized beds can help dealing with these problems.

Small-scale experiments have been performed in the past [6, 8–11] to determine the lateral dispersion coefficient of fuel particles in fluidized beds, but the resulting values are different between different studies, ranging from magnitudes of 10^{-4} $\frac{m^2}{s}$ to 10^{-1} $\frac{m^2}{s}$ [9, 11, 12]. In some previous studies [8, 9] 2D bed models have been used to study the mixing visually, and therefore some relevant phenomena have not been captured. Thus, there is a need for further experiments for the characterization of the mixing in industrial fluidized beds.

An innovative technology has recently started to be used in the study of fluidized beds, this is magnetic particle tracking, which consists of multiple anisotropic magnetic resonance sensors [13] that can determine the position of a magnetic particle by sensing the strength and angle of the magnetic field. An magnetic particle tracking system allows for highly resolved 3D tracking of single particles, from which the velocity and acceleration can be calculated. In contrast to radioactive tracking of particles, it also allows for the use of metallic particles as bed material as long as they are non-magnetic. This is beneficial since metallic particles typically are of high density which is a requirement when applying dynamic scaling to industrial scale. Experiments have already been performed in a small scale unit and shown that a magnetic tracer particle can successfully be tracked in a small scale bed of bronze powder with a spacial resolution in the magnitude of 1 mm and a temporal resolution in the magnitude of milliseconds [5]. Experiments in larger scale are still required to uncover more details [6]. For this purpose, a new magnetic particle tracking system has been developed by RISE and Chalmers to allow for experiments in a 0.5×0.89 m^2 scale model of a >200 MW 13 times larger industrial boiler.

2
Theory

This chapter covers a general framework regarding fluidization, mixing of fuels in fluidized beds, the strategy for mixing calculations, scaling of the hot model to the cold model and a brief explanation of the principles which the magnetic particle tracking system is based on.

2.1 Fluidization

Fluidization occurs when a fluid is passed upward through a bed of solids at a velocity at or above minimum fluidization velocity. The minimum fluidization velocity is the fluid velocity at which the frictional forces between the particles are in equilibrium with the compressing forces on the particles caused by gravity. This velocity is specific to the bed material and fluid used. At minimum fluidization velocity the bed obtains properties similar to liquid and the volume of the bed increases, leading to a higher bed of lower density. These properties include flotsam behaviour of objects of lower density than the bed, jetsam behaviour of objects of higher density than the bed and evening of the bed surface. For solids typically used in boilers and at gas flow rates above the minimal fluidization gas bubbles form at the bottom and emerge at the surface of the bed. This is referred to as a bubbling fluidized bed [14]. Fluidization generally results in good mixing of solids and gases as well as high mass and heat transfer [15]. The uniform temperature profile in a bubbling fluidized bed allows for good control of large scale processes [14]. A bubbling bed can be divided into two fluid-dynamical regions, specifically the dense bottom bed, and the freeboard. The dense bottom bed is where the gas bubbles develop and rise to the surface. The gas bubbles grow as they rise as a result of bubble coalescence. The freeboard is where particles are either splashed above the surface due to bubbles bursting or are entrained in the gas flow [16]. These zones are shown in Figure 2.1.

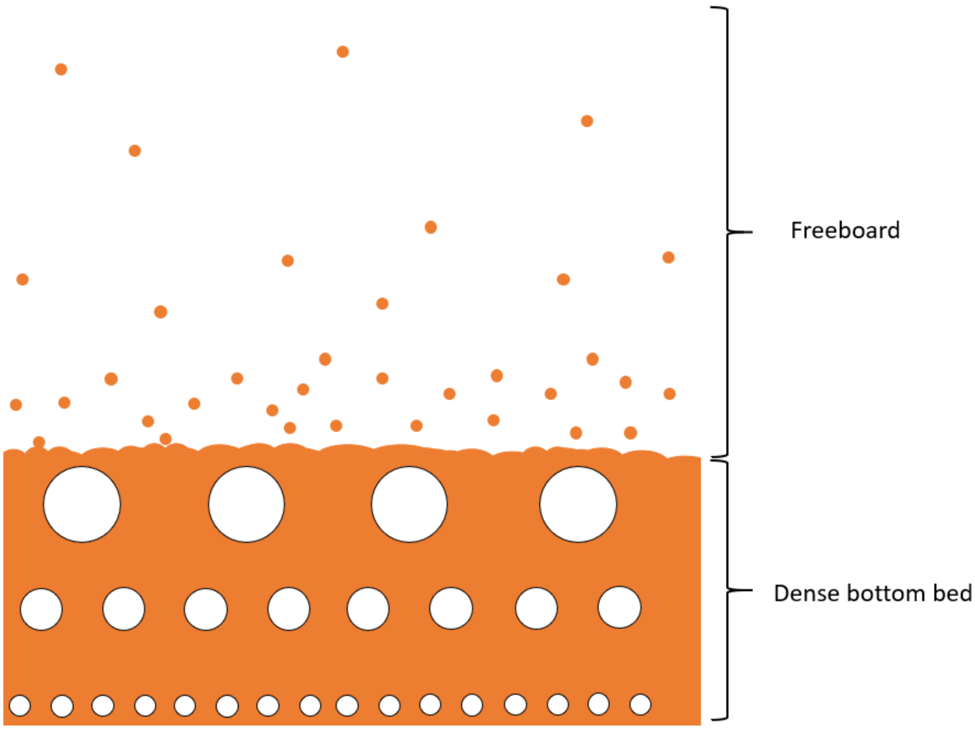

Figure 2.1: Diagram of the different sections of. The rising gas bubbles are illustrated as white circles and the bed material is colored orange.

2.2 Solids mixing

The mixing of solids in fluidized beds is a product of gas bubbles rising through the bed affecting the solids through three different mechanisms [17]. The first is the mixing caused by the lifting of solids in the wake of a rising gas bubble. The second is the sinking of solids in the emulsion around the gas bubble. The third mixing mechanism, which is the one with the largest contribution to the lateral dispersion, is the splashing of solids at the bed surface caused by the gas bubble erupting [7].

The gas bubbles have been observed to rise along preferential locations in the bed, referred to as bubble paths. A toroidal flow pattern of solids and fuel particles is formed surrounding this path [5]. The bubble path and the surrounding local flow pattern is referred to as a mixing cell and a visual representation of a mixing cell is presented in Figure 2.2. Fuel particles tend to be in low concentration in the bubble paths, they are instead found in higher concentration at the borders of the mixing cells in the sinking region around the bubbles and at the walls of the bed [10]. The bubbles develop and coalesce as they rise through the bed, meaning that the dense bottom bed height has a strong influence on the solids mixing. Specifically, a taller dense bottom bed has been observed to result in a higher horizontal dispersion coefficient for bulk solids, although this has not been observed for fuel particles suspended in the bed [5, 18]. The increased dispersion of bulk solids is the result of bubble paths coalescing leading to fewer but larger mixing cells. As they are transferred laterally between mixing cells, the mixing of fuel particles increases [2].

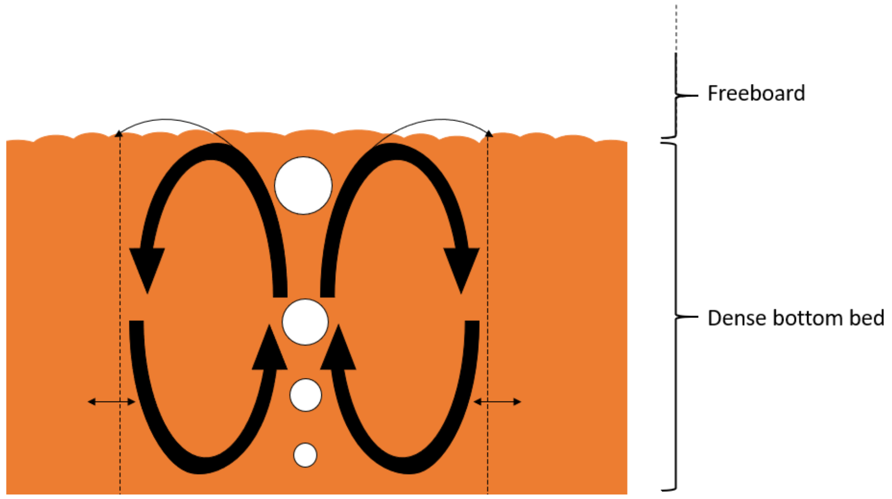

Figure 2.2: Diagram of a mixing cell. The rising gas bubbles are illustrated as white circles, the solids movement (bulk solids and fuel particles) as black arrows and the mixing cell edges as dotted lines. The bed zones are also indicated.

From the different methods that can be used for calculating the lateral dispersion coefficient two have been used in similar studies: the direct calculation based on Brownian motion and the one based on mixing cell theory [2, 9, 11]. To ensure that the calculated lateral dispersion coefficient is reasonable, it is suggested to calculate the mixing in different ways. Ideally, the resulting value should be independent of the method used.

A simple and direct way to calculate the lateral dispersion coefficient is using Einsteins equation for Brownian motion [19] presented in Equation (2.1)

$$D_l = \frac{\Delta x^2}{2\Delta t} \tag{2.1}$$

where D_l is the lateral dispersion coefficient in $\frac{m^2}{s}$, Δx the distance moved after a certain time in m, and Δt the time between two obervations. Since Equation (2.1) is defined for microscopic diffusional motion a method to filter out small motions that do not contribute to macroscopic dispersion needs to be applied. The most reliable method [8] to do this is to keep Δx constant, as varying the time might exclude the characteristic mixing time of the tracer. This set value of Δx is called the threshold length. A previous study [9] has shown that the results using this equation are time dependant.

The lateral dispersion can also be calculated using the concept of mixing cells by modifying Equation (2.1) into Equation (2.2) as follows:

$$D_l = \frac{L_{cell}^2}{2\tau} \tag{2.2}$$

where L_{cell} is the length of the mixing cell in m and τ the residence time in a mixing cell in s. This method requires that the mixing cells of the bed have been determined so that L_{cell} is known. This procedure is described in Section 3.3.3.2. With L_{cell}, the position of the mixing cells and the the tracer position it is possible calculate the average residence time of the tracer in the mixing cells and consequently the lateral dispersion coefficient can be calculated.

2.3 Fluid-dynamical scaling

Data collection from a hot industrial fluidized bed can be both difficult and unreliable [20]. A more convenient method is to use smaller cold models and scaling laws that preserve fluid-dynamic similarity with the hot bed while allowing for more convenient and robust data collection. Glicksman et al. has developed both a full set [21] and a set of simplified [22] scaling laws. The simplified set imposes less constraints on the geometry of the cold model while still correctly relating the fluidization conditions in the cold unit to the hot unit, and are applied in this project. The function of these laws is to preserve the dimensionless values presented in Tables 2.1 and 2.2 to achieve similar fluidization conditions between a hot and a cold unit.

Table 2.1: Presentation and description of the parameters used in Glicksman's full set scaling laws.

Dimensionless number	**Expression**	**Definition**
Froude number	$\frac{u_0^2}{gD}$	The ratio between the inertial and gravitational forces
-	$\frac{\rho_b}{\rho_f}$	The density ratio between the bed solids and the fluidizing medium
Particle Reynolds number	$\frac{\rho_p u_0 D}{\mu_f}$	Ratio between particle inertial forces and fluid viscous forces
Fluid Reynolds number	$\frac{\rho_f u_0 L}{\mu_f}$	Ratio between fluid inertial forces and fluid viscous forces
-	$\frac{G_s}{\rho_p u_0}$	External solids circulation

Table 2.2: Presentation and description of the parameters used in Glicksman's simplified scaling laws.

Dimensionless number	**Expression**	**Definition**
Froude number	$\frac{u_0^2}{gD}$	The ratio between the inertial and gravitational forces
-	$\frac{\rho_b}{\rho_f}$	The density ratio between the bed solids and the fluidizing medium
-	$\frac{u_0}{u_{mf}}$	Ratio between minimum and maximum fluidization velocity
-	$\frac{G_s}{\rho_p u_0}$	External solids circulation

The parameter $\frac{G_s}{\rho_p u_0}$ will not be used in the present work since there will not be any circulation of the bed material.

3
Methods

This chapter discusses the experimental setup, measurement procedures and data acquisition and processing.

3.1 Experimental setup

This section discusses how the gathered data can be related to larger beds operating at higher temperatures and presents the unit in which experiments were performed (hereafter called S13), the MPT-sensors and tracer particles.

3.1.1 Downscaling in the S13 unit

Two batches of experiments were to be performed in S13 with two different bed materials: glass beads and copper powder. Glass beads have a particle size distribution corresponding to d10-d50-d90 for 71-112-139μm, solids density of 2600 $\frac{kg}{m^3}$, a bed density at minimum fluidization of 1483 $\frac{kg}{m^3}$, minimum fluidization velocity of 0.012 $\frac{m}{s}$ and a terminal velocity of 0.64 $\frac{m}{s}$ [23]. Copper powder has a density of 8920 $\frac{kg}{m^3}$, a mean particle diameter of 35 μm and a minimum fluidization velocity of 0.0043 $\frac{m}{s}$ [16]. The characteristics for each material presented in Table 3.1 and 3.2.

Table 3.1: Scaling parameters used for the downscaling of the bed with glass beads.

Parameter	Unit	Superficial hot boiler	Cold model with glass beads
Length scale of the bed, L	m	L	$L/1.81$
Superficial velocity, u_0	$\frac{m}{s}$	u_0	$u_0/\sqrt{1.81}$
Temperature	$°C$	850	50
Bed material density, ρ_b	$\frac{kg}{m^3}$	2600	2600
Fuel particle density, ρ_{fp}	$\frac{kg}{m^3}$	571	See Table 3.5
Fluid density, ρ_f	$\frac{kg}{m^3}$	0.3143	1.204
Bed material particle size, D	μm	190	105

Table 3.2: Scaling parameters used for the downscaling of the bed with copper powder.

Parameter	Unit	Commercial boiler	Ideal cold model value	Cold model with copper powder
Length scale of the bed, L	m	L	$L/13$	$L/13$
Superficial velocity, u_0	$\frac{m}{s}$	u_0	$u_0/\sqrt{13}$	$u_0/\sqrt{13}$
Temperature	$°C$	850	50	50
Bed material density, ρ_b	$\frac{kg}{m^3}$	2600	10600	8920
Fuel particle density, ρ_{fp}	$\frac{kg}{m^3}$	571	2187	See Table 3.6
Fluid density, ρ_f	$\frac{kg}{m^3}$	0.3143	1.204	1.204
Bed material particle size, D	μm	190	14.6	35

The use of glass beads in the unit implies a different scaling ratio in relation to the original boiler [16] as can be seen from Table 3.1. For the purposes of the present work, the tracers were designed so that the density ratio between the bed material and fuel particle is kept constant compared to the hot unit. Using the properties of the glass beads, the up-scaling calculations were done and are available in Appendix A. They resulted in a boiler 7.18 times smaller than the commercial unit and 1.81 times larger than S13.

The scaling of the two beds were evaluated by comparing the parameters in Glicksman's simplified scaling laws for the two bed materials in S13 to their respective up-scaled alternative. This is presented in Table 3.3 for the glass bead bed and superficial hot boiler and in Table 3.4 for the copper powder bed and the boiler S13 is based on with calculations available in Appendix B.

Table 3.3: Comparison of the parameters included in Glicksman's simplified scaling laws between the cold glass bead bed and the superficial hot boiler.

Parameter	Value in cold model glass bead bed	Value in hot superficial boiler	Ratio between hot and cold value
$\frac{u_0^2}{gD}$	417.46-428.13	179.55-188.86	0.43-0.44
$\frac{\rho_b}{\rho_f}$	2159.45	8272.35	3.83
$\frac{u_0}{u_{mf}}$	35.83-36.75	50.21-51.50	1.40
$\frac{G_s}{\rho_p u_0}$	Not applicable	Not applicable	-

Table 3.4: Comparison of the parameters included in Glicksman's simplified scaling laws between the cold copper powder bed and the hot boiler.

Parameter	Value in cold model copper powder bed	Value in hot commercial boiler	Ratio between hot and cold value
$\frac{u_0^2}{gD}$	$970.83u_{0,C}^2$	$1934.41u_{0,C}^2$	1.99
$\frac{\rho_b}{\rho_f}$	7408.64	8272.35	1.12
$\frac{u_0}{u_{mf}}$	$232.56u_{0,C}^2$	$232.61u_{0,C}^2$	1.00
$\frac{G_s}{\rho_p u_0}$	Not applicable	Not applicable	-

From Table 3.3 and 3.4 it can be concluded that the scaling for the glass bead bed is alright except for quite poor density scaling while the copper powder bed has better scaling. Both experimental setups can still provide data about mixing phenomena in general and be used to evaluate the specific mixing conditions of S13.

3.1.2 The cold model fluidized bed - S13

The experiments were performed in the 0.89×0.5 m^2 S13 unit which is a 13 times smaller cold scale model of a commercial 200 MW$_{th}$ CFB boiler with an operating temperature of 850 ℃. A schematic picture of the entire S13 unit is shown in Figure 3.1 [24] and the bottom section of the unit is described more detailed in Figure 3.2. During operation, one fan was used to provide fluidization air to the system . The fan was controlled with a LabView interface that also provided information about the conditions in the bed, such as pressure at different heights, the net superficial velocity and the temperature of the air at the inlet. All data that the interface measured were recorded and collected in an Excel spreadsheet.

Adding and removing tracer particles to and from the bed was done through the first and third large lateral pipes seen in Figure 3.2. The left side of Figure 3.2 close to sensor 3 in Figure 3.4 is called A and the left side of Figure 3.2 close to sensor 1 in Figure 3.4 is called side B.

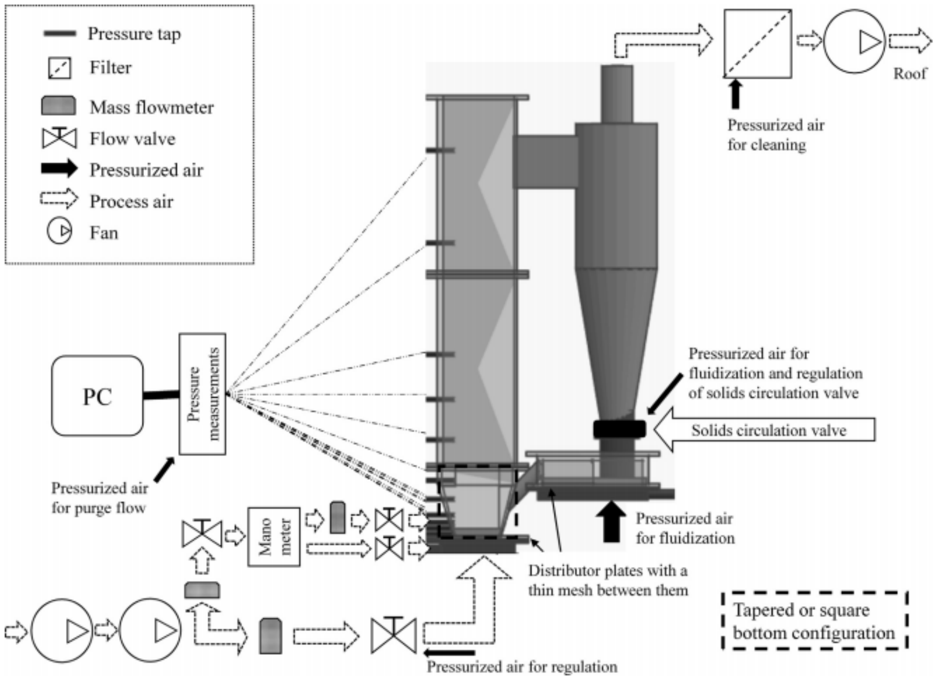

Figure 3.1: Schematic picture of the S13 unit and its control system created by Djerf [24].

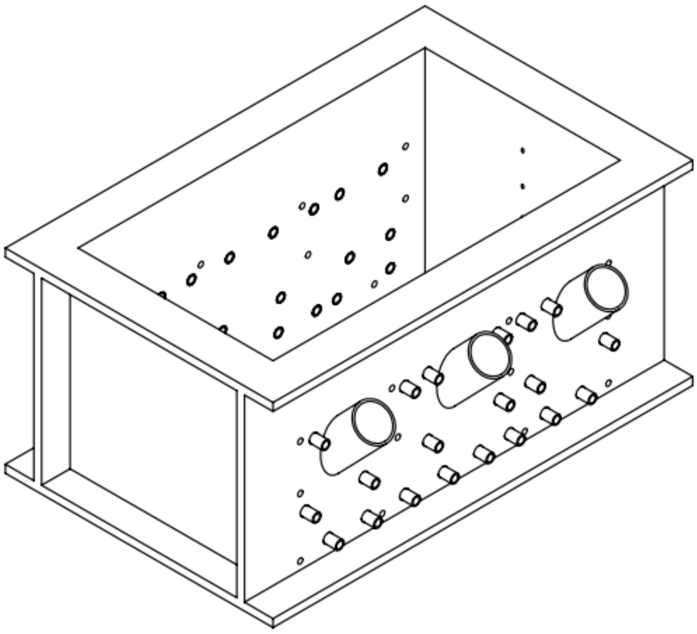

Figure 3.2: Schematic of the bottom section of the S13 unit.

3.1.3 MPT-sensors

The tracking system used in this work employs anisotropic magnetoresistive sensors which are based on the change in resistance of certain materials with a current running through them in the presence of a magnetic field [25]. They are henceforth referred to as magnetic particle tracking (MPT) sensors. The magnetic field is generated by the magnet placed in the center of the tracer particle and a current is run through each of the twelve sensors attached to the outside of S13. A background measurement is also performed to creates a baseline for ambient magnetic field in the geometry the tracer particle will be tracked in. These sensors can be used without involving harmful materials used in other tracking techniques such as radioactive tracking. It can also be used with metallic powders as bed material, which is necessary to scale the results to industrial conditions [5] as seen in Section 3.1.1. 10 MPT-sensors were mounted around the lateral walls of the bottom section of S13 and 2 more below the distributor plate of S13 as shown in Figure 3.3 and 3.4.

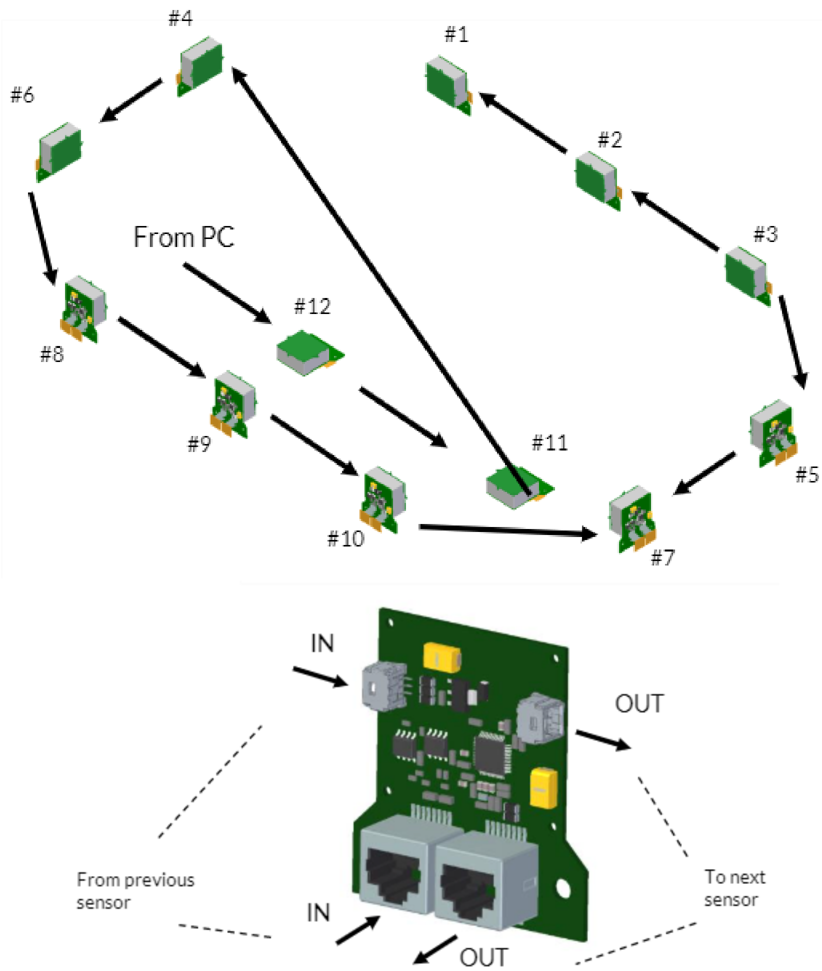

Figure 3.3: The sensor setup and placement around S13.

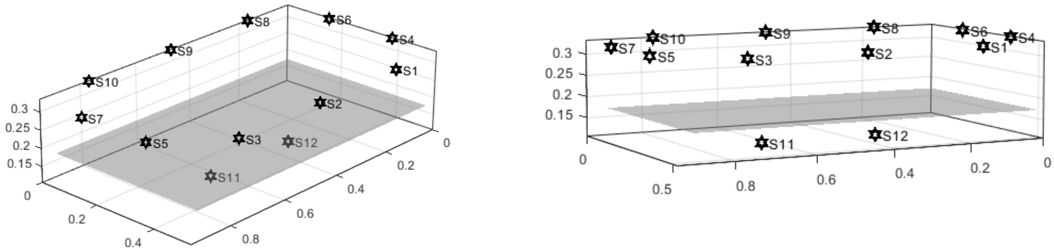

Figure 3.4: The placement of the MPT sensors and the approximate position of the distributor plate relative to the sensors in S13.

The MPT-sensors are connected in series with ethernet cables. A cable from sensor 12 connects them all to a laptop through a signal converter and to a power supply. A LabView program was used to operate the sensors. It allowed for monitoring of the signals in each individual sensor in real time and could record a static background measurement of the ambient magnetic field and a continuous measurement of a particle moving in the vicinity of the sensors. A recorded measurement with a corresponding background could be run in a Matlab program to obtain the xyz-coordinates and direction of the tracer particle at 20 Hz.

3.1.4 Tracer particles

The tracer particles resembling biomass were constructed by 3D-printing a spherical plastic shield made of ABS plastic around two types of magnets. They were designed to keep the density ratio between biomass and the bed particles in the commercial boiler. Three densities were chosen that resemble the density variations of wood chips [26], 370 $\frac{kg}{m^3}$, 470 $\frac{kg}{m^3}$ and 570 $\frac{kg}{m^3}$. In addition to this, two different sets of magnets were used, one 8 mm sphere with a weight of 2.03 g and one 5×5 mm cylinder with a weight of 0.763 g. In this way, 2 different tracer sizes were achieved for the densities mentioned above to study how the mixing is affected by particle size in addition to density. Examples of the shields are presented in Figure 3.5 and additional details about the calculations are available in Appendix C.

Figure 3.5: Two examples of tracers particles. The left one is the GVC tracer and the right one is the CLC tracer with a cylindrical magnet in one of the halves.

Since the glass beads have the same density as the material used in the hot unit, these tracer particles used with the glass bead bed should have a density similar to biomass. However, early measurements showed that using these tracers did not result in good mixing due to their large mass, so an additional smaller, lighter and denser tracer called GVC was used. the properties of all tracers intended to be used in the glass bead bed are presented in Table 3.5. The first letter in the acronym denotes which bed material the tracer is intended for (Glass beads or Copper powder), the second letter the relative density of the tracer (Low, Medium, High or Very high) and the third letter which magnet is in the tracer (Cylinder or Sphere).

Table 3.5: The properties of the different tracer particles used in the glass bead bed.

Tracer diameter [mm]	**Tracer weight [g]**	**Tracer density** $[\frac{kg}{m^3}]$	**Magnet shape**	**Magnet size [mm]**	**Magnet weight [g]**	**Tracer name**
51	26.7	370	Cylinder	5×5	0.763	GLC
37.6	13.1	470	Cylinder	5×5	0.763	GMC
30.2	8.2	570	Cylinder	5×5	0.763	GHC
17.2	2.7	1010	Cylinder	5×5	0.763	GVC
53.8	30.1	370	Sphere	8	2.03	GLS
41	17.9	470	Sphere	8	2.03	GMS
14	11.7	570	Sphere	8	2.03	GHS

Copper powder has a higher density than the glass beads which yields denser and smaller tracer particles, their properties are presented below in Table 3.6.

Table 3.6: The properties of the different tracer particles used in the copper powder bed.

Tracer diameter [mm]	**Tracer weight [g]**	**Tracer density** $[\frac{kg}{m^3}]$	**Magnet shape**	**Magnet size [mm]**	**Magnet weight [g]**	**Tracer name**
15.6	2.8	1417	Cylinder	5×5	0.763	CLC
13.4	2.3	1800	Cylinder	5×5	0.763	CMC
12.2	2.1	2183	Cylinder	5×5	0.763	CHC
19	5.1	1417	Sphere	8	2.03	CLS
16.8	4.5	1800	Sphere	8	2.03	CMS
15.2	4.0	2183	Sphere	8	2.03	CHS

3.2 Measurement procedures

This section describes how the measurements were carried out and how the data was acquired and preprocessed for further calculations.

3.2.1 Standard measurement procedure

To perform long measurements with the MPT-sensors the temperature of the sensors and ambient magnetic field needs to be kept as constant as possible. The procedure used to keep these conditions constant consisted of starting both the senors and the fans while having a constant airflow at the superficial velocity the measurement would be run at. When the temperature had reached a stationary value a background recording of the ambient magnetic field was performed. This was followed by cutting the air flow so that the seal to one of the large pipes on side A or B could be opened without any bed material leakage to place the magnet in the bed. After resealing the opening, the air flow was then increased again to the same value as before and when the current temperature was less than one degree away from the background temperature, the measurement was started. After the measurement the air flow was again turned off to extract the magnet through one of the pipes and then the process could be repeated for a new measurement. The procedure was run a number of times for the same fluidization conditions and alternating the opening used to introduce the tracer. In this way, statistically relevant data were intended.

3.2.2 Evaluation of tracer bed coverage and location of mixing cells

An initial assessment of the bed coverage is performed by evaluating a plot of the positions of all the sample points measured in one experiment. This is to ensure that the particle traveled across the bed in random movements. If any patterns are observed in a measurement, this can quickly be investigated to evaluate whether the the bed was fully fluidized and if the tracer interacted with the whole bed. Figure 3.6a shows a case where the tracer covered the whole bed and Figure 3.6b a case where the tracer has not been able to reach the region near the center of the bed in the right plot. The second case indicates that the conditions in the bed where not satisfactory during the measurement.

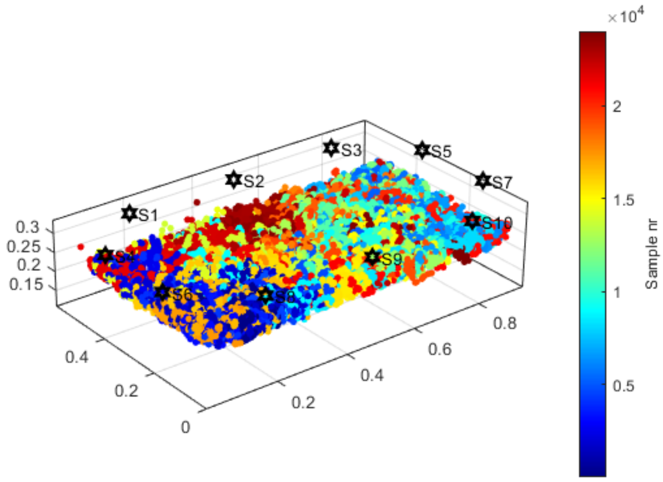

(a) Measurement for a medium bed height in which good bed coverage has been achieved at a fluidization velocity of 0.43 $\frac{m}{s}$.

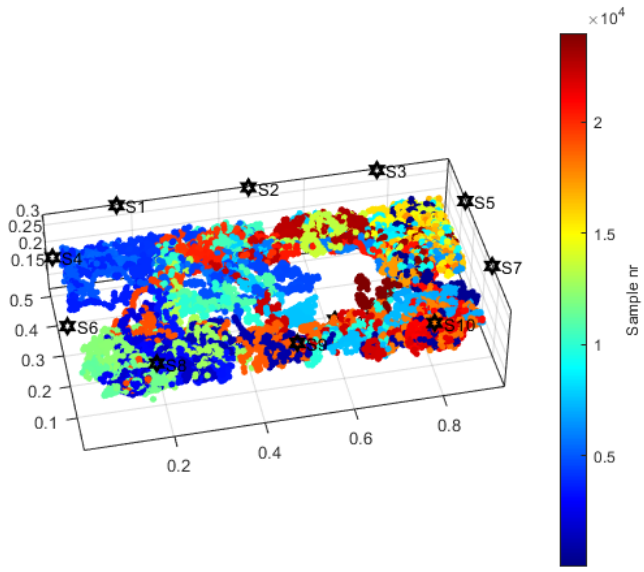

(b) Measurement for a low bed height in which good bed coverage has not been achieved at a fluidization velocity of 0.433 $\frac{m}{s}$.

Figure 3.6: Two measurements comparing a case with good coverage and a case with bad coverage.

To investigate if mixing cells can be identified, a plot referred to as a velocity field plot is used. The plot divides a horizontal slice of the bed located 90 percent of the way the bed surface counted from the bottom of the bed into a grid. All measured points below the horizontal slice are placed in a grid space matching their position. This grid space is then colored according to the average vertical velocity of the points measured in that grid space. Red indicates that the average velocity is positive, in other words that the particle is traveling upwards in that small region, and darker red means a higher vertical velocity. Negative velocities are assigned blue colors with darker tones indicating a higher downwards velocity. Colors where the tracer was not detected even once during the experiment are shown as white in the plot. In Figure 3.7a a 3D positional data plot is shown with a corresponding velocity field plot in 3.7b.

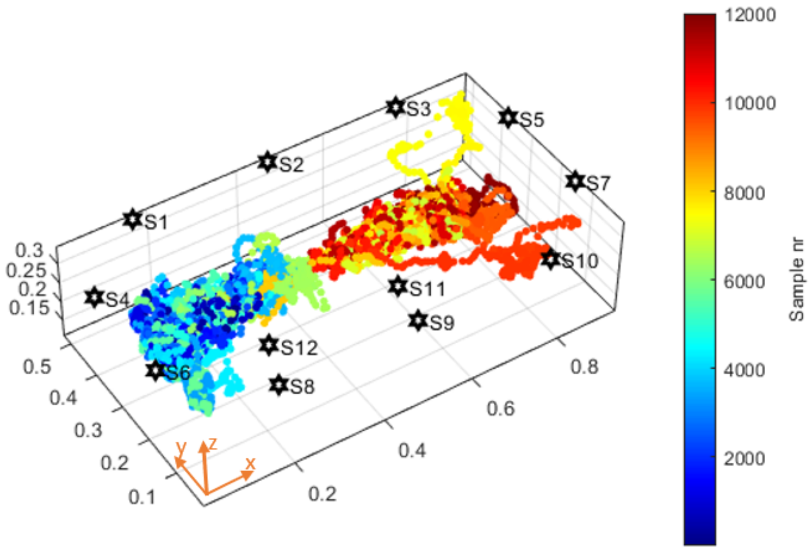

(a) Positional data of a measurement.

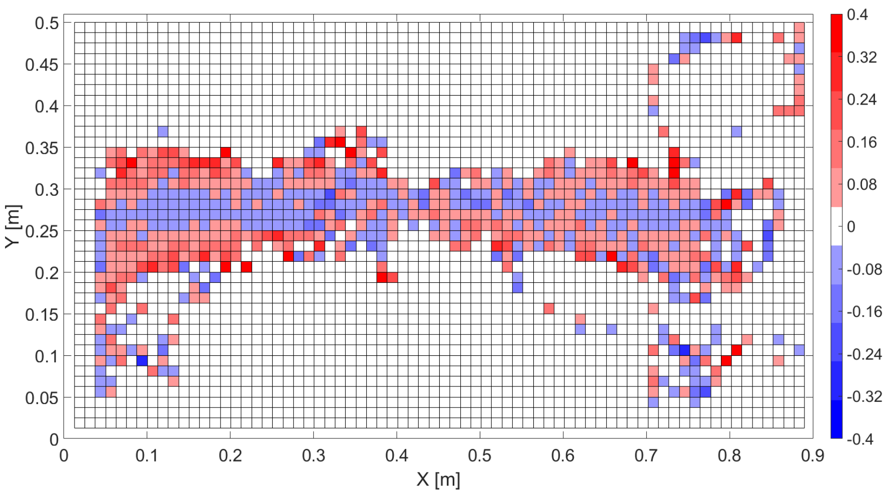

(b) Corresponding velocity field for an experiment. Red indicates areas in which the particle has traveled upwards with darker shades meaning higher velocities. Blue indicates downward velocity with darker shade meaning higher downwards velocities. No mixing cells are identified in this example.

Figure 3.7: Example of the positional data and a corresponding velocity field plot for a 10 minute measurement at 0.43 $\frac{m}{s}$.

Data from all successful experiments performed under similar conditions are then combined to form a single velocity field plot.

3.3 Data analysis

Describes the final experimental design and discusses the calculation strategy.

3.3.1 Procedure for data collection

The two sets of tracer shields for the two different magnets made it possible to study how both the density and size of the tracer influences the mixing, since the cylindrical magnet is lighter than the sphere. Even though the 12 different designed tracers were expected to be tested with each of the selected fluidization conditions, before all different tracers and velocities could be tested, data for a few cases was collected to improve the calculation methods and set a suitable duration for each measurement. These results are discussed further in Section 4.1.1 with the conclusion that the tracer particles designed for the glass beads bed were too large and heavy to interact properly with the bed, while the smaller cylinder tracer with very high density yielded better results. Due to time and safety considerations, associated with the loading and manipulation of the copper bed material, as well as the achievement of the successful experiments that allowed a complete development of the experimental and calculating methods, only the glass beads were used in this work. It should be pointed out that the findings of the present work are general to the use of MPT for precise determination of solids dispersion in fluidized beds. The final experimental design on which the results are based, is presented below.

3.3.2 Final experimental design

The GVC tracer was tested at three different bed heights at a fluidization velocity of 0.43 $\frac{m}{s}$ (with slight variations in velocity among experiments). This velocity had proven to give good mixing conditions from earlier measurements while avoiding too violent fluidization that could result in losing bed material to the cyclone or lifting the tracer too high above the sensed volume, both of which effects would result in bad tracking. The different bed heights were achieved by adding to or removing bed material from the bed, and assessed from the data from pressure sensors mounted at different heights in S13. The pressure profiles along the height of the model are available in Appendix D. Data for these different measurements is presented in Table 3.7. The measurements were initially 15 minutes long but were changed to 20 minutes to make the data collection more efficient. In total at least two hours of data was gathered for each bed height with half of the data from each side A and B.

Table 3.7: Overview of the data from the final sets of measurements with the GVC tracer.

Estimation of bed height [m]	Average superficial velocity [$\frac{m}{s}$]	Individual measurement length [min]	Total amount of measurement data collected [min]
0.163-0.25 (High)	0.430	15	120
0.076-0.113 (Medium)	0.441	20	160
0.076-0.113 (Low)	0.433	20	240

3.3.3 Calculation methods

The acquired data (from the 12 sensors) is processed by applying an optimization algorithm that determines the precise position and orientation of the tracer in every moment. The tracer trajectory is then processed in Matlab in order to determine the lateral dispersion coefficient. This was done using the two different methods discussed in the Theory chapter.

3.3.3.1 Brownian motion

Einsteins equation for Brownian motion is presented in Equation (2.1) and as mentioned in Section 2.2, the best results are obtained if the length Δx is kept constant [8]. Since diffusion is the result of random movement, the walls in the S13 model pose an obstacle that would prevent the particle from displaying truly random motion. To account for this, the dispersion is only calculated by tracer movement in a region away from the walls.

The created Matlab script takes both of the considerations mentioned above into account while calculating the lateral dispersion coefficient according to Equation (2.1). A border a certain distance from the walls in the xy-plane is defined Samples outside these borders are discarded to avoid the influence of wall effects. A threshold length is also defined to filter out small movements which do not contribute to the mixing. When the distance between the current location and the entry location is larger than the threshold length, that distance is saved and the time spent for performing that trajectory is calculated as the number of points between the two locations divided with the sample time of the magnets, 20 *Hz*. In this way only tracer movements larger than the selected threshold are accounted for. The consistency of the calculation can be tested by evaluating an experiment with different values for the threshold length, the dispersion coefficient should become independent of the length at threshold lengths larger than L_{cell} [11].

Two examples of the described procedure are shown in Figure 3.8 and 3.9. The red points are tracer locations outside the defined borders, green points inside the borders and blue points the location before the tracer enters the borders. The purple lines are the distances filtered with the threshold length criteria used to calculate the lateral dispersion coefficient.

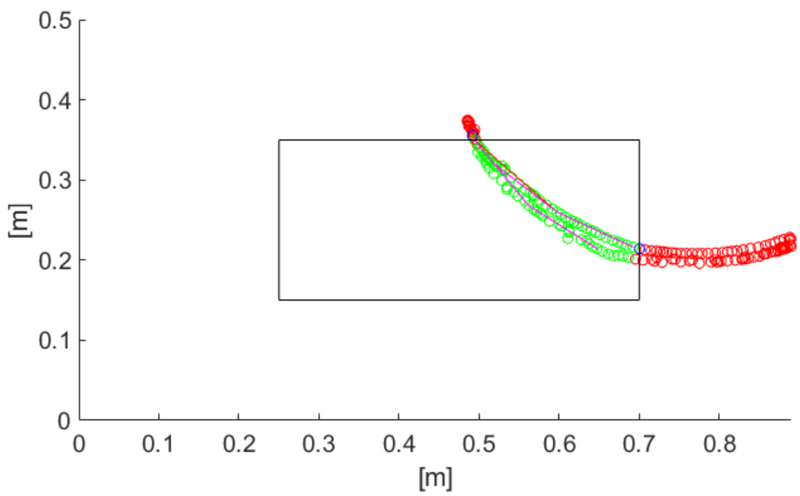

Figure 3.8: Demonstrates how the Matlab script calculates the dispersion using Einstein's equation of Brownian motion for a simple movement.

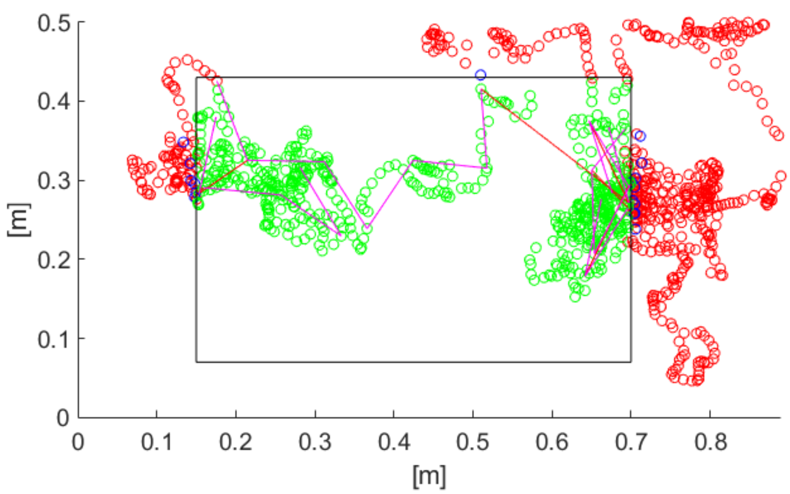

Figure 3.9: Demonstrates how the Matlab script calculates the dispersion using Einstein's equation of Brownian motion for general tracer movement.

3.3.3.2 Mixing cells

The size of the mixing cells can be determined by studying the velocity field of the tracer and identifying regions with dominant down- and upwards velocity. This is followed by dividing the bed with a grid with every square having the length L_{cell} ideally, or the depth D_{cell} and width W_{cell} with the characteristic length of the cell L_{cell} being the mean between them if the cells were not shaped as a square. A Matlab script was then run that checked how many of the grid point coordinates on the x- and y-axis the current tracer position was larger than which determined which mixing cell the tracer currently resided in. When this value changes, the tracer has switched cell and the residence time can be calculated by dividing the amount of sample points in the cell by the sample time 20 Hz. With the residence time acquired, the dispersion coefficient understood as the characteristic time for the particle to change from one mixing cell to an adjacent one is calculated. All dispersion coefficient values were saved and the mean value of the lateral dispersion coefficient was calculated when the entire measurement had been analysed. As previously stated, tracer positions near the wall should not be accounted for, since the wall prevents the random movement. Therefore only the central mixing cells that are not adjacent to the wall should be used for this calculation. It was not possible to assign the exact coordinates of the mixing cells, so to avoid inaccurate calculations, a filter was applied that required the particle to have minimum residence time in a mixing cell before it switched cell in order for the mixing to be accounted for.

4
Results

The initial results consists of some results from the experiments using the tracers designed for the glass beads bed, which were used to evaluate and improve the experimental procedures and calculations. This is followed by a deeper analysis at different bed heights with the GVC tracer that had better bed coverage than the other tracers designed to be used in the glass bead bed.

4.1 High bed height

This section covers the development of the experimental procedures by comparing the bed coverage obtained using the less dense GMC tracer and the denser GVC tracer. This is followed by a more detailed analysis using the GVC tracer.

4.1.1 Tracer bed coverage

A 10 minute measurement was run using the GMC tracer at a superficial velocity of 0.43 $\frac{m}{s}$. The velocity field for this measurement was then examined and is presented in Figure 4.1.

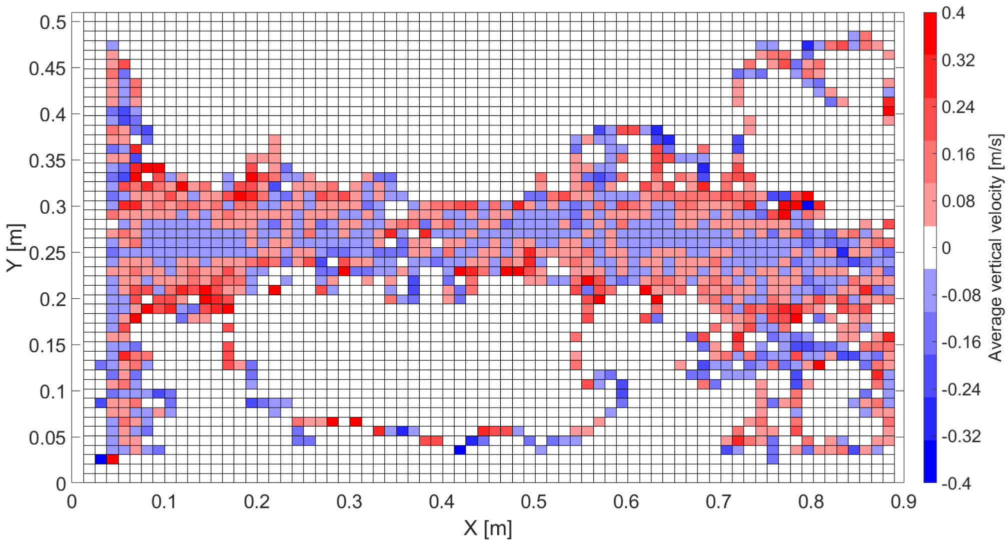

Figure 4.1: The velocity field for a measurement using the GMC tracer for 10 minutes at a superficial velocity of 0.43 $\frac{m}{s}$. Most of the bed has not been covered by the tracer.

Figure 4.1 shows that the tracer is not covering the whole bed. This could be the result of the experiment time being too short or the particle moving in a pattern which restricts it from full bed coverage. This could indicate that the movement is not Brownian, since random particle movements would not result in such uneven surface coverage. To examine if this is the result of insufficient time a combined velocity field plot for 50 minutes of measurements performed under similar conditions and is shown in Figure 4.2. The same behaviour persists. The tracer movement is therefore not characteristic of a particle in a fluidized bed. Mixing cells can not be identified in the velocity field plot and the only pattern that can be observed is a sinking zone extending along the entire x-axis between the values 0.25m and 0.3m om the y-axis.

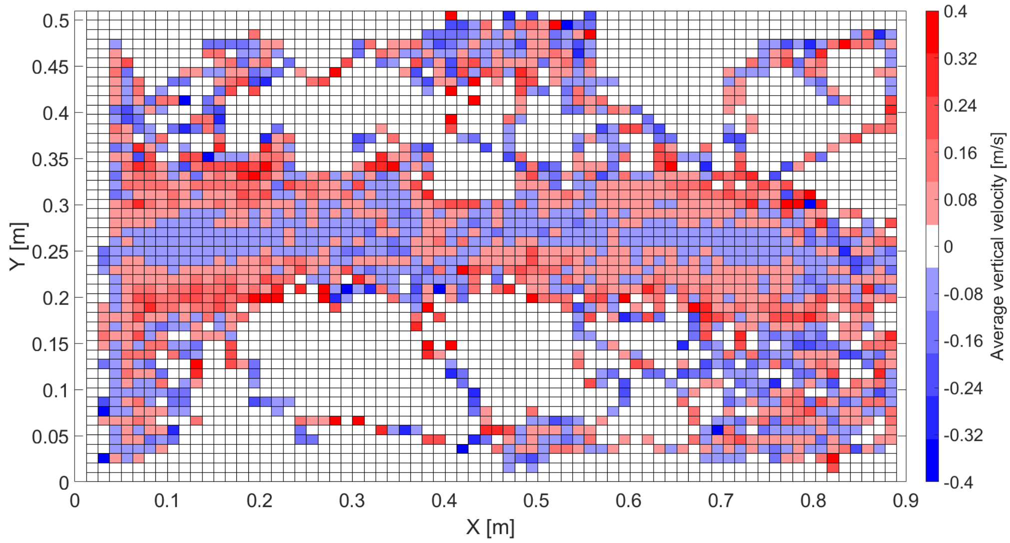

Figure 4.2: The combined velocity field of 50 minutes of measurements using the GMC tracer for the glass beads at a superficial velocity of 0.43 $\frac{m}{s}$. A significant portion of the bed has not been covered by the tracer.

This imperfect mixing of the GMC tracer particle in the bed was believed to be the result of the large size of the tracer (37.6 mm diameter, 470 $\frac{kg}{m^3}$), since spacial limitations could restrict the free movement of the particle. In order to further investigate this hypothesis, equivalent experiments were performed under similar fluidization conditions and using the GVC tracer, which is smaller and denser that the originally proposed GMC tracer. The velocity field and positional data was produced. This resulted in considerably larger coverage over the bed and more easily identifiable patterns in the velocity field plot, see Figure 4.3.

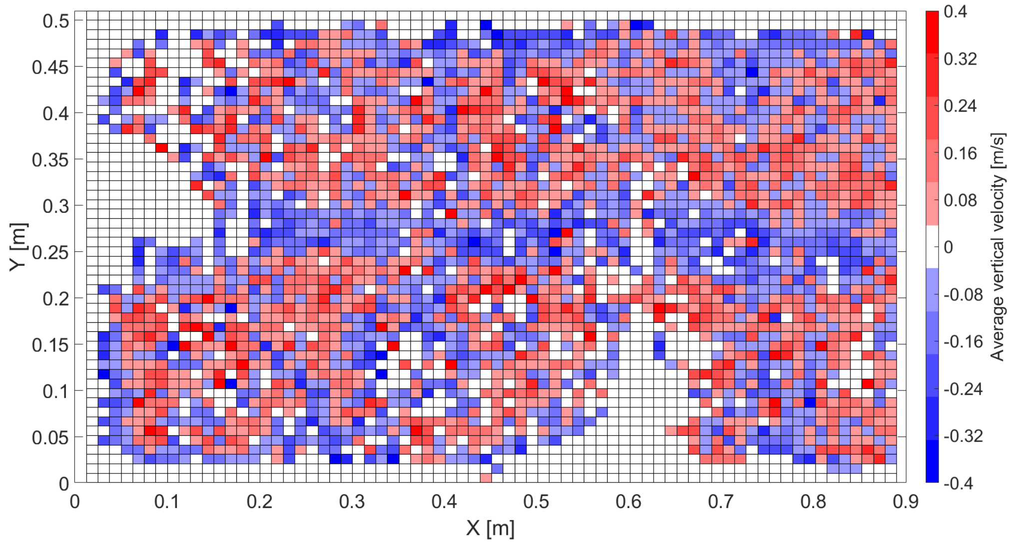

Figure 4.3: The velocity field observed for a measurement using the GVC tracer particle for the glass beads for 10 minutes at a superficial velocity of 0.43 $\frac{m}{s}$. This resulted in almost full coverage of the bed.

A plot using a combined 30 minutes of data from three different measurements under the same conditions was produced using the GVC tracer. All but a few points across the bed were covered, as presented in Figure 4.4. The data then showed a tendency for zones of upward velocity to appear in clusters above and below the sinking zone along the y-axis. This could be the result of the particle following preferential paths when going up the bed and would then be a sign of the presence of mixing cells.

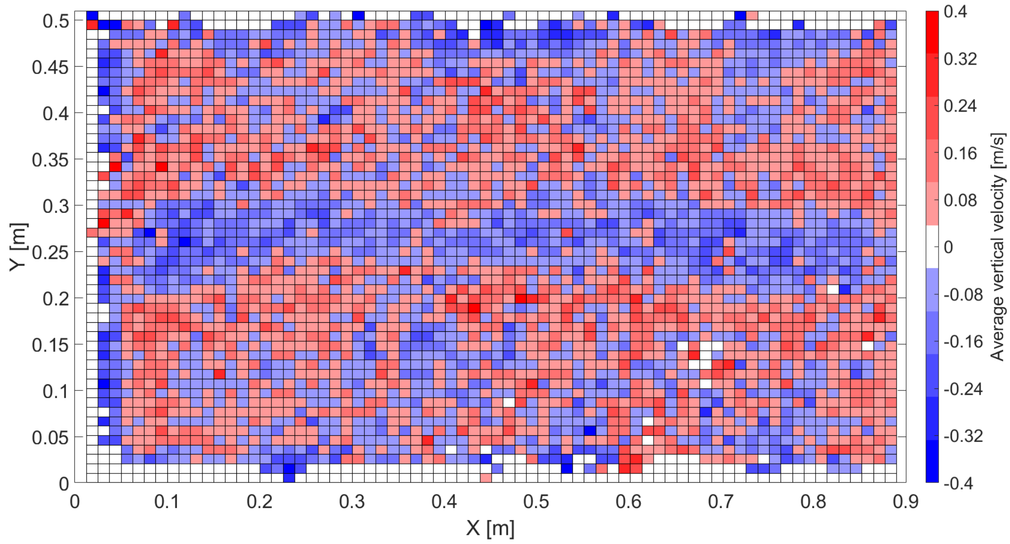

Figure 4.4: The velocity field using the GVC tracer particle for the glass beads for a combined 30 minutes at a superficial velocity of 0.43 $\frac{m}{s}$.

An almost full coverage of the bed is obtained. A clear pattern is visible with alternating areas of upwards and downwards velocities along the y-axis. The sinking zone along the x-axis between values 0.25m and 0.3m on the y-axis previously observed in Figure 4.2 is also observed here.

These results indicate that the tracer particles intended to be used with the glass beads are too large for a consistent interaction with the mixing cells of the bed. This issue does not persist for the smaller GVC tracer, which was therefore selected to be used for the rest of the measurements. The method for running experiments was now set and from here on the same structure will be used to present the results from all three bed heights.

4.1.2 Measurements with the GVC tracer

Continued measurements are run for the small GVC tracer. Individual measurements are run 15 minutes. For every set of conditions, eight repetitions are completed in order to sum a total time of 2 hours. For 4 of these repetitions, the tracer is inserted at position A and for the other 4, at position B. The resulting velocity field plot shows observable clusters of upward movement with alternating areas of downward movement, as can be seen in Figure 4.5.

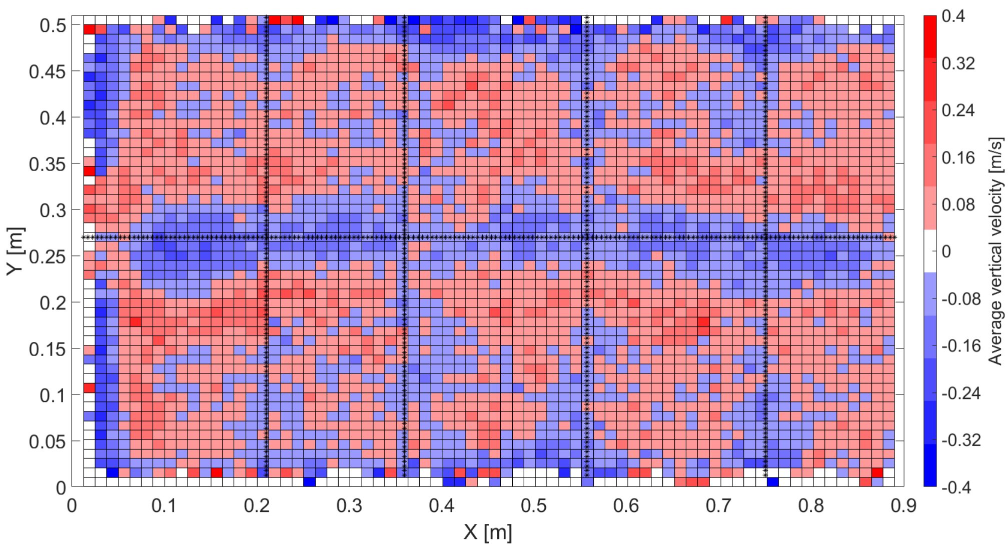

Figure 4.5: Velocity field plot using 2 hours collected for the GVC tracer at high bed height and a superficial velocity of 0.43 $\frac{m}{s}$. The mixing cells are marked in black.

The sinking zone along the x-axis can still be observed and can be concluded to be a feature of the S13 construction. For stability purposes, the distributor plate is attached to the structure underneath by means of screws located along that zone. This seems to cause some extent of defluidization and therefore, to create an additional hindrance to the free movement of the particles. As for these experiments, the bed appears to be divided into 10 identifiable mixing cells based on this picture with an L_{cell} of 0.214 m. This length is used for the calculation of dispersion coefficient. Since only two mixing cells are observed along the y-axis, no mixing cells free of influence of wall effects can be studied at this bed height.

To investigate whether the results are statistically significant across the whole bed, the number of sample points in each mixing cell is calculated. The resulting histogram plot for a high bed height is shown in Figure 4.6.

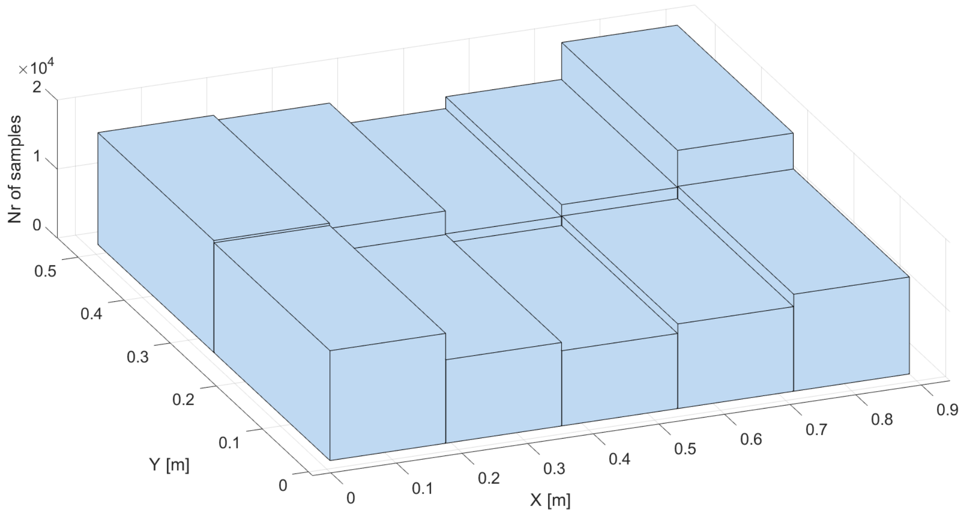

Figure 4.6: Histogram showing the number of samples measured in each mixing cell identified in the bed for the high bed and a superficial velocity of 0.43 $\frac{m}{s}$.

The histogram shows that the tracer traveled across the entire bed and did not show a strong preference for specific regions. The fact that every zone has a large number of samples measured is indication of the statistical validity of the analysis.

4.1.3 Mixing cell residence time

In order to to test a hypothesis that the residence time of a mixing cell depends on the length of perimeter open to transfer between mixing cells, the average residence times of each mixing cell were examined. If the hypothesis is correct, the residence time of a mixing cell should be inversely proportional to the total length of the cell perimeter which faces other mixing cells. This would result in higher residence times at the walls, particularly in the corners. The average residence time of the tracer in each cell was obtained by dividing the total time spent in each mixing cell by the number of times the particle left the mixing cell. Dimensionless mixing times were calculated by dividing the average residence time of each cell with the total average residence time calculated using all cells, meaning that a value above 1 is above average and below 1 is below average. The resulting dimensionless residence times are shown in Figure 4.7.

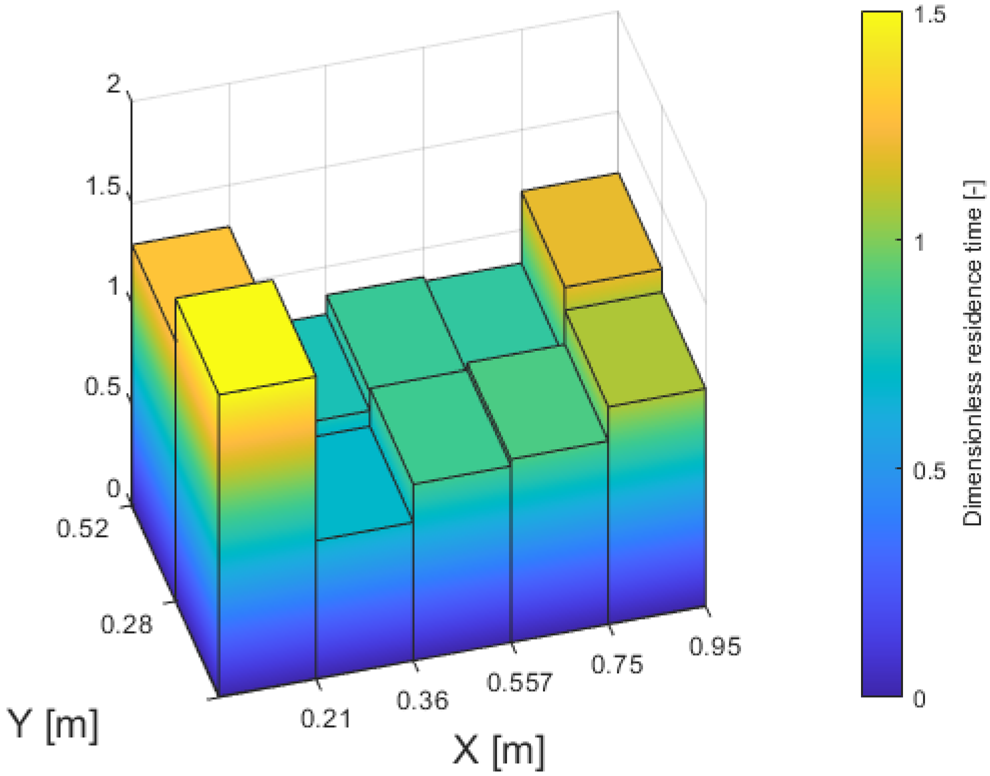

Figure 4.7: Normalized residence time for each mixing cell for the high bed and a superficial velocity of 0.43 $\frac{m}{s}$.

The results show that the mixing cells in the corners of the bed have the highest residence times. This is an expected result since out of the four sides of the mixing cell, two are facing the wall. This leads to fewer opportunities for the tracer to leave the mixing cell. This is a further indication that the bed height should be lower to allow the studying of mixing cells without wall contact, since a lower bed height is expected to result in smaller mixing cells present in larger numbers. One corner of the bed has a particularly high residence time. The reason for this is not clear, but uneven fluidization across the bed is a possible factor.

4.1.4 Dispersion calculations for the high bed

To avoid some wall effects for the calculations at this bed height the corner cells were excluded from the calculations. Dispersion values using Einstein's equation for Brownian Motion and varying the threshold length between 0.01 and 0.3 m for both sides of S13 with the mixing cells in the corners excluded are presented for each measurement in Figure 4.8. Graphs with confidence intervals for each separate measurement and mean values are available in Appendix E.

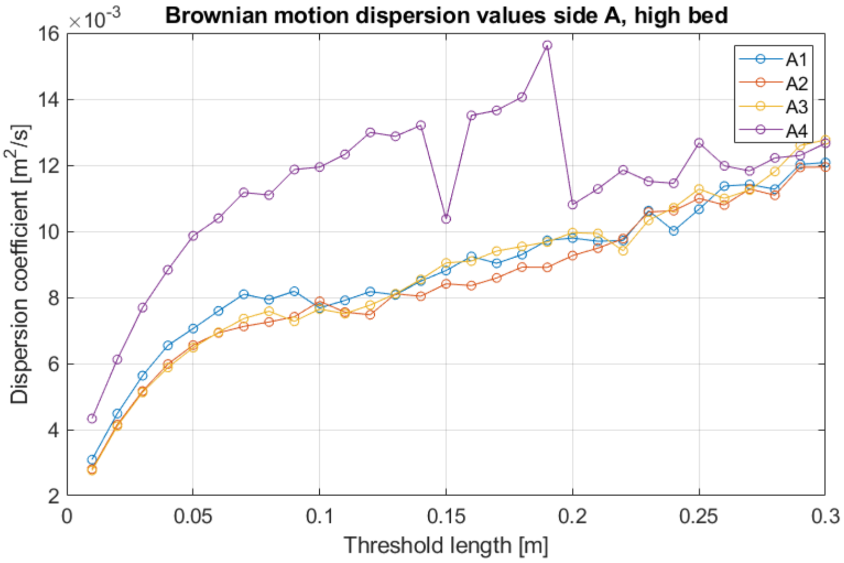

(a) Dispersion coefficient values from the measurements for the high bed with the tracer inserted at side A.

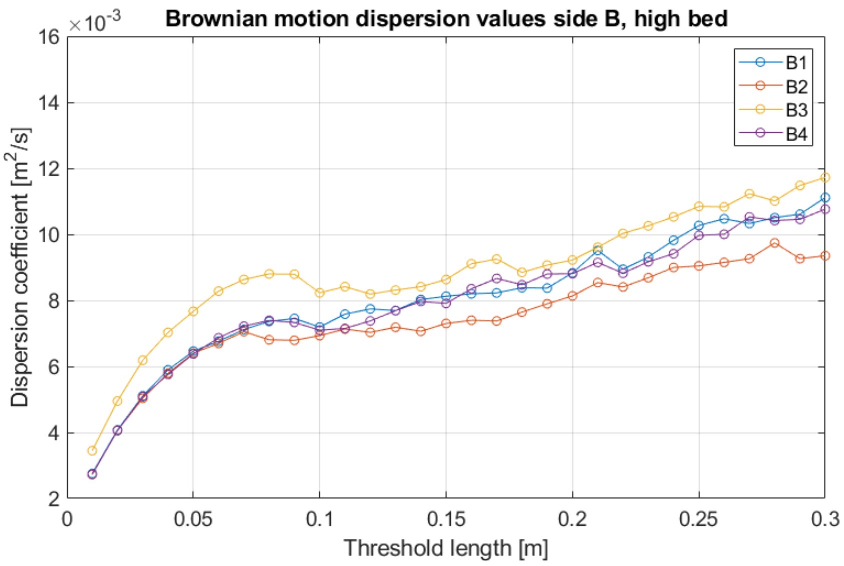

(b) Dispersion coefficient values from the measurements for the high bed with the tracer inserted at side B.

Figure 4.8: Dispersion coefficient values from the measurements for the high bed calculated with Einstein's equation for Brownian motion. Every individual measurement is 15 minutes long.

From Figure 4.8 it is clear that the calculated value of the dispersion coefficient is dependent on the threshold length but all values are in line with earlier research [11, 12]. The dispersion values and variance of A4 in Figure 4.8a are deviating from the rest of the measurements and therefore measurement A4 was not included in the graphs displaying mean values for all measurements in Figure 4.9.

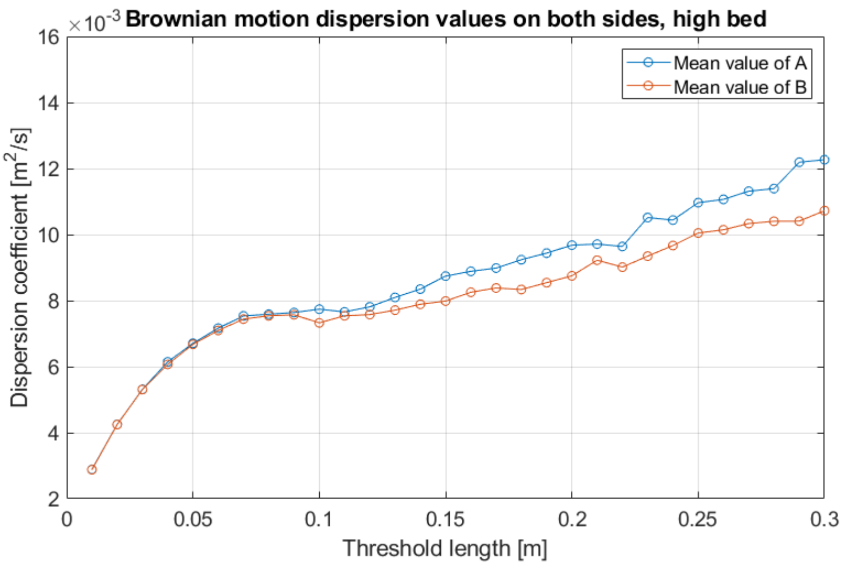

(a) Mean dispersion coefficient values from the measurements for the high bed and each side of tracer insertion.

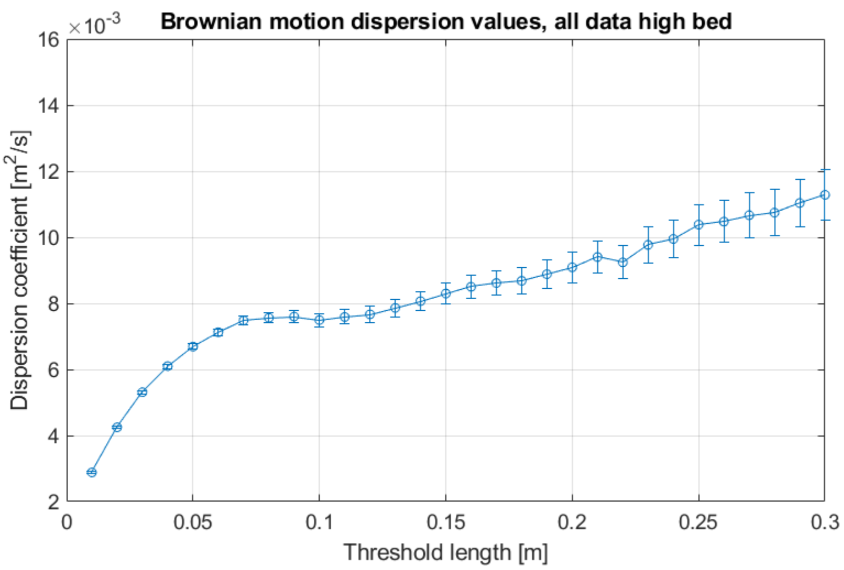

(b) Mean dispersion coefficient values for all measurements for the high bed.

Figure 4.9: Mean values of the dispersion coefficient for the high bed calculated with Einstein's equation for Brownian motion. A total amount of 1 hour and 45 minutes of data was used.

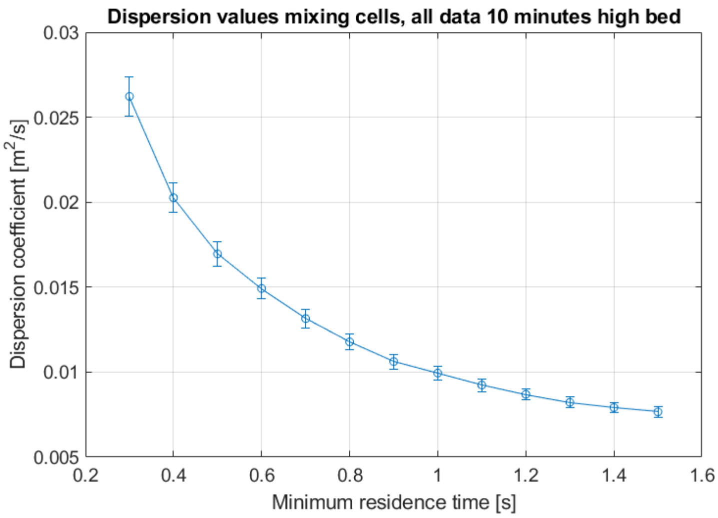

(a) 10 minute individual measurement length.

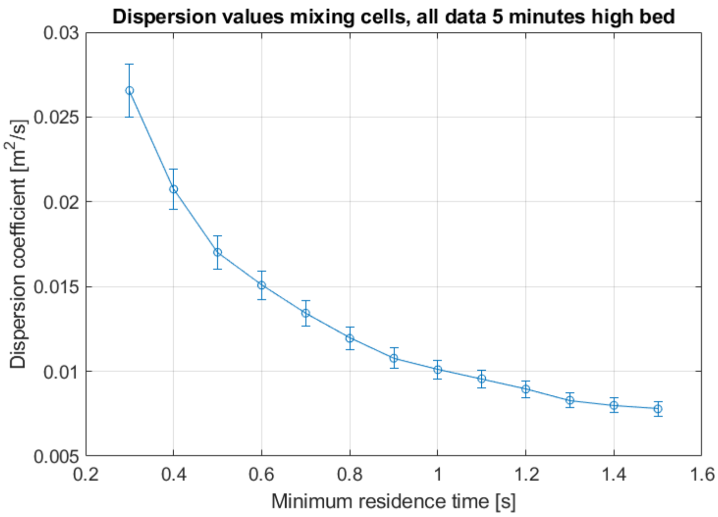

(b) 5 minute individual measurement length.

Figure 4.10: Values of the dispersion coefficient for the high bed and shorter individual measurement times calculated using mixing cells. The total measurement time is 80 minutes for (a) and 40 minutes for (b).

Theoretically [11] the value of the dispersion coefficient should increase until the threshold length reaches L_{cell} and then level out, which is observed around a threshold length of about 0.08 m in both Figure 4.8 and Figure 4.9. When the threshold length increases beyond 0.11 m the value of the dispersion coefficient starts to increase again. This is suspected to stem from the squared length step in Equation (2.1) which could increase faster than the time step when the threshold length gets large. Despite this increase, the leveling out indicates that Einstein's equation for Brownian movement is a suitable tool to evaluate the dispersion of the tracer. A mixing cell length between 0.08-0.11 m means that the estimation of L_{cell} at 0.214 m using the velocity field in Figure 4.5 is poor and that other tools are needed to properly size the mixing cells. Between threshold lengths 0.08 and 0.11 m the value of the dispersion coefficient is $7.6 \times 10^{-3} \pm 1.6 \times 10^{-4}$ $\frac{m^2}{s}$. It can also be noted that the mean value of the dispersion coefficient from measurements on the different sides is the same at low threshold lengths and higher on side A for larger threshold lengths.

The dispersion coefficient was also calculated with all measurements but with a lower individual measurement duration by cutting the data at 10 and 5 minutes from the original 15 minutes with the resulting graphs in Figure 4.11. This was done to study if the full measurement length is enough to capture all relevant mixing phenomena in the bed.

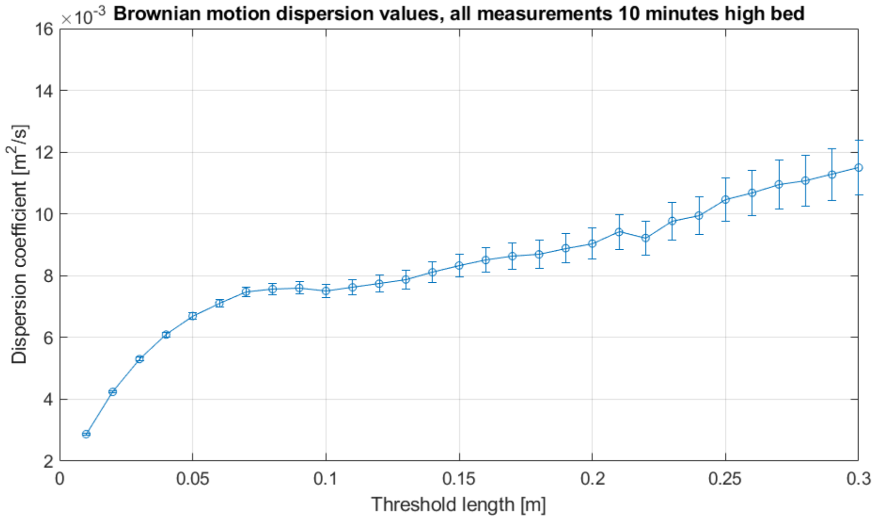

(a) 10 minute individual measurement length.

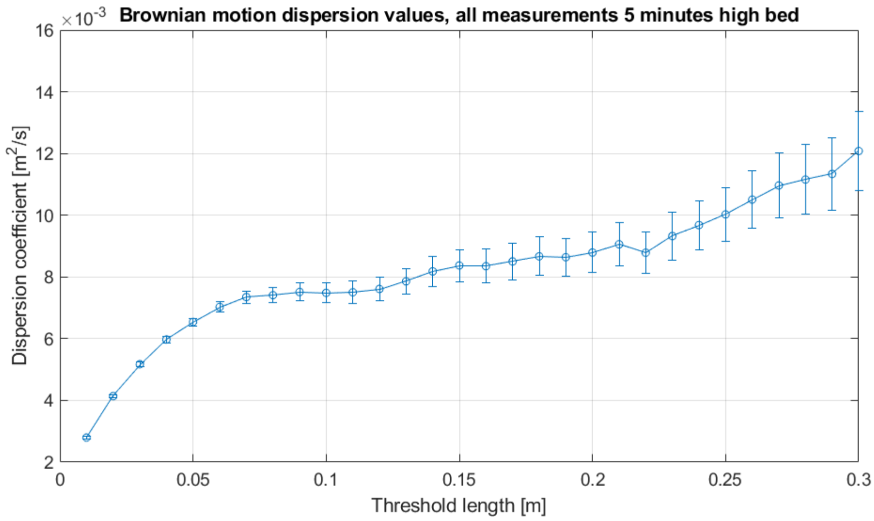

(b) 5 minute individual measurement length.

Figure 4.11: Values of the dispersion coefficient for the high bed and shorter individual measurement times calculated with Einstein's equation for Brownian motion. The total measurement time is 70 minutes for (a) and 35 minutes for (b).

The comparison Figure 4.9 and Figure 4.11 shows no clear differences except some higher variance due to lower amounts of data for the shorter measurement times and slightly lower values in Figure 4.11b compared to the full 15 minute measurements in Figure 4.9. This behavior was not observed in a previous study [9] were the dispersion coefficient value was higher at shorter measurement times, but it could also mean that the results have already stabilized at 5 minutes.

Calculating the dispersion coefficient with the mixing cells method and the mixing cells in the corners excluded resulted in the graphs presented in Figure 4.12 and Figure 4.13 for minimum residence times between 0.3 and 1.5 seconds with complementing graphs with confidence intervals available in Appendix F. These graphs are highly dependent on the amount of filtering applied, which sets a limit for the minimum residence time required for the tracer in order to account for the mixing. This filtering technique has no theoretical basis but is applied due to the difficulties of precisely defining the coordinates for the mixing cells.

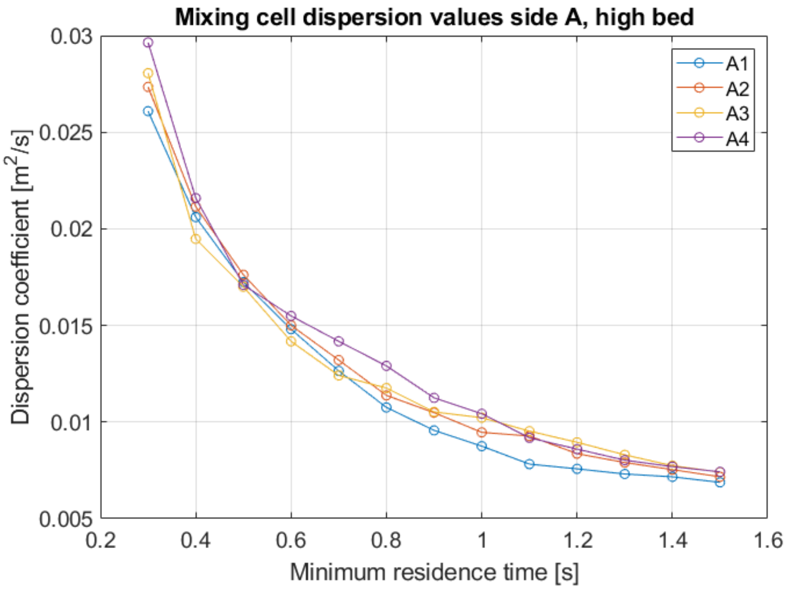

(a) Dispersion coefficient values from the measurements for the high bed with the tracer inserted at side A.

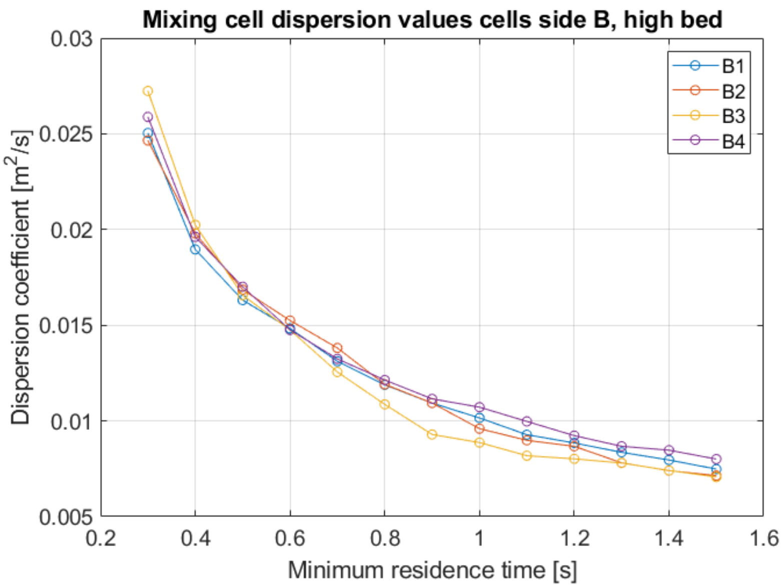

(b) Dispersion coefficient values from the measurements for with the tracer inserted at side B.

Figure 4.12: Dispersion coefficient values from the measurements for the high bed calculated using mixing cells. Every individual measurement is 15 minutes long.

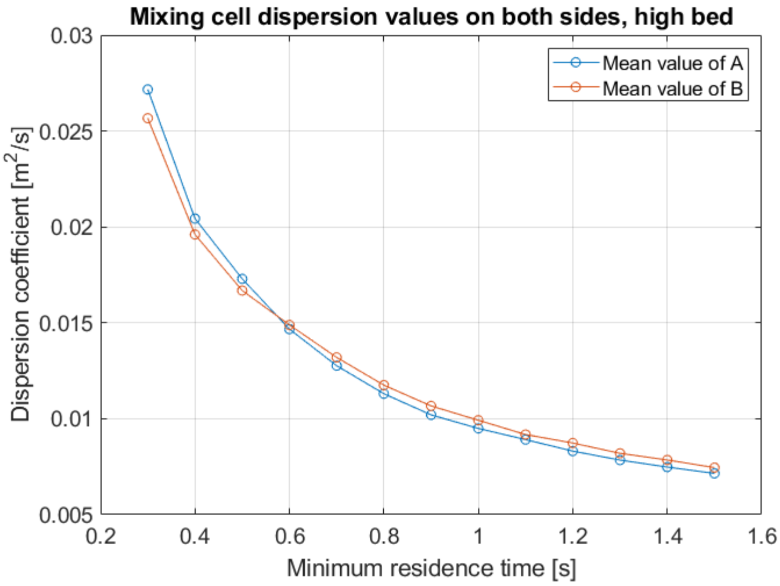

(a) Mean dispersion coefficient values from the measurements for the high bed and each side of tracer insertion.

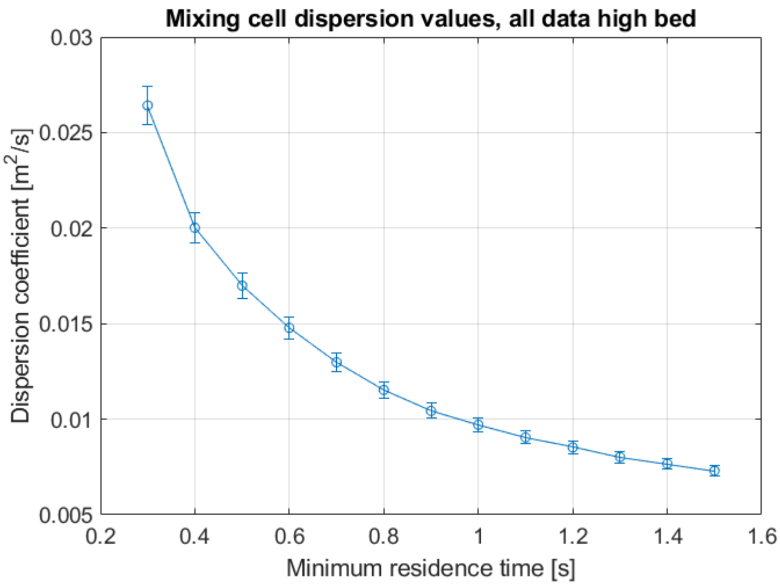

(b) Mean dispersion coefficient values for all measurements for the high bed.

Figure 4.13: Mean values of the dispersion coefficient for the high bed calculated using mixing cells. A total amount of 2 hours of data was used.

Since the filtering technique is not based on any theory it is not possible to say what values in Figure 4.12 and 4.13 are correct. These calculations also have a high degree of uncertainty since the exact mixing cell length could not be established, as the estimations from the velocity field and Figure 4.9 does not agree with each other. The variance in Figure 4.13b decreases as the minimum residence time increases which is expected as only longer residence times are a high level of filtering. At higher minimum residence times, the dispersion values from the mixing cell calculation converge towards the value at the plateau for the Brownian movement calculation. This would mean that incorrectly placed mixing cells mostly affects the dispersion coefficient value at low minimum residence times, in other words the small and rapid movements, while the slow and large movements are less affected by the uncertainties of the length and positions of the mixing cells. The dispersion coefficient value from the Brownian motion calculations, $7.6 \times 10^{-3}\ \frac{m^2}{s}$, is found at a minimum residence time of 1.5 seconds.

Comparing the data from the two different calculation methods shows that the dispersion values from measurement A4 are more similar to the values from other measurements when using the mixing cell method compared to the Brownian motion method. The Brownian motion calculations uses the tracer particles trajectory which requires that every recorded tracer position is correctly placed. A small magnetic disturbance could mean that a few points are recorded incorrectly which the Brownian motion algorithm would interpret as if the particle has moved a long distance in a short time step. This results in inaccurate dispersion coefficient values that could have a large influence on the overall result. The mixing cell method seems to be better at handling these disturbances, as no fluctuating values from an individual measurement or strange variance increases were observed. One possible cause for this is that inaccurate tracer particle positions will not affect the data if the recorded position still is in the same mixing cell, and that it is easy to filter out short disturbances where the tracer changes mixing cells, which was done in this case. However, even if the mixing cell method can handle small disturbances in the data better, it requires that the mixing cells are properly assigned before any calculations can be performed.

Calculations at shorter individual measurement times were performed for the mixing cell method and they are presented in Figure 4.14.

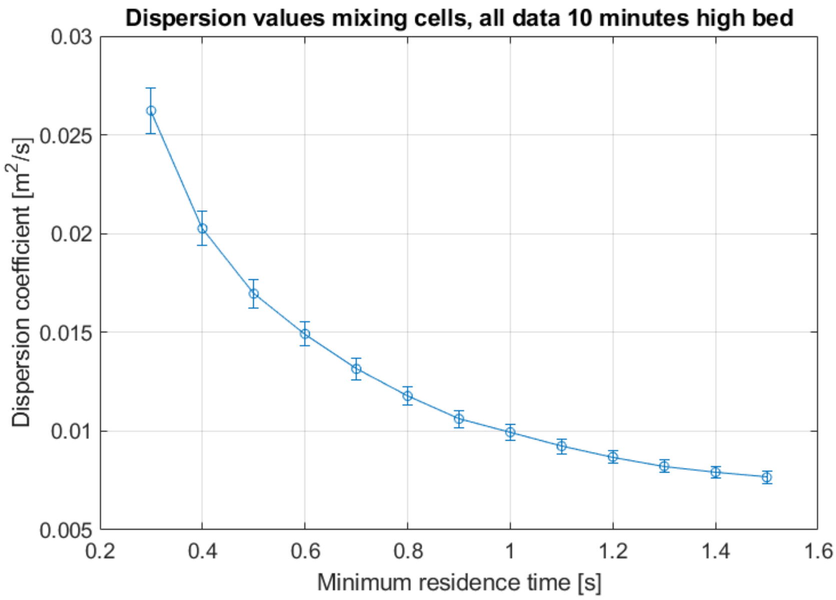

(a) 10 minute individual measurement length.

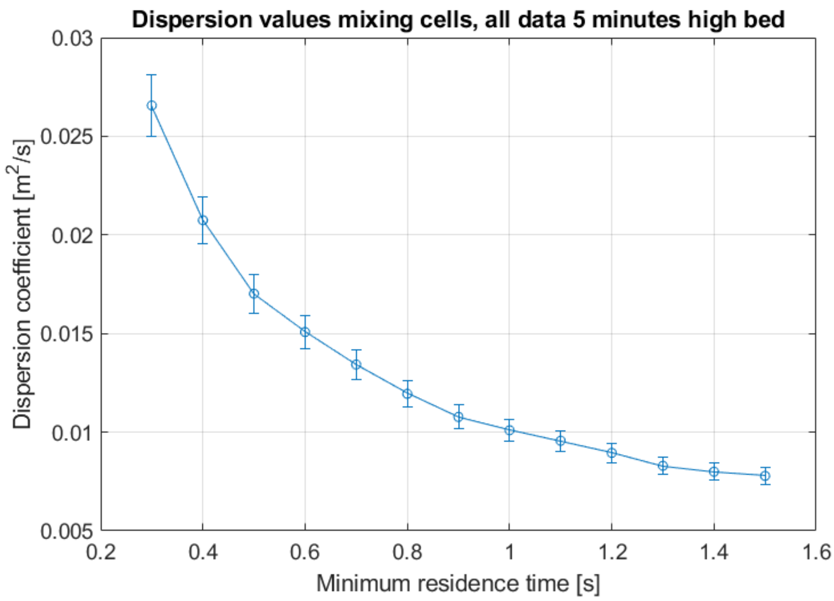

(b) 5 minute individual measurement length.

Figure 4.14: Values of the dispersion coefficient for the high bed and shorter individual measurement times calculated using mixing cells. The total measurement time is 80 minutes for (a) and 40 minutes for (b).

The graphs in Figure 4.14 and the bottom graph in Figure 4.13 are quite similar even in Figure 4.14b but with the values and variance increasing slightly as the individual measurement time decreases.

4.2 Medium bed height

Measurements at medium bed height were only performed using the GVC tracer. Individual measurements are 20 minutes long with 4 performed from each side A and B giving a total measurement time of 2 hours and 40 minutes. The analysis follows the same structure as the latter part of the previous section, with an initial evaluation of the bed coverage and partitioning of mixing cells before the residence time in different parts of the bed and dispersion coefficient values are calculated.

At a medium bed height the GVC tracer covered the entire bed in one 20 minute measurement which is demonstrated in Figure 4.15.

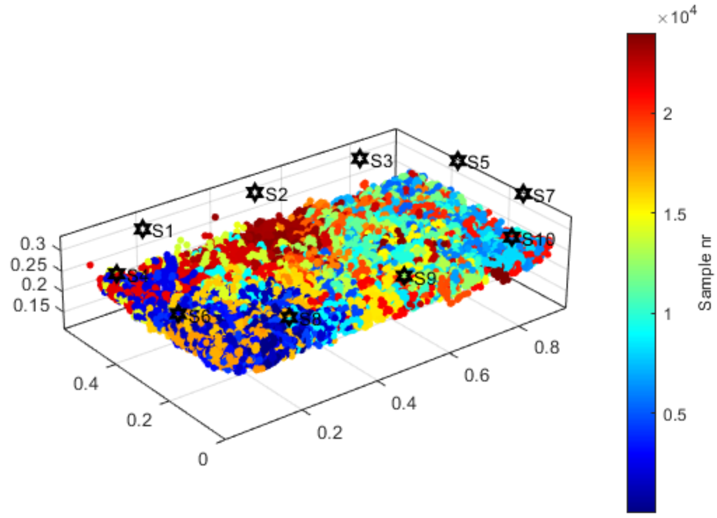

Figure 4.15: Positional data for one 20 minute measurement at medium bed height and a superficial velocity of 0.44 $\frac{m}{s}$.

The mixing cell structure was examined using the velocity field plot from 2 hours and 40 minutes of collected data with a superficial velocity of 0.441 $\frac{m}{s}$ shown in Figure 4.16.

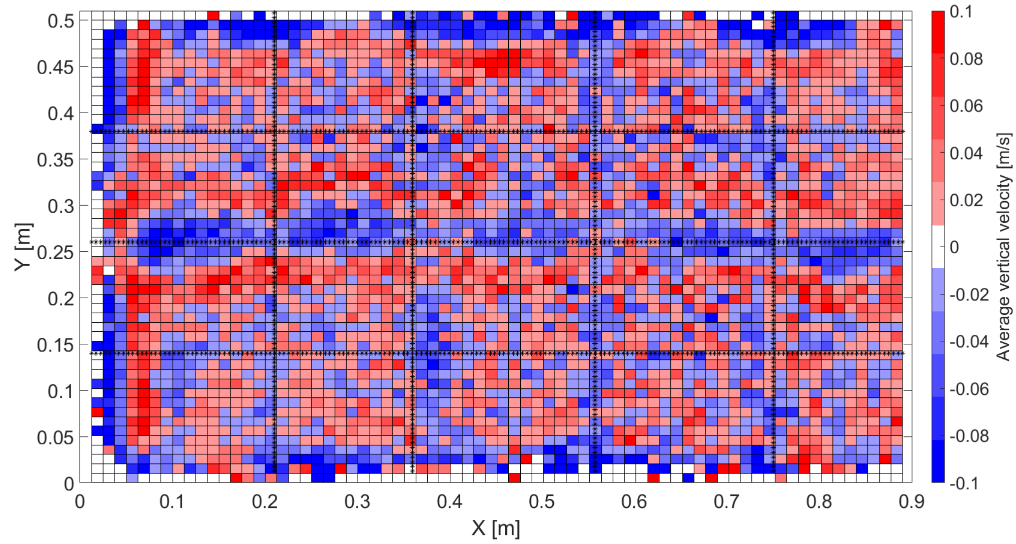

Figure 4.16: Velocity field for 2 hours and 40 minutes of measurements at medium bed height and a superficial velocity of 0.44 $\frac{m}{s}$. Mixing cells are present, but the structure is complex. The assigned mixing cells are marked in black.

More mixing cells are present compared to the high bed and the structure they form is more complex. The assumed cause for the lack of clarity is that the sinking zone along the x-axing disrupts the mixing cell pattern. It is therefore more difficult to assign the cells for calculation. As a rough estimation, the bed is divided into 4 cells along the y-axis and 5 cells along the x-axis, resulting in a total of 20 mixing cells with a L_{cell} 0.152 m.

The bed coverage was further evaluated using a histogram, shown in Figure 4.17.

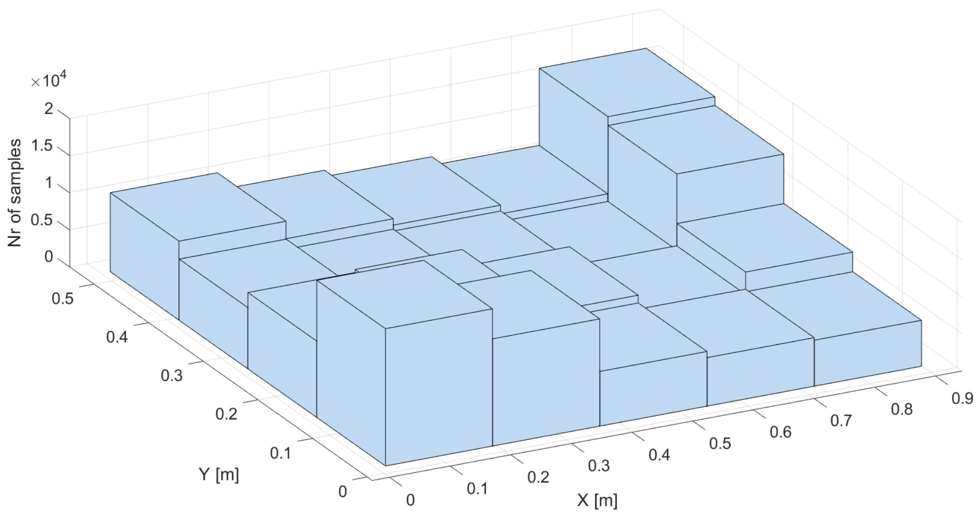

Figure 4.17: Histogram showing the number of point measured for each section of the bed at medium bed height and a superficial velocity of 0.44 $\frac{m}{s}$.

The largest number of points measured are at the corners of the bed and fewer points are measured at the center. The distribution in in Figure 4.17 is similar but more extreme compared to Figure 4.6 which indicates that a lower bed height with smaller mixing cells has lower mixing if the rest of the conditions are similar.

The dimensionless residence time of each assigned mixing cell was calculated using the 2 hours and 40 minutes of collected data at a superficial velocity of 0.43 $\frac{m}{s}$. The result is shown in Figure 4.18.

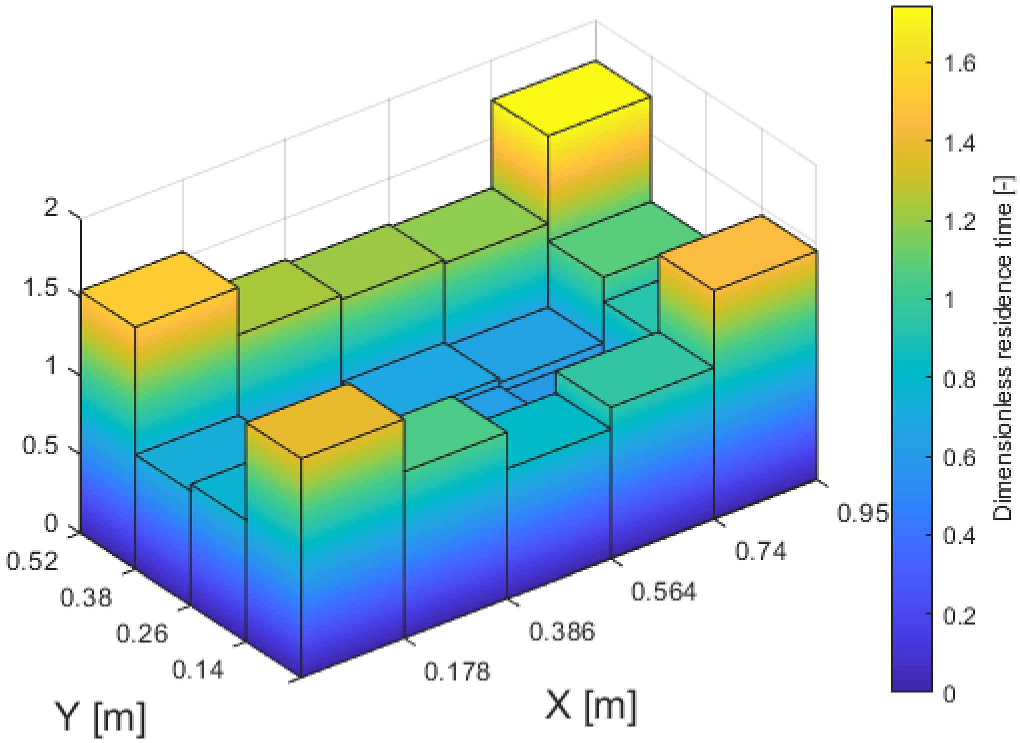

Figure 4.18: Dimensionless residence time for each mixing cell at medium bed height and a superficial velocity of 0.44 $\frac{m}{s}$.

The average residence time in each mixing cell is higher for cells that are facing the wall. The highest residence times are collected at the corners where two sides of the cell are facing the wall, just as observed in Figure 4.7. It is, however, possible that the sinking zone affects the residence times of the mixing cells bordering it. To study a mixing cell only surrounded by other mixing cells, it would therefore be preferable to do this during conditions under which more mixing cells are present. This could possibly be achieved by further lowering the bed height.

The dispersion coefficient was calculated using Einstein's equation for Brownian motion with the cells adjacent to the walls excluded. The resulting values are presented for varying threshold lengths between 0.01 and 0.25 m in Figure 4.19. The confidence intervals for separate measurements and the mean values on each side are available in Appendix G.

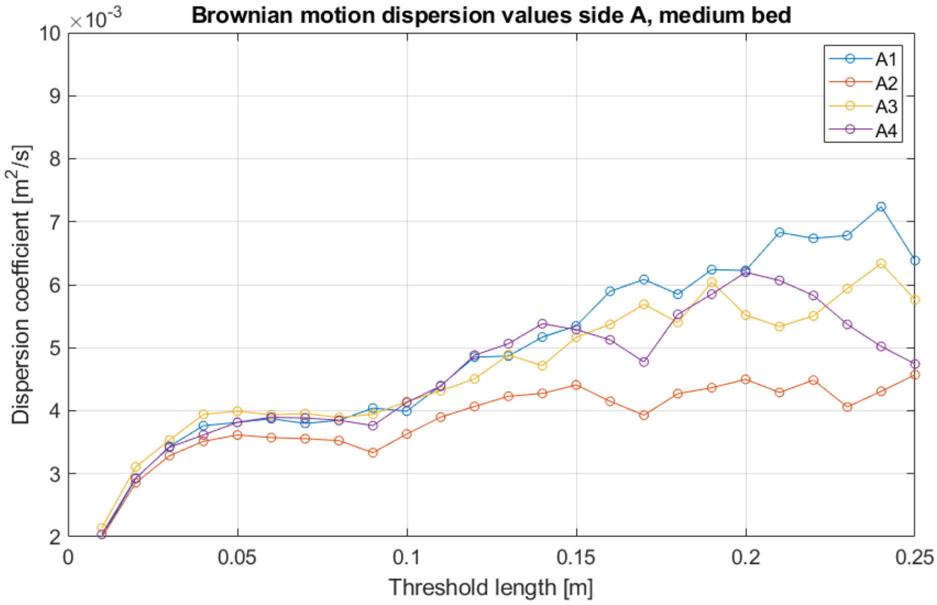

(a) Dispersion coefficient values from the measurements for the medium height bed with the tracer inserted at side A.

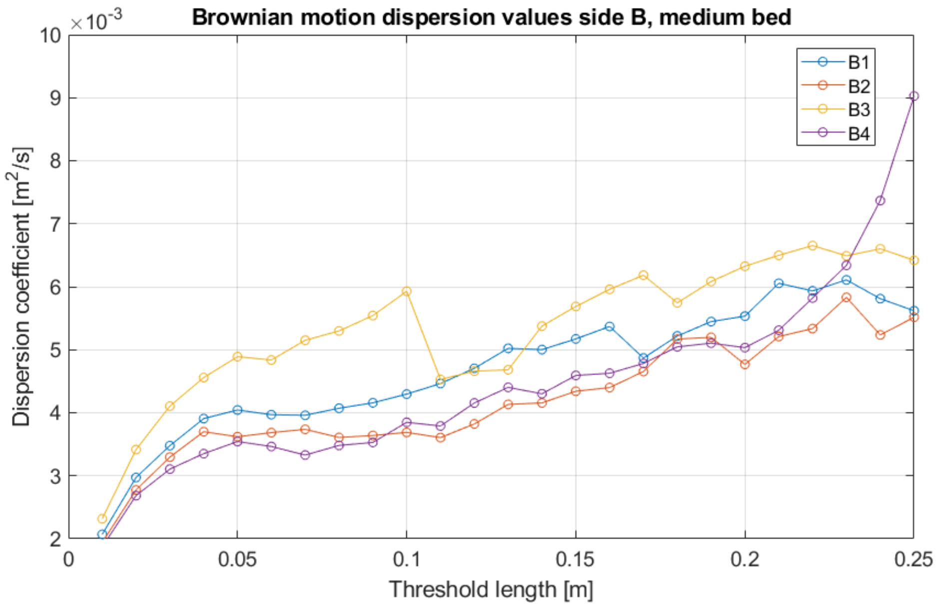

(b) Dispersion coefficient values from the measurements for the medium height bed with the tracer inserted at side B.

Figure 4.19: Dispersion coefficient values from the measurements for the medium height bed calculated with Einstein's equation for Brownian motion. Every individual measurement is 20 minutes long.

Measurement B3 in Figure 4.19b has diverging values and high variance at lower threshold lengths and was excluded from the mean values presented in Figure 4.20.

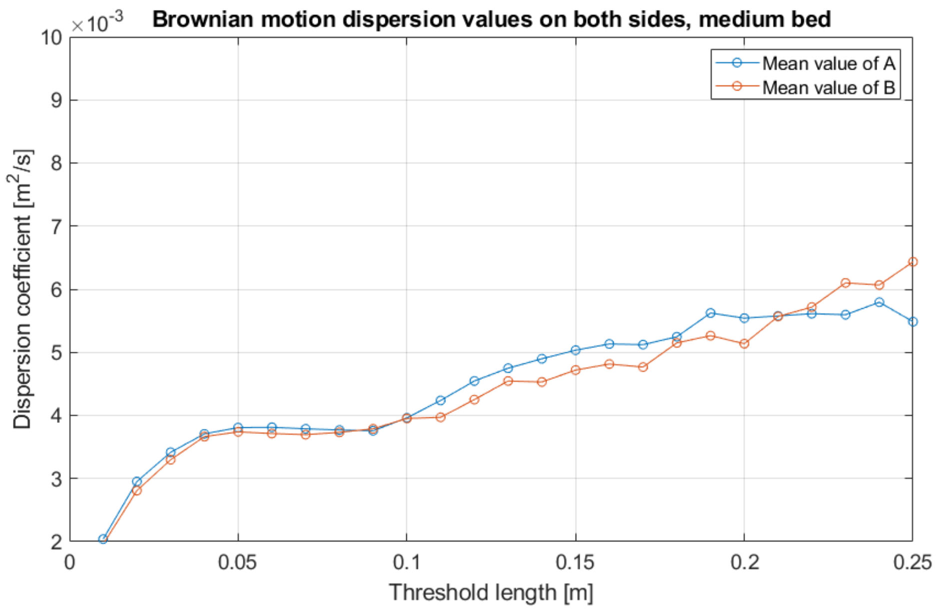

(a) Mean values of the dispersion coefficient from the measurements for the medium height bed and each side of tracer insertion.

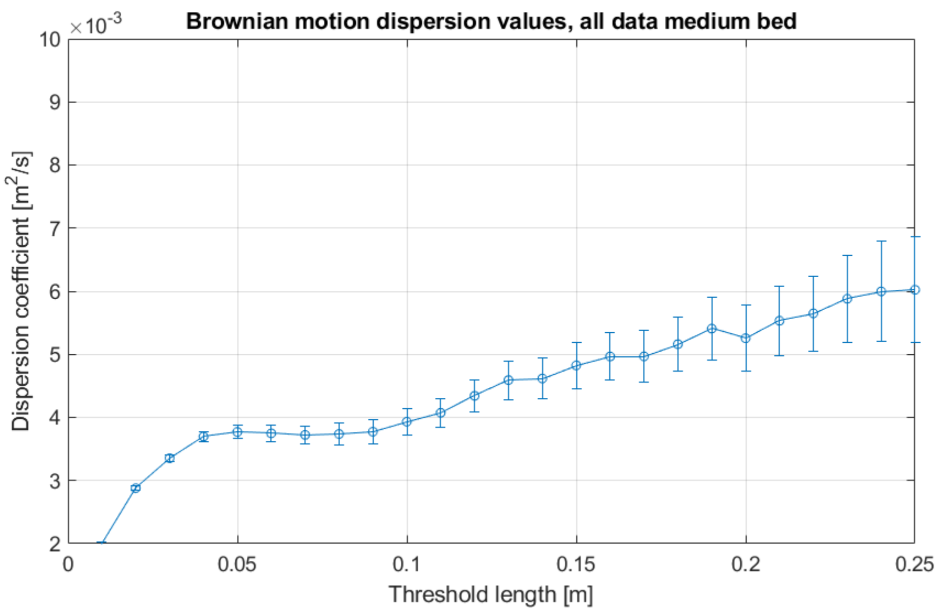

(b) Mean dispersion coefficient values for all measurements for the medium height bed.

Figure 4.20: Mean values of the dispersion coefficient for the medium height bed calculated with Einstein's equation for Brownian motion. A total amount of 2 hours and 20 minutes of data was used.

Figure 4.20 has the same appearance as for the high bed in Figure 4.9 with a region of constant dispersion coefficient values at lower threshold lengths that then starts to increase as the threshold length increases. In Figure 4.20b the dispersion coefficient reaches a constant value between 0.05 and 0.09 m of $3.7 \times 10^{-3} \pm 1.4 \times 10^{-4}$ $\frac{m^2}{s}$ which indicates a shorter mixing cell length than the number of 0.152 m for L_{cell} obtained using the velocity field plot. A possible reason for this is that the mixing cell size is roughly partitioned into rectangular cells from the velocity field plot, which could result in an overestimation of the mixing cell length using this method. This further proves that the exact mixing cell length needs to be studied in further detail. This time the values from side A are slightly higher for most threshold lengths which could be a further indication of uneven flow in the bed.

Since the measurements for the medium bed height were 20 minutes long, the calculations for shorter individual measurement lengths were performed for 15, 10 and 5 minutes. The resulting graphs are presented in Figure 4.21.

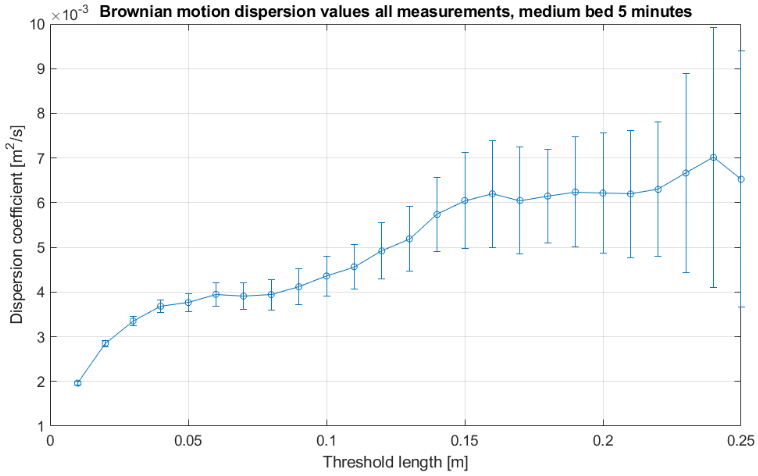

(a) 15 minute individual measurement length.

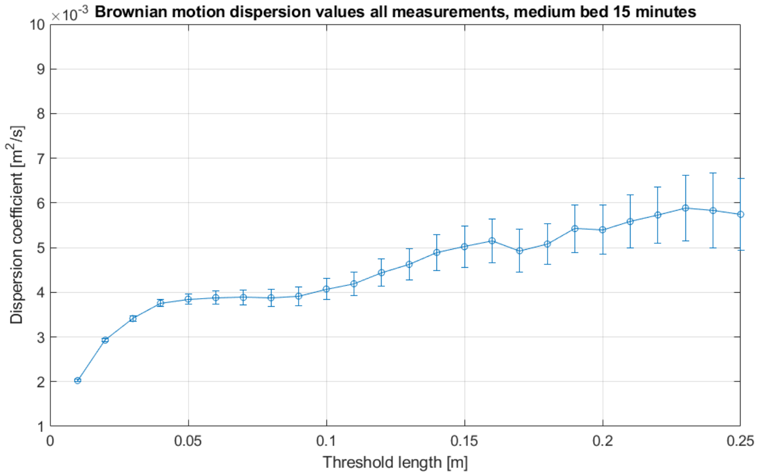

(b) 10 minute individual measurement length.

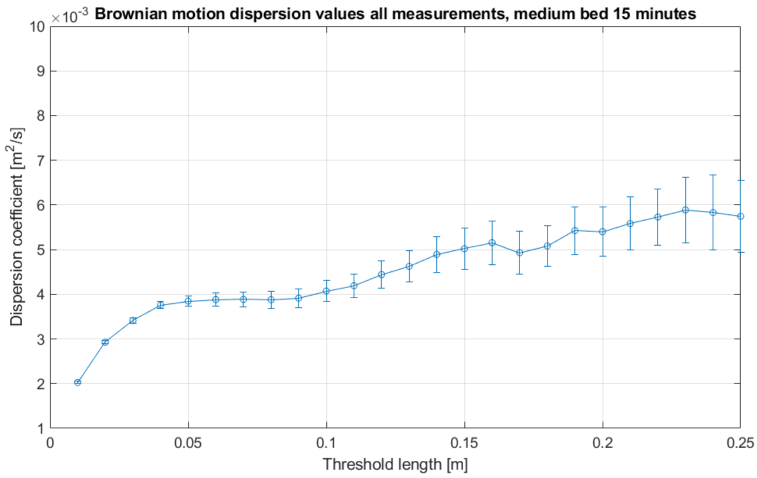

(c) 5 minute individual measurement length.

Figure 4.21: Values of the dispersion coefficient for the medium high bed and shorter individual measurement times calculated with Einstein's equation for Brownian motion. The total measurement time is 105 minutes for (a), 70 minutes for (b) and 35 minutes for (c).

The graphs in Figure 4.21 are similar, just as in the case for the high bed. The value and variance of the dispersion coefficient increases a lot at higher threshold lengths in Figure 4.21c this should be due to the small amount of data available. To test the influence of experiment times with a higher degree of certainty, an equal amount of data should be acquired for the shorter experiment times as for the longer experiment times. However, since a large amount of total data needs to be gathered to get estimations with low degrees of variance, shorter experiment times are not recommended since the collection of data gets more time consuming with shorter experiment times.

Although only a rough estimation of the mixing cells was possible, the dispersion coefficient was also calculated using the mixing cells method with the cells adjacent to the walls excluded. The resulting values are presented for minimum residence times between 0.3 and 1.5 seconds in Figure 4.22 and 4.23. Complementary graphs with confidence intervals for each separate measurement and the mean values on each side are available in Appendix H.

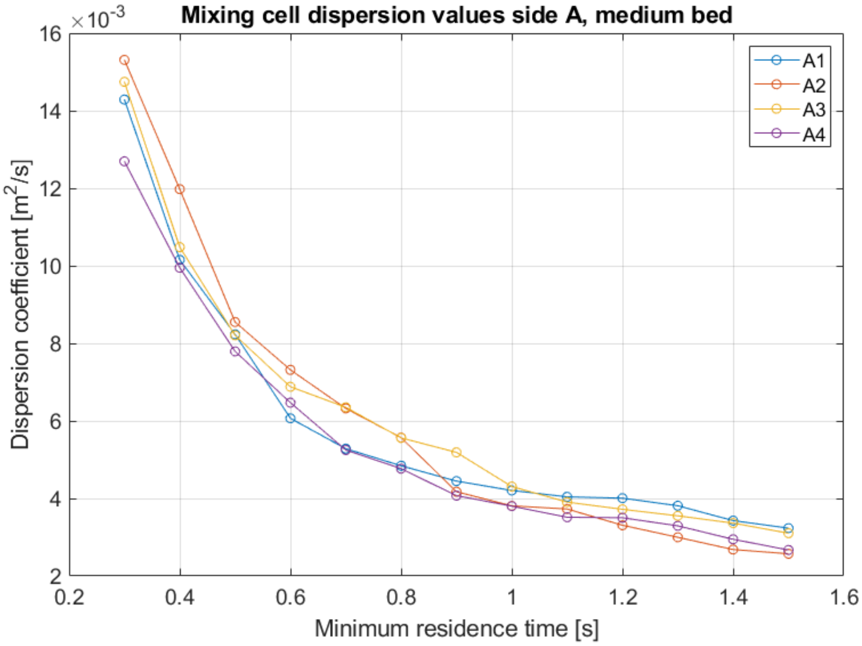

(a) Dispersion coefficient values from the measurements for the medium bed height with the tracer inserted at side A.

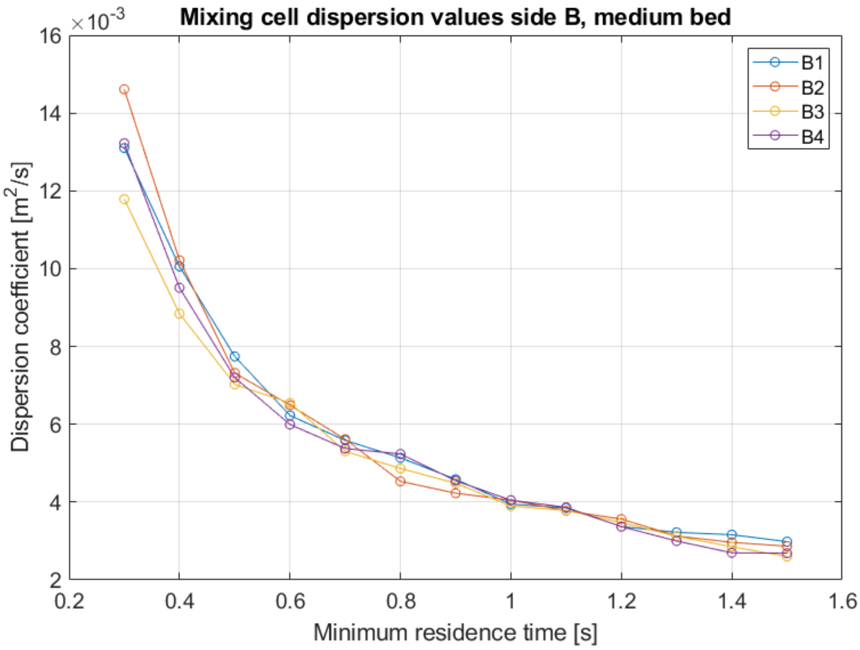

(b) Dispersion coefficient values from the measurements for the medium bed height with the tracer inserted at side B.

Figure 4.22: Dispersion coefficient values from the measurements for the medium bed height calculated using mixing cells. Every individual measurement is 20 minutes long.

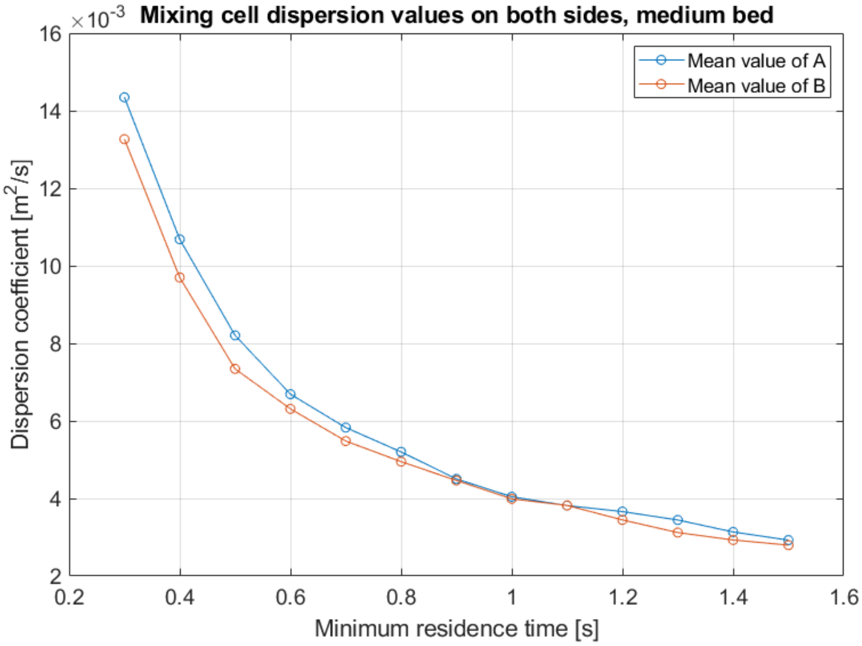

(a) Mean dispersion coefficient values from the measurements for the medium high bed and each side of tracer insertion.

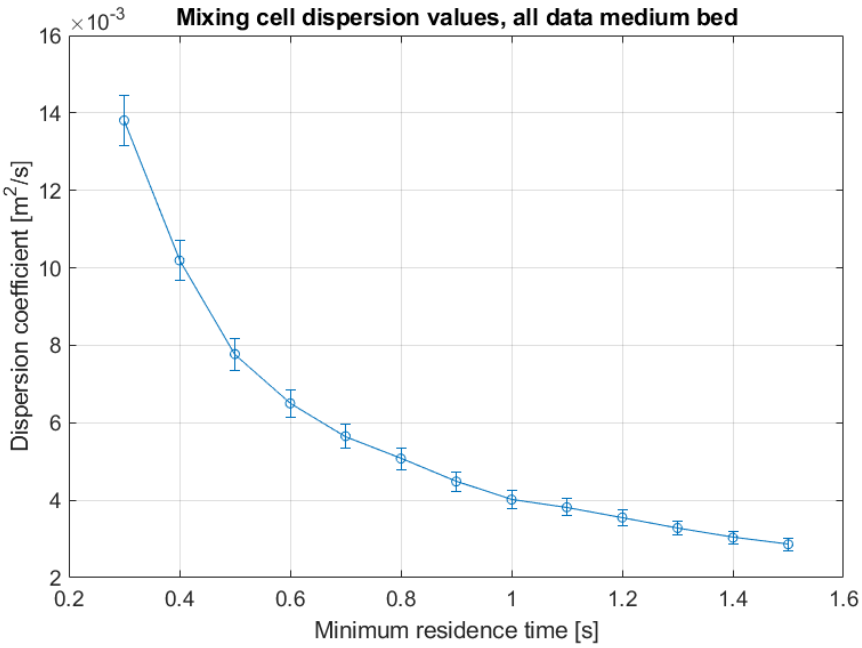

(b) Mean dispersion coefficient values for all measurements for the medium high bed.

Figure 4.23: Mean values of the dispersion coefficient for the medium bed height calculated using mixing cells. A total amount of 2 hours and 40 minutes of data was used.

The graphs in Figure 4.22 and 4.23 are similar to the corresponding graphs for the high bed in Figure 4.12 and 4.13 but with lower values just as with the Brownian motion calculations. The mean dispersion coefficient value of 3.7×10^{-3} $\frac{m^2}{s}$ is located at the bottom graph of Figure 4.23 at a minimum residence time of 1.15 seconds. This is a shorter residence time than for the high bed, which could indicate that the mixing cells were estimated more exactly than for the high bed.

Different measurement lengths were also evaluated for the calculations using mixing cells and the results are presented in Figure 4.24 for individual measurement times between 5-15 minutes instead of the normal 20 minutes.

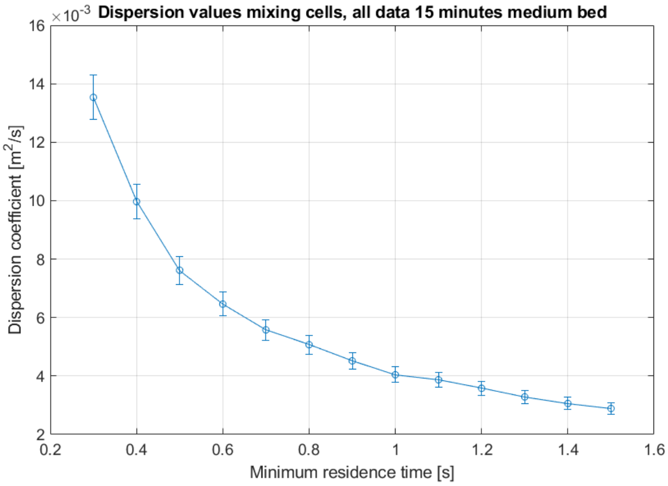

(a) 15 minute individual measurement length.

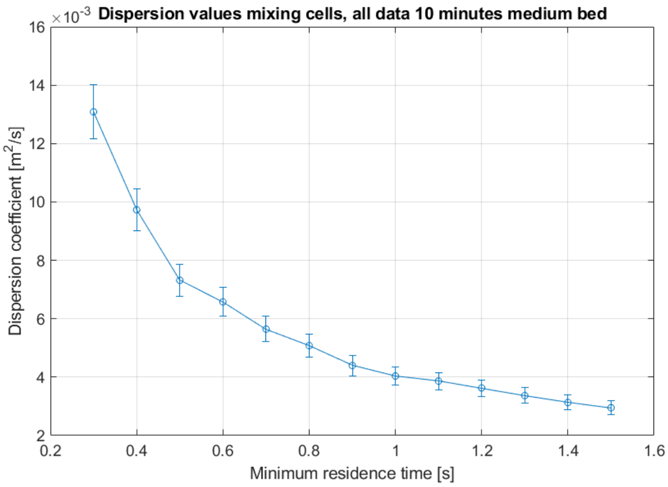

(b) 10 minute individual measurement length.

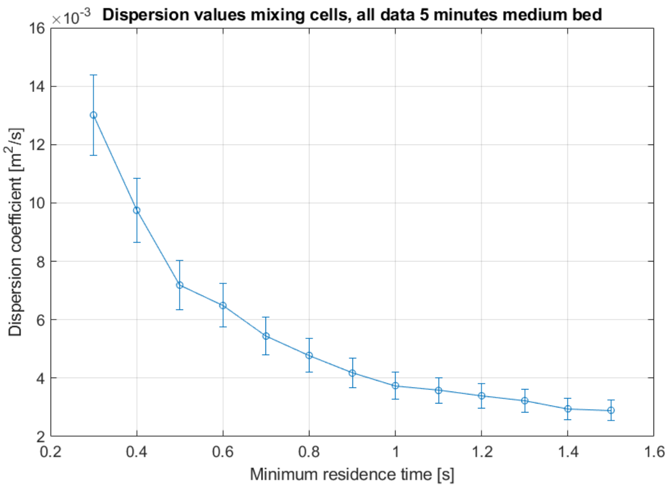

(c) 5 minute individual measurement length.

Figure 4.24: Values of the dispersion coefficient for the medium high bed and shorter individual measurement times calculated using mixing cells. The total measurement time is 120 minutes for (a), 80 minutes for (b) and 40 minutes for (c).

The graphs in Figure 4.24 have similar shape as for previous cases with higher variance for shorter times due to lower amounts of data. The values at longer minimum residence times are somewhat lower in Figure 4.24c.

4.3 Low bed height

Measurements at the low bed height continued to be performed with the GVC tracer. At this bed height the tracer exhibited worse bed coverage so the amount of 20 minute measurements on each side were increased from 4 to 6 for a total of 12 measurements or 4 hours of data. The analysis is structured in the same way as for the medium bed height but the lower bed coverage made it harder to identify mixing cells in the bed. This worse bed coverage coverage for the low bed height is demonstrated in Figure 4.25. The large holes in the middle of the bed suggests that the mixing rate is lower.

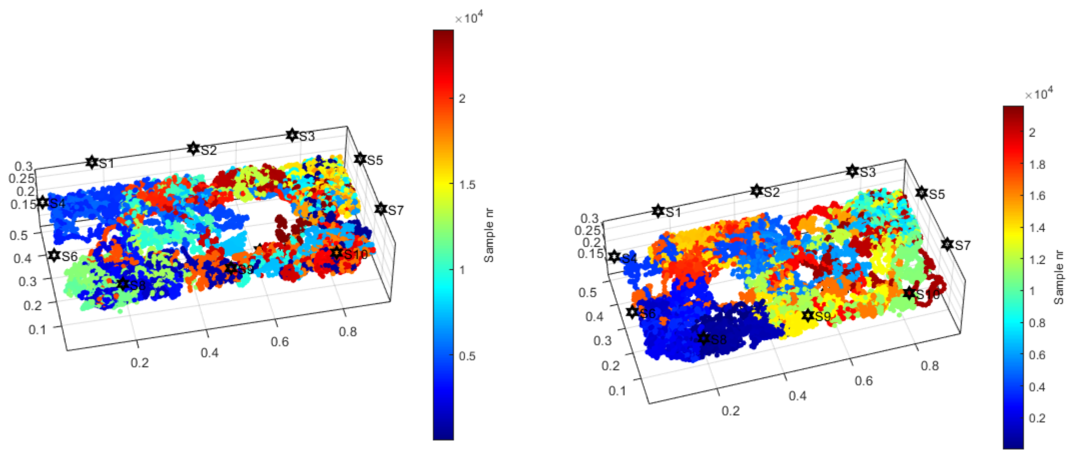

(a) Measurement performed with side A as initial position

(b) Measurement performed with side B as initial position.

Figure 4.25: The positional data for two measurements at the low height bed and a superficial velocity of 0.433. $\frac{m}{s}$.

To examine how the mixing cell structure was influenced by the lowering of the bed height four hours of data, two hours on each side, was collected and compiled into a velocity field plot shown in Figure 4.26. Compared to the results for the normal height the mixing cell structure are smaller and the magnitude of the average velocity for each grid space is smaller. The mixing cells are less clearly observable, but smaller clusters are present compared to the previous bed heights. The bed is therefore divided into 30 mixing cells giving an average L_{cell} of 0.131 m. However there is a large degree of error present in the assigned border of each mixing cell.

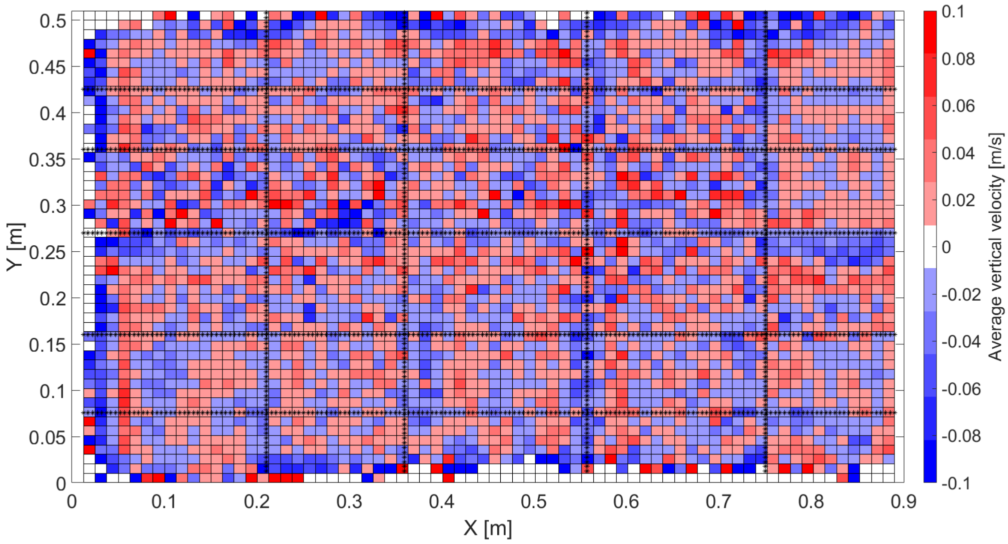

Figure 4.26: Velocity field for 4 hours of measurements at low bed height with a superficial velocity of 0.433 $\frac{m}{s}$. Mixing cells are marked with black crosses.

Evaluating the bed coverage with all data at this bed height with a histogram plot shows that poor coverage of the center of the bed is achieved, as is shown in Figure 4.27.

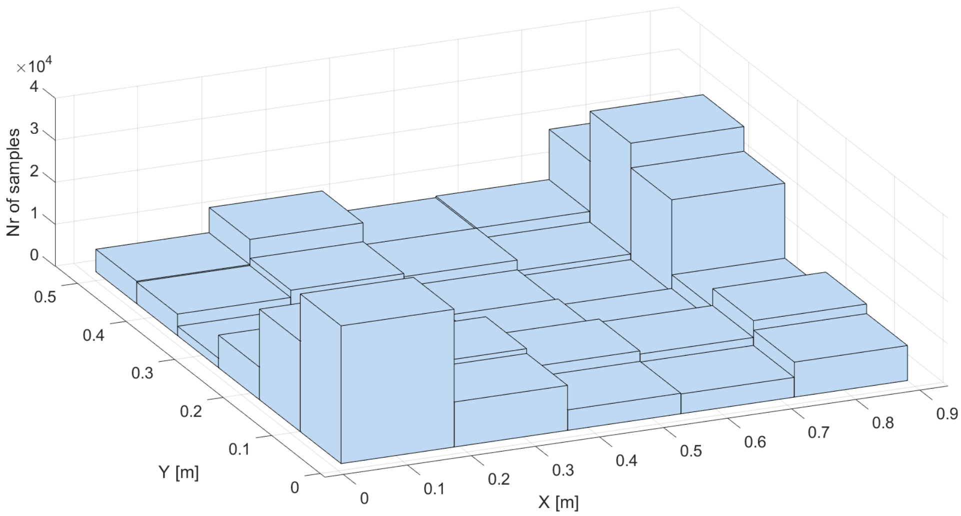

Figure 4.27: Histogram showing the number of samples measured in each area of the bed at low bed height with a superficial velocity of 0.433 $\frac{m}{s}$.

The zones of poor coverage are suspected to be due to full fluidization not being achieved. To examine whether this is true, the superficial velocity is raised to 0.548 $\frac{m}{s}$. 1 hour of measurements are run under these conditions. The resulting velocity field plot is shown in Figure 4.28.

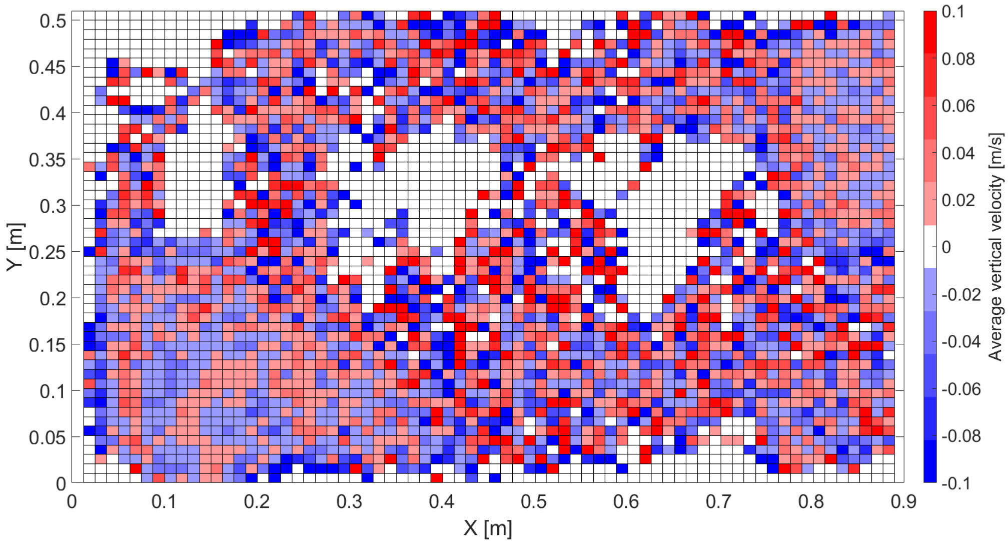

Figure 4.28: Velocity field for 1 hour of combined measurements for a low bed height and superficial velocity of 0.548 $\frac{m}{s}$.

The coverage of the bed is still poor and several zones in the center of the bed are completely uncovered. The superficial velocity can not be raised further without approaching the terminal velocity and risk entraining the tracer in the upward flow, causing it to reach heights where the measurements become unreliable.

The dimensionless residence time for each cell is shown in Figure 4.29. This is calculated from the 4 hours of data collected using an air flow of 0.433 $\frac{m}{s}$.

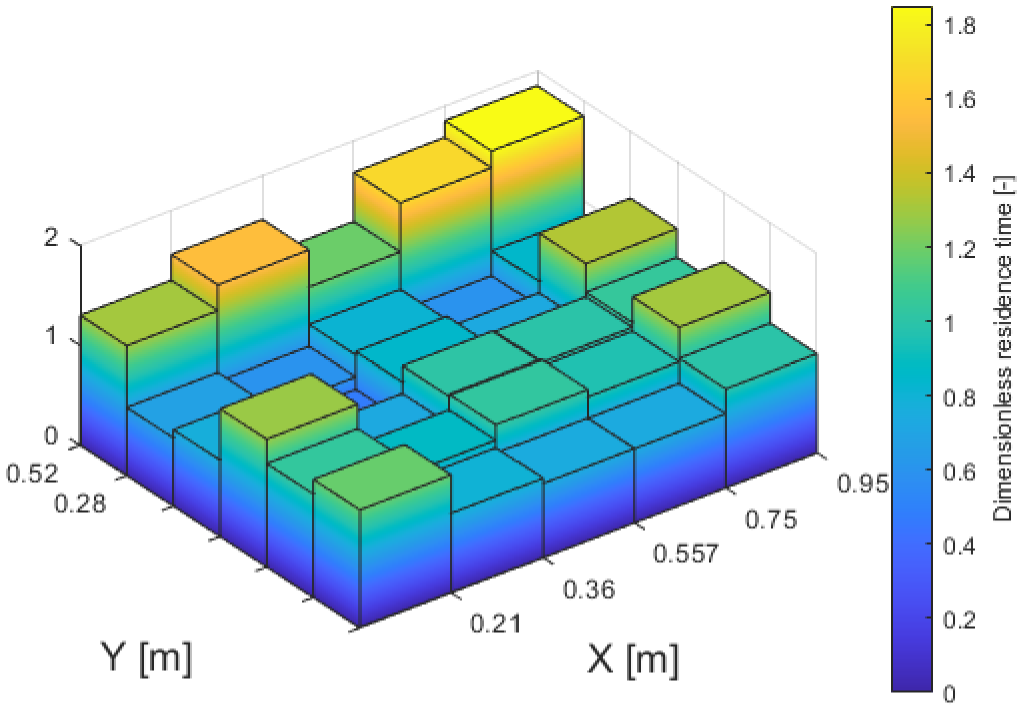

Figure 4.29: Dimensionless residence time for each mixing cell at low bed height at low bed height with a superficial velocity of 0.433 $\frac{m}{s}$.

The residence times in Figure 4.29 is higher for the mixing cells facing the wall at high y-coordinates which deviates from the earlier trend observed in Figure 4.7 and Figure 4.18 where all corners had more similar residence times. This is possibly a result of full fluidization not being achieved.

The dispersion coefficient was calculated using Einstein's equation for Brownian motion with the outer cells close to the walls excluded. The resulting values for varying threshold lengths between 0.01 and 0.26 m are presented in Figure 4.30. Graphs with confidence intervals for all separate measurements and the mean values for both sides are available in Appendix I.

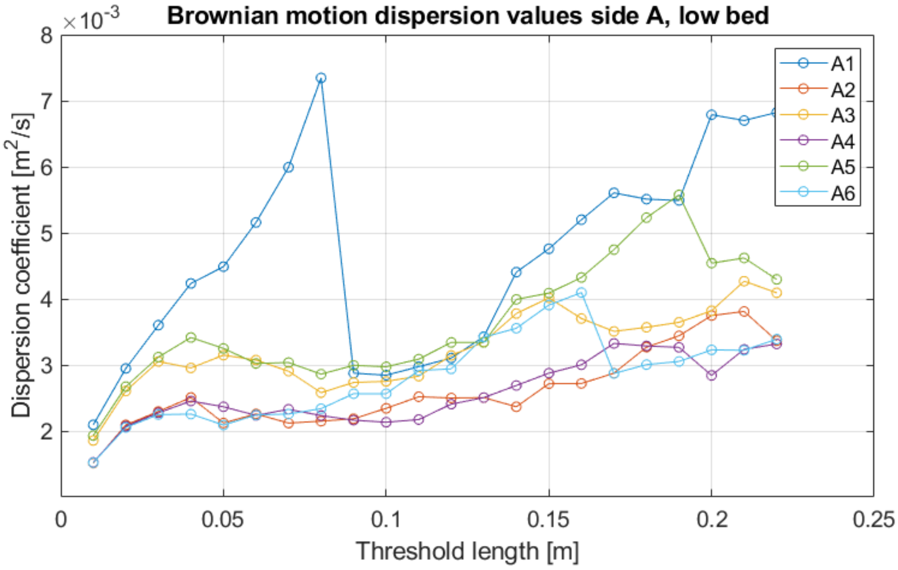

(a) Dispersion coefficient values from the measurements for the low bed with the tracer inserted at side A.

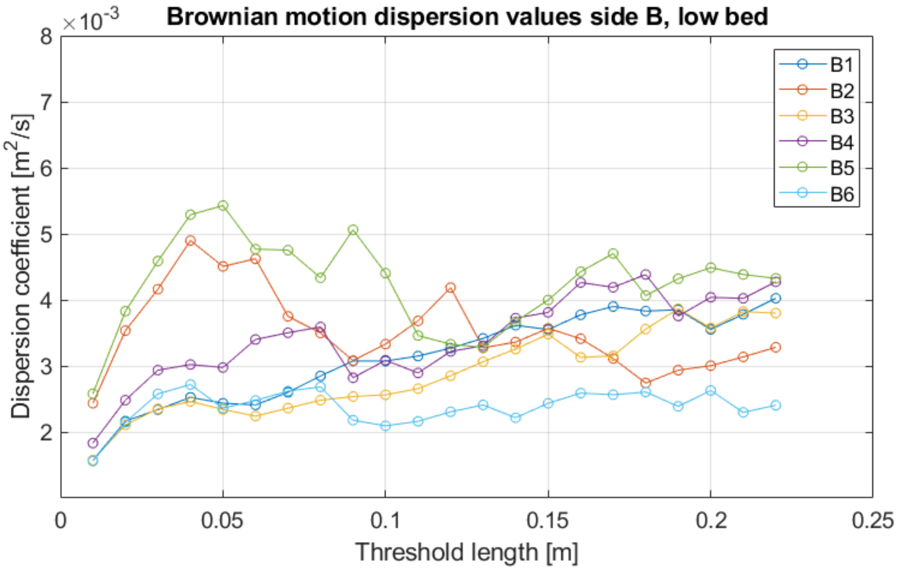

(b) Dispersion coefficient values from the measurements for the low bed with the tracer inserted at side B.

Figure 4.30: Dispersion coefficient values from the measurements for the low bed height calculated with Einstein's equation for Brownian motion. Every individual measurement is 20 minutes long.

Measurement A4 in Figure 4.30a showed a large deviation and was therefore excluded for the calculation of the mean dispersion coefficient presented in Figure 4.31.

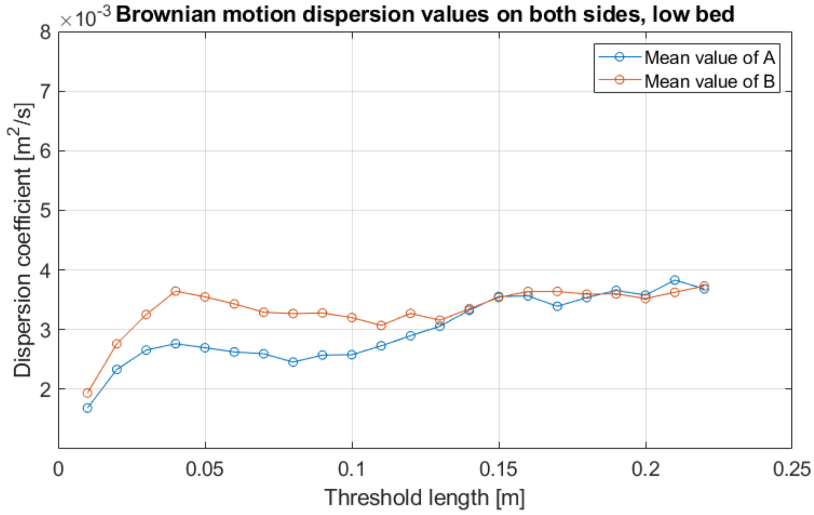

(a) Mean dispersion coefficient values from the measurements for the low bed and each side of tracer insertion.

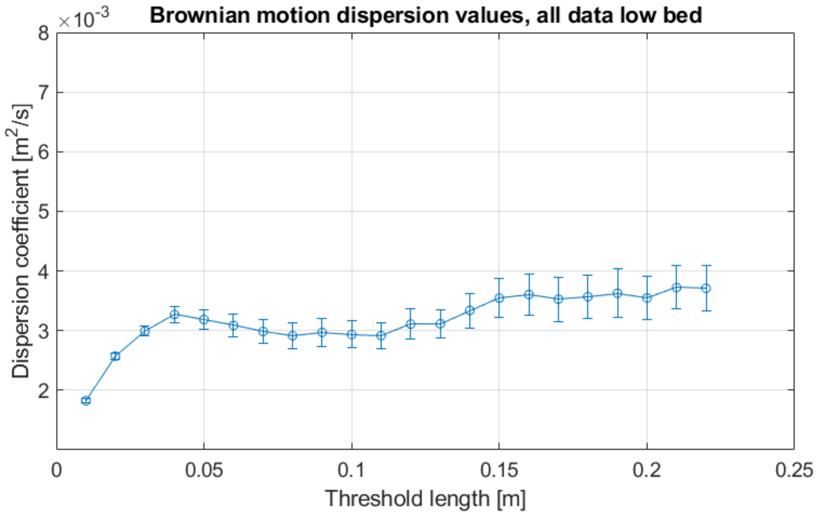

(b) Mean dispersion coefficient values for all measurements for the low bed.

Figure 4.31: Mean values of the dispersion coefficient for the low bed calculated with Einstein's equation for Brownian motion. A total amount of 3 hours and 40 minutes of data was used.

The graphs in both Figure 4.30 and 4.31 has the same overall shape as their corresponding graphs at previous bed heights but indicate that the mixing conditions are more unstable for the low bed height. Figure 4.31b has a somewhat different shape compared to the earlier bed heights as it does not level out in the same manner. From the graph L_{cell} is estimated to be 0.04 m and by comparing it to the estimation of 0.131 m from the velocity field plot in Figure 4.26 it can be concluded that the two estimations are different for this case too. An estimation of 0.04 m gives a dispersion coefficient value of $3.3 \times 10^{-3} \pm 1.4 \times 10^{-4}$ $\frac{m^2}{s}$, however this value is quite uncertain as the individual measurements vary a lot in this region. The dispersion coefficient value is larger on side B for this case but it is hard to make any robust conclusions as the variation along individual measurements is large.

Calculations at shorter measurement times were also performed for the low bed height. Dispersion coefficient values at at measurement times of 15, 10 and 5 minutes are presented in Figure 4.32 for varying threshold lengths.

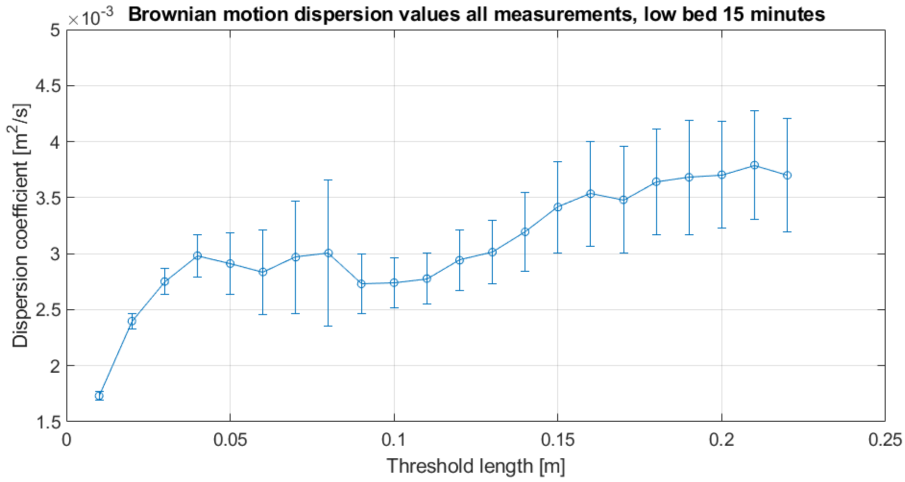

(a) 15 minute individual measurement length.

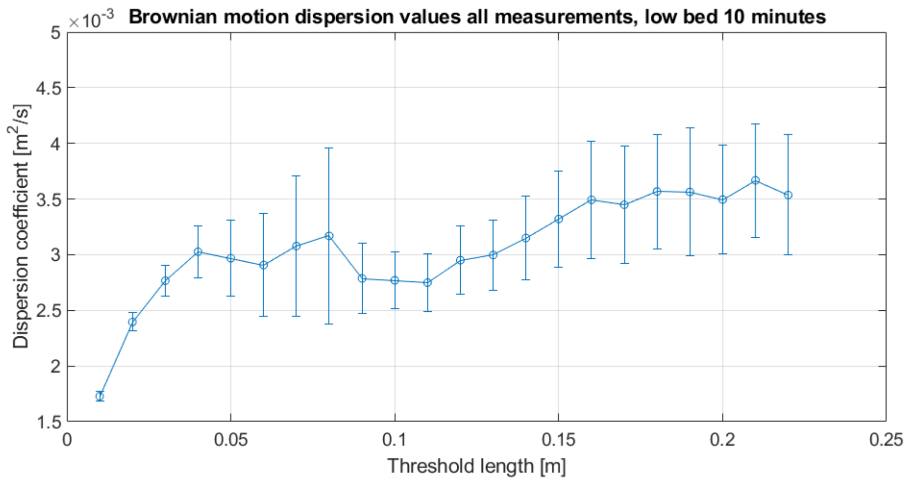

(b) 10 minute individual measurement length.

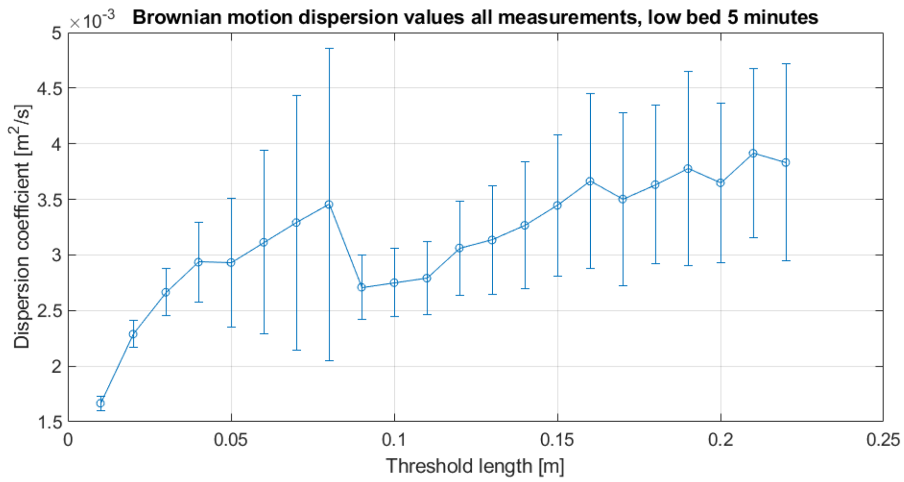

(c) 5 minute individual measurement length.

Figure 4.32: Values of the dispersion coefficient for the low bed and shorter measurements calculated with Einstein's equation for Brownian motion at low bed height. The total measurement time is 165 minutes for (a), 110 minutes for (b) and 55 minutes for (c).

The variance increases as the experiment time decreases as observed in all previous cases. The variance initially increases as the threshold length increases, but decreases after 0.08 m. After this threshold length the dispersion coefficient also decreases. The reason for this is not clear, although it is possible that the poor tracer coverage of the bed results in the tracer taking a long time to travel further than 0.08 m.

The dispersion coefficient calculations performed using mixing cells at low bed height are presented in Figure 4.33 and 4.34 for a minimum residence time between 0.3 and 1.5 seconds and with the mixing cells close to the wall excluded. Individual graphs for each measurement and for the mean values on each side with confidence intervals are available in Appendix J.

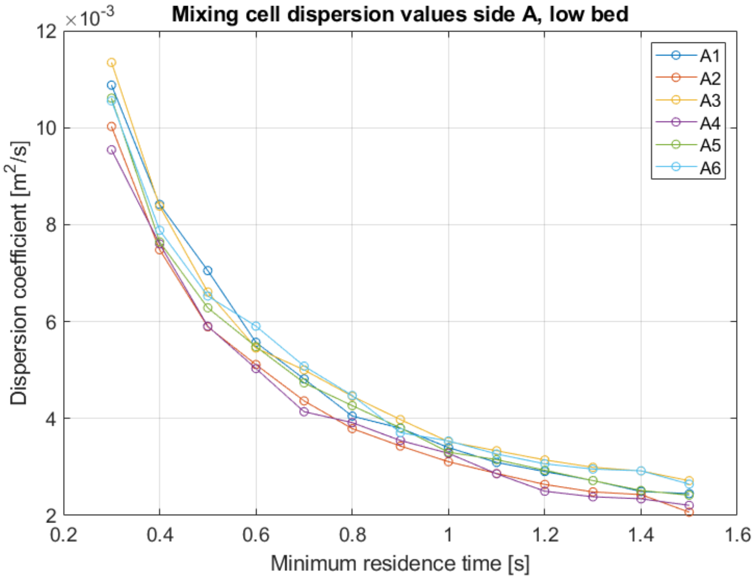

(a) Dispersion coefficient values from the measurements for the low bed with the tracer inserted at side A.

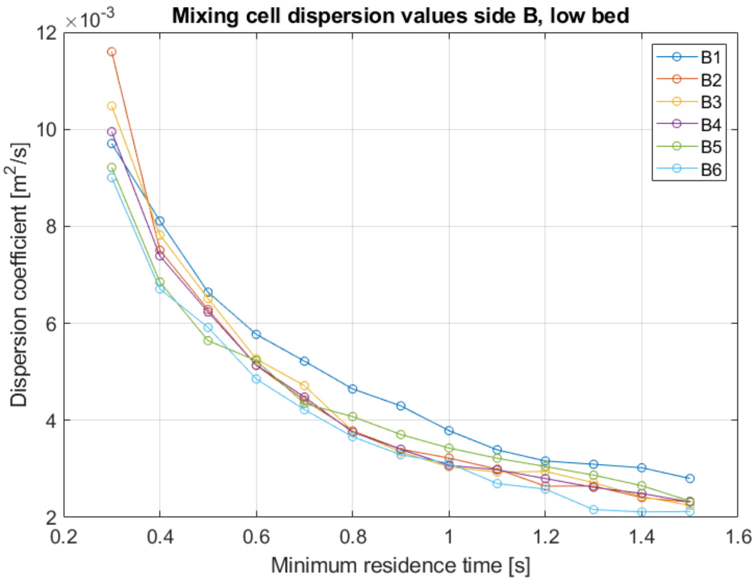

(b) Dispersion coefficient values from the measurements for the low bed with the tracer inserted at side B.

Figure 4.33: Dispersion coefficient values from the measurements for the low bed height calculated with the mixing cell equation. Every individual measurement is 20 minutes long.

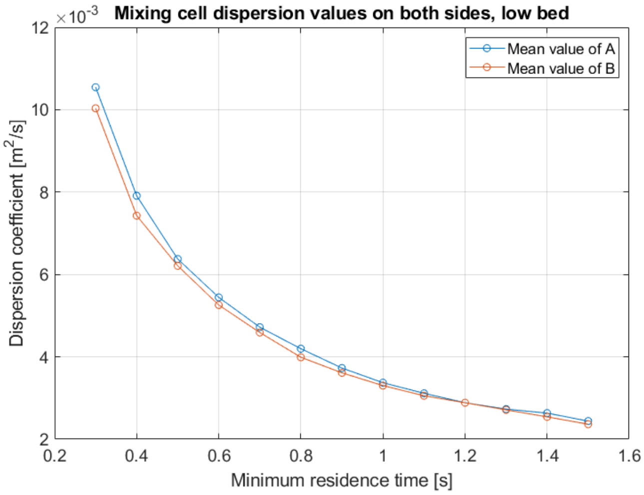

(a) Mean dispersion coefficient values from the measurements for the low bed and each side of tracer insertion.

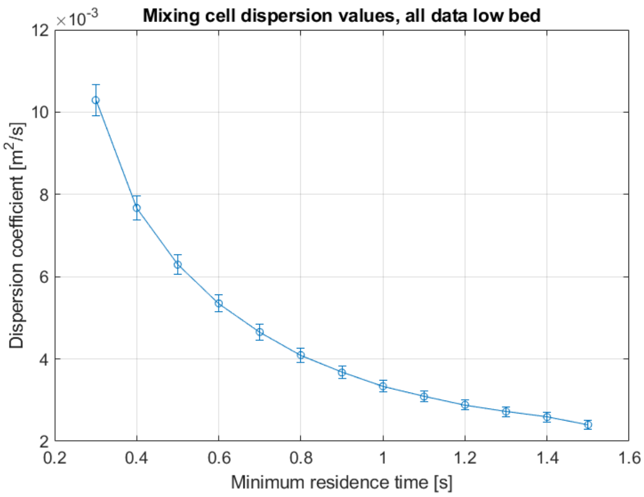

(b) Mean dispersion values for all measurements for the low bed.

Figure 4.34: Mean values of the dispersion coefficient for the low bed calculated using mixing cells. A total amount of 4 hours of data was used.

The graphs in Figure 4.33 and 4.34 are similar to the graphs at the previous bed heights and look more cohesive than the graphs in Figure 4.30 and 4.31. The mean dispersion coefficient value on side A is somewhat larger than on side B in Figure 4.34a. A value that matches the result from the calculation using Einstein's equation for Brownian motion of $3.3 \times 10^{-3}\ \frac{m^2}{s}$ is found at a minimum residence time of 1 second, which is similar but lower compared to the matching minimum residence times for the greater bed heights.

These calculations were also performed at shorter individual measurement lengths. The dispersion coefficient values at measurement times of 15, 10 and 5 minutes are presented in Figure 4.35.

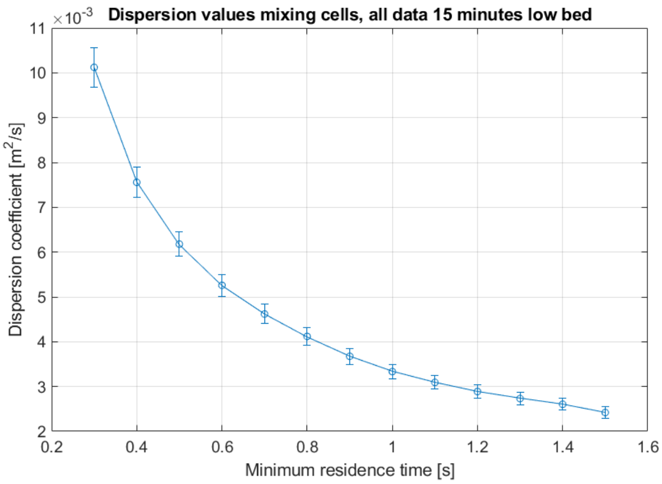

(a) 15 minute individual measurement length.

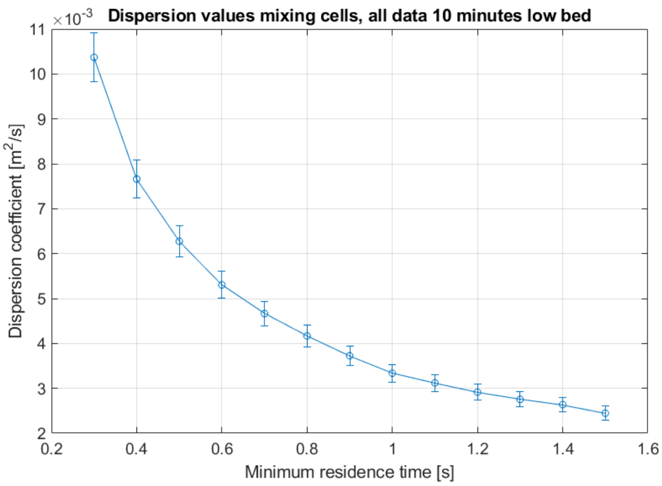

(b) 10 minute individual measurement length.

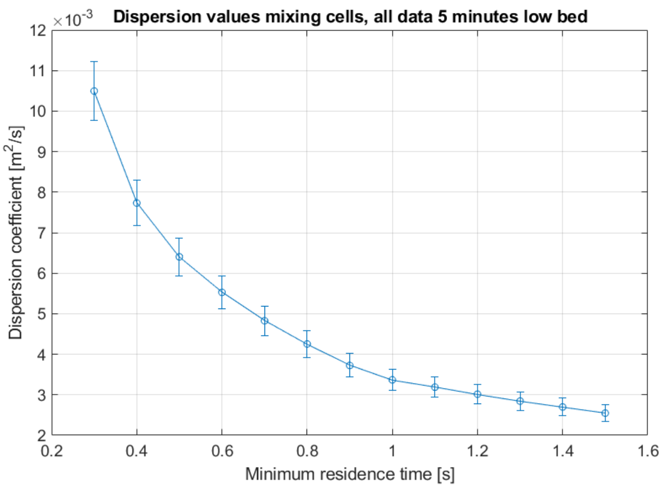

(c) 5 minute individual measurement length.

Figure 4.35: Values of the dispersion coefficient for the low bed and shorter individual measurements calculated using mixing cells equation at low bed height. The total measurement time is 180 minutes for (a), 120 minutes for (b) and 60 minutes for (c).

The calculated value of the dispersion coefficient in Figure 4.35 increases at small minimum residence times in Figure 4.35b and decreases in Figure 4.35c. This was also observed for the medium bed height. Apart from that the graphs are similar with increasing variance as the individual measurement time decreases.

5

Conclusions and further remarks

The following conclusions were reached based on the results of the experimental study:

- A framework for performing measurements using MPT-sensors in a downscaled cold model unit has been established.
- The experimental setup scales somewhat well with a superficial hot boiler with a smaller cross section than the commercial boiler, although with inadequate density scaling. Using copper powder as bed material would give better scaling relations.
- Mixing cells could be identified in the velocity field plots, but sizing and partitioning of these should be studied in greater detail.
- The average residence time in the mixing cells was proven to be higher for cells neighboring the walls, agreeing with the expectation that the residence time decreases as the length of perimeter open to transfer increases.
- The construction of the distributor plate in S13 prohibits even airflow along the bed which disrupts the mixing cell structure.
- Calculations using Einstein's equation for Brownian motion for different bed heights resulted in dispersion coefficient numbers ranging from $3.3 \times 10^{-3}\ \frac{m^2}{s}$ to $7.6 \times 10^{-3}\ \frac{m^2}{s}$ from the low to high bed and mixing cell lengths of 0.04, 0.05 and 0.08 for the low, medium and high bed respectively. The values for the dispersion were proportional to the bed height.
- A Matlab script was also created to calculate the lateral dispersion coefficient by calculations based on mixing cells. The values from these calculations matched the lateral dispersion coefficient values from the Brownian motion calculations for filtered times of 1.5 seconds with a mixing cell length of 0.214 m, 1.15 seconds with a mixing cell length of 0.152 m and 1 second with a mixing cell length of 0.131 m for high, medium and low bed heights respectively. The filtered time decreased with decreasing bed height.
- The dispersion coefficient values in the mixing cell method tend to converge towards the dispersion coefficient value from the Brownian motion method at larger sample amount threshold, even if the calculations are not based on the same mixing cell length. This indicates that slower tracer movements are less affected by incorrectly placed mixing cells.
- Calculating the value of the lateral dispersion coefficient using mixing cells gives less variation in the resulting data but requires mixing cells to be identified before calculations can be performed.
- The airflow in the downscaled cold model used in the study is suspected to be uneven.

- Cutting the individual measurement length from 20 to 5 minutes gave similar results but with higher variation due to smaller amounts of data. Longer measurements are still more efficient for obtaining large amounts of data.
- Lower bed heights gave a more uneven tracer distribution, possibly due to full fluidization of the bed not being achieved or lower mixing rates.
- More and smaller mixing cells could be observed as the bed height was decreased.
- A mixing cell surrounded by other mixing cells on all sides could not be studied during good conditions. Such mixing cells were identified for a low bed height, but the bed was not fully fluidized.

For further studies with the MPT-system in the downscaled cold model, mixing cells should be studied in greater detail and be partitioned using methods with a higher resolution, since the results indicate that rough estimations of the mixing cell shapes give results which do not match across different calculation methods. In addition to this, the air flow over the distributor plate in S13 should be further investigated to be able to better account for its irregularities. To achieve greater applicability for the calculated dispersion coefficients, future experiments should be performed with copper powder or another bed material with similar properties that better relates the gathered quantitative data to applications in industrial fluidized beds. An updated MPT-system with additional sensors on the z-axis could also allow for studies of axial dispersion of fuel particles by increasing the bed height.

Bibliography

[1] D. L. Klass, 2.2 basic concept, 1998.

[2] E. Sette, “Solids mixing in bubbling fluidized beds”, Ph.D. dissertation, Chalmers University of Technology, Sweden, 2016, ISBN: 978-91-7597-347-0.

[3] S. Ravelli, A. Perdichizzi, and G. Barigozzi, “Description, applications and numerical modelling of bubbling fluidized bed combustion in waste-to-energy plants”, *Progress in Energy and Combustion Science*, vol. 34, no. 2, pp. 224–253, 2008, ISSN: 0360-1285. DOI: `https://doi.org/10.1016/j.pecs.2007.07.002`.

[4] A. Awasthi and T. Bhaskar, “Chapter 11 - combustion of lignocellulosic biomass”, in *Biofuels: Alternative Feedstocks and Conversion Processes for the Production of Liquid and Gaseous Biofuels (Second Edition)*, ser. Biomass, Biofuels, Biochemicals, A. Pandey, C. Larroche, C.-G. Dussap, E. Gnansounou, S. K. Khanal, and S. Ricke, Eds., Second Edition, Academic Press, 2019, pp. 267–284, ISBN: 978-0-12-816856-1. DOI: `https://doi.org/10.1016/B978-0-12-816856-1.00011-7`.

[5] E. Sette, D. Pallarès, F. Johnsson, F. Ahrentorp, A. Ericsson, and C. Johansson, “Magnetic tracer-particle tracking in a fluid dynamically down-scaled bubbling fluidized bed”, *Fuel Processing Technology*, vol. 138, pp. 368–377, 2015, ISSN: 0378-3820. DOI: `https://doi.org/10.1016/j.fuproc.2015.06.016`.

[6] A. Köhler, D. Pallarès, and F. Johnsson, “Magnetic tracking of a fuel particle in a fluid-dynamically down-scaled fluidised bed”, *Fuel Processing Technology*, vol. 162, pp. 147–156, 2017, ISSN: 0378-3820. DOI: `https://doi.org/10.1016/j.fuproc.2017.03.018`.

[7] A. Köhler, A. Rasch, D. Pallarès, and F. Johnsson, “Experimental characterization of axial fuel mixing in fluidized beds by magnetic particle tracking”, *Powder Technology*, vol. 316, pp. 492–499, 2017, Fluidization for Emerging Green Technologies, ISSN: 0032-5910. DOI: `https://doi.org/10.1016/j.powtec.2016.12.093`.

[8] D. Pallarès and F. Johnsson, “A novel technique for particle tracking in cold 2-dimensional fluidized beds - simulating fuel dispersion”, *Chemical Engineering Science*, vol. 61, pp. 2710–2720, 8 Apr. 2006, ISSN: 00092509. DOI: `10.1016/j.ces.2005.11.030`.

[9] D. Liu and X. Chen, “Lateral solids dispersion coefficient in large-scale fluidized beds”, *Combustion and Flame*, vol. 157, pp. 2116–2124, 11 Nov. 2010, ISSN: 00102180. DOI: `https://doi.org/10.1016/j.combustflame.2010.04.020`.

[10] J. Olsson, D. Pallarès, and F. Johnsson, "Lateral fuel dispersion in a large-scale bubbling fluidized bed", *Chemical Engineering Science*, vol. 74, pp. 148–159, 2012, ISSN: 0009-2509. DOI: https://doi.org/10.1016/j.ces.2012.02.027.

[11] E. Sette, D. Pallarès, and F. Johnsson, "Experimental quantification of lateral mixing of fuels in fluid-dynamically down-scaled bubbling fluidized beds", *Applied Energy*, vol. 136, pp. 671–681, 2014, ISSN: 0306-2619. DOI: https://doi.org/10.1016/j.apenergy.2014.09.075.

[12] F. Niklasson, H. Thunman, F. Johnsson, and B. Leckner, "Estimation of solids mixing in a fluidized-bed combustor", English, *Industrial and Engineering Chemistry Research*, vol. 41, no. 18, pp. 4663–4673, 2002.

[13] K. A. Buist, P. Jayaprakash, J. Kuipers, N. G. Deen, and J. T. Padding, "Magnetic particle tracking for nonspherical particles in a cylindrical fluidized bed", *AIChE Journal*, vol. 63, no. 12, pp. 5335–5342, 2017. DOI: https://doi.org/10.1002/aic.15854.

[14] D. Kunii and O. Levenspiel, Fluidization engineering. Ser. Butterworths monographs in chemistry. Butterworth-Heinemann, 1991, ISBN: 0409902330.

[15] C. Schaschke, Fluidized catalytic cracker unit (FCCU). Oxford University Press, 2014, ISBN: 978-0-19-965145-0.

[16] T. Djerf, "Solids flows in circulating fluidized beds: Explorations of phenomena with applications to boilers", Ph.D. dissertation, Chalmers University of Technology, Sweden, 2021, ISBN: 978-91-7905-511-0.

[17] P. Rowe and B. Partridge, "An x-ray study of bubbles in fluidised beds", *Chemical Engineering Research and Design*, vol. 75, S116–S134, 1997, ISSN: 0263-8762. DOI: https://doi.org/10.1016/S0263-8762(97)80009-3.

[18] D. Pallarès and F. Johnsson, "A novel technique for particle tracking in cold 2-dimensional fluidized beds—simulating fuel dispersion", *Chemical Engineering Science*, vol. 61, no. 8, pp. 2710–2720, 2006, ISSN: 0009-2509. DOI: https://doi.org/10.1016/j.ces.2005.11.030.

[19] A. Einstein, Investigations on the theory of the Brownian movement. 1956, ISBN: 0486603040.

[20] S. Shrestha, B. S. Ali, and M. D. Binti Hamid, "Cold flow model of dual fluidized bed: A review", *Renewable and Sustainable Energy Reviews*, vol. 53, pp. 1529–1548, 2016, ISSN: 1364-0321. DOI: https://doi.org/10.1016/j.rser.2015.09.034.

[21] L. Glicksman, M. Hyre, and P. Farrell, "Dynamic similarity in fluidization", *International Journal of Multiphase Flow*, vol. 20, pp. 331–386, 1994, ISSN: 0301-9322. DOI: https://doi.org/10.1016/0301-9322(94)90077-9.

[22] L. Glicksman, M. Hyre, and K. Woloshun, "Simplified scaling relationships for fluidized beds", *Powder Technology*, vol. 77, no. 2, pp. 177–199, 1993, ISSN: 0032-5910. DOI: https://doi.org/10.1016/0032-5910(93)80055-F.

[23] T. Djerf, D. Pallarès, and F. Johnsson, "Bottom-bed fluid dynamics – influence on solids entrainment", *Fuel Processing Technology*, vol. 173, pp. 112–118, 2018, ISSN: 0378-3820. DOI: https://doi.org/10.1016/j.fuproc.2017.12.023.

[24] ——, "Solids flow patterns in large-scale circulating fluidised bed boilers: Experimental evaluation under fluid-dynamically down-scaled conditions", *Chem-*

ical Engineering Science, vol. 231, p. 116 309, 2021, ISSN: 0009-2509. DOI: https://doi.org/10.1016/j.ces.2020.116309.

[25] N. Ida, 5.6 magnetoresistance and magnetoresistive sensors, 2014.

[26] V. Gryc and P. Horáček, Variability in density of spruce (Picea abies [L.] Karst.) wood with the presence of reaction wood, [Online; accessed 6. Apr. 2021], Apr. 2021. DOI: https://doi.org/10.17221/2146-JFS.

A

Scaling calculations

Abbreviations used:

- C - cold model
- H - hot boiler
- b - bed material
- f - fuel particle
- sb - superficial boiler

$$d_{b,H} = 190\ \mu m,\ d_{b,C} = 105\ \mu m,\ L_C = 1076\ mm,\ W_C = 500\ mm$$

$$\frac{13}{\frac{d_{b,H}}{d_{b,C}}} = 7.18$$

The new superficial boiler has a size of 1950.8 $mm \times 906.5\ mm$ which is 7.18 times smaller than the commercial boiler and $\frac{13}{7.18} = 1.81$ times larger than S13.

B

Calculations for evaluation of simplified scaling laws

B.1 Comparison Between the Cold Model Glass Bead Bed and the Superficial Hot Boiler

B.1.1 Froude number

$$L = 1.81,\ u_{0,C} = 0.430 - 0.441\frac{m}{s},\ u_{0,H} = \sqrt{L} \times u_{0,C} = 0.579 - 0.593\frac{m}{s}$$
$$g = 9.81\frac{m}{s^2},\ D_C = 105\ \mu m,\ D_H = 190\ \mu m$$
$$(\frac{u_0^2}{gD})_C = 417.46 - 428.13$$
$$(\frac{u_0^2}{gD})_H = 179.55 - 188.86$$

B.1.2 Density ratio between bed material and fluidizing medium

$$\rho_{b,C} = \rho_{b,H} = 2600\frac{kg}{m^3},\ \rho_{f,C} = 1.204\frac{kg}{m^3},\ \rho_{f,H} = 0.3143$$
$$(\frac{\rho_b}{\rho_f})_C = 2159.45$$
$$(\frac{\rho_b}{\rho_f})_H = 8272.35$$

B.1.3 Ratio between minimum and maximum fluidization velocity

$$u_{0,C} = 0.430 - 0.441\frac{m}{s},\ u_{mf,C} = 0.012\frac{m}{s}$$
$$u_{0,H} = 0.579 - 0.593\frac{m}{s},\ u_{mf,H} = 0.0155\frac{m}{s}$$
$$(\frac{u_0}{u_{mf}})_C = 35.83 - 36.75$$
$$(\frac{u_0}{u_{mf}})_H = 37.35 - 38.26$$

B.2 Comparison between the copper powder bed and the hot boiler

B.2.1 Froude number

$$L = 13,\ u_{0,C} = u_{0,C},\ u_{0,H} = \sqrt{L} \times u_{0,H} = \sqrt{13}u_{0,C}$$
$$g = 9.81\frac{m}{s^2},\ D_B = 105\ \mu m,\ D_H = 190\ \mu m$$
$$(\frac{u_0^2}{gD})_C = 970.83u_{0,C}^2$$
$$(\frac{u_0^2}{gD})_H = 1934.41u_{0,C}^2$$

B.2.2 Density ratio between bed material and fluidizing medium

$$\rho_{b,C} = 8920\frac{kg}{m^3},\ \rho_{f,C} = 1.204\frac{kg}{m^3},\ \rho_{b,H} = 2600\frac{kg}{m^3},\ \rho_{f,H} = 0.3143$$
$$(\frac{\rho_b}{\rho_f})_C = 7408.64$$
$$(\frac{\rho_b}{\rho_f})_H = 8272.35$$

B.2.3 Ratio between minimum and maximum fluidization velocity

$$u_{0,C} = u_{0,C},\ u_{mf,C} = 0.0043\frac{m}{s}$$
$$u_{0,H} = \sqrt{13}u_{0,C},\ u_{mf,H} = 0.0155\frac{m}{s}$$
$$(\frac{u_0}{u_{mf}})_B = 232.56u_{0,C}$$
$$(\frac{u_0}{u_{mf}})_H = 232.61u_{0,C}$$

C
Plastic shield calculations

The size of the shields with spherical magnets were calculated by solving the following equation with the `fzero` function in Matlab

$$(\pi \cdot \frac{4}{3}((r^3 - (r-t)^3) + ((r-t)^3 - (r_{sphere} + 5 \cdot 10^{-4})^3) \cdot f \cdot \rho_{shell} + ((r-t)^2 - (r_{sphere} + 5 \cdot 10^{-4})^2) \cdot \pi \cdot t \cdot (1-f) \cdot \rho_{shell}) + m_{sphere} + m_{glue}) \cdot \frac{1}{\frac{4}{3} \cdot \pi \cdot r^3} - \rho_{tracer} = 0$$

were r is the radius of the sphere in m, t the thickness of the 100% filled layer at 2 mm, r_{sphere} the radius of the spherical magnet at 4 mm, f the amount of infill (mostly 10%), m_{sphere} the weight of the spherical magnet at 2.03 g, m_{glue} the weight of glue, 0.2 g, and ρ_{tracer} the tracer density that should be achieved in $\frac{kg}{m^3}$.

The expression used to calculate the size of the shields containing the cylindrical magnet is similar and is solved in the same way

$$(\pi \cdot \frac{4}{3}((r^3 - (r-t)^3) + ((r-t)^3 - (r_{cylinder} + 5 \cdot 10^{-4})^2 * \pi * (h_{cylinder} + 10^{-3})) \cdot f \cdot \rho_{shell} + ((r-t)^2 - (r_{cylinder} + 5 \cdot 10^{-4})^2) \cdot \pi \cdot t \cdot (1-f) \cdot \rho_{shell}) + m_{cylinder} + m_{glue}) \cdot \frac{1}{\frac{4}{3} \cdot \pi \cdot r^3} - \rho_{tracer} = 0$$

were $r_{cylinder}$ is the radius of the cylinder at 2.5 mm, $h_{cylinder}$ the height of the cylinder at 5 mm and $m_{cylinder}$ at 0.763 g.

D

Pressure graphs from S13

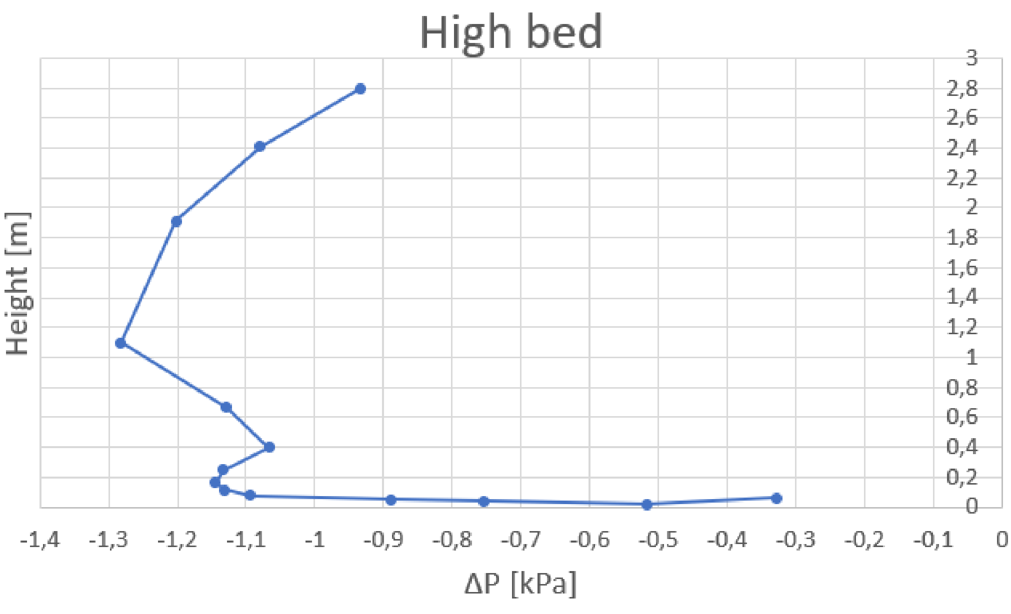

Figure D.1: Pressure graph for the high bed.

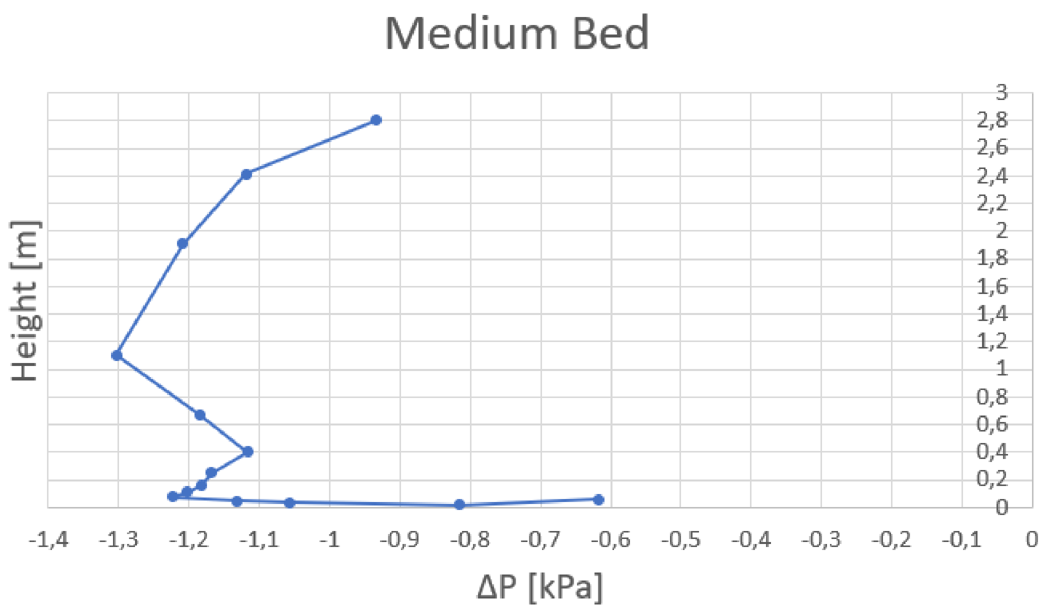

Figure D.2: Pressure graph for the medium bed.

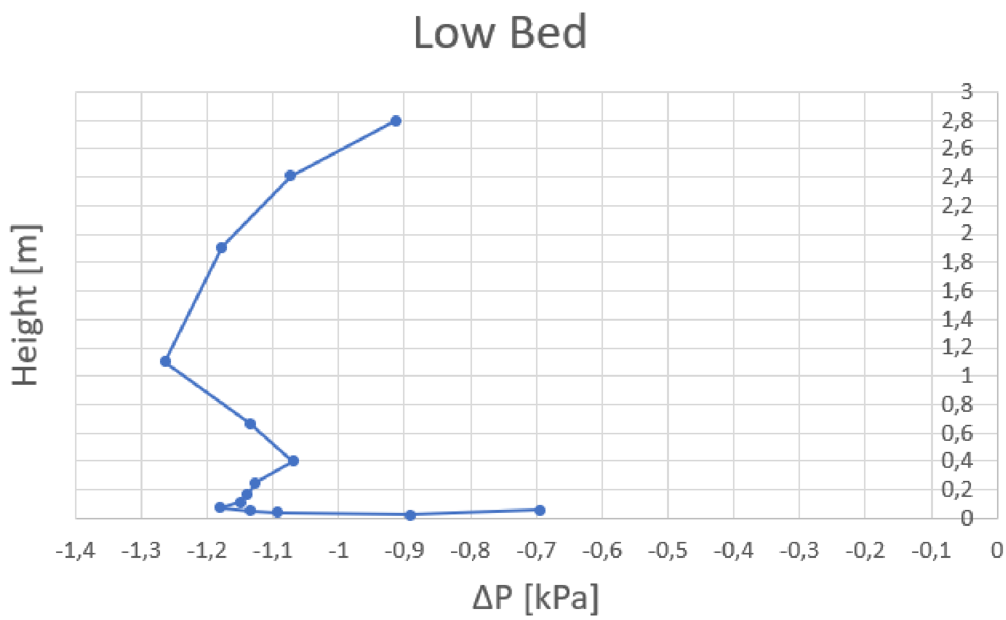

Figure D.3: Pressure graph for the low bed.

E

Confidence intervals for Brownian motion calculations for the high bed

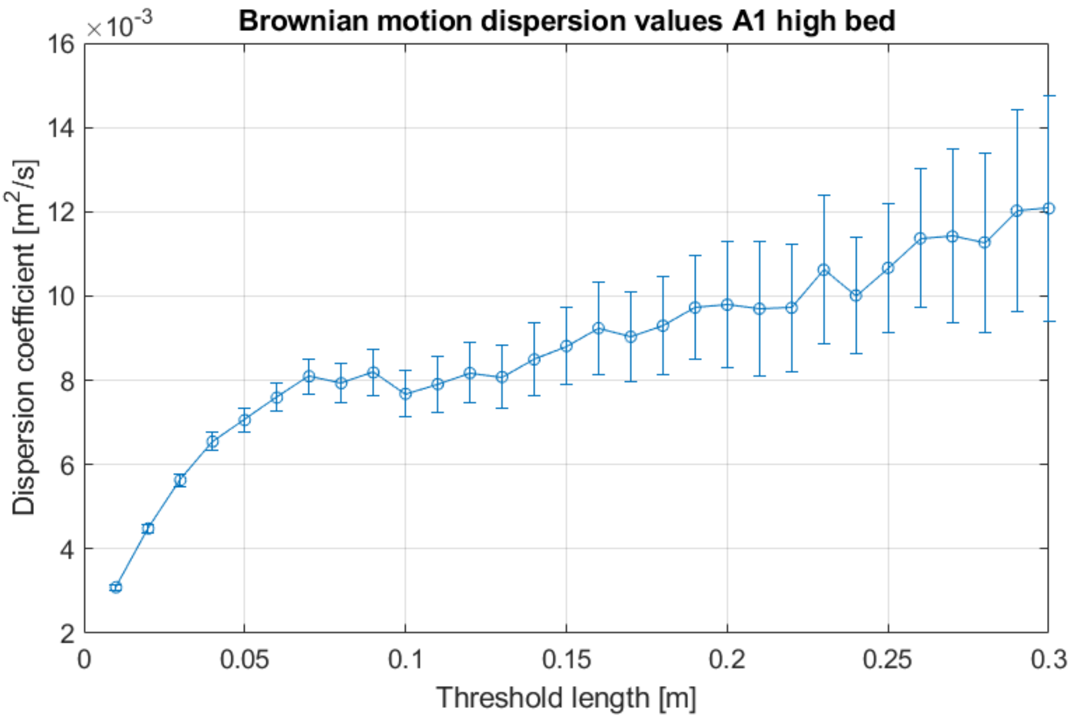

Figure E.1: Brownian motion dispersion values with 95% confidence intervals for A1 for the high bed.

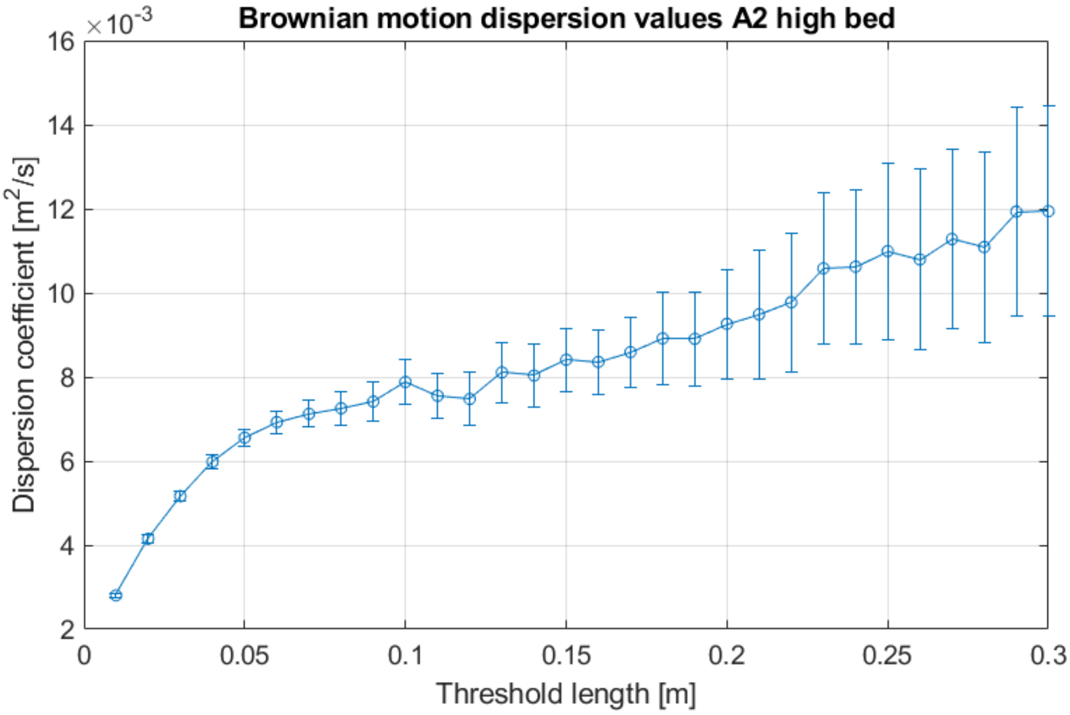

Figure E.2: Brownian motion dispersion values with 95% confidence intervals for A2 for the high bed.

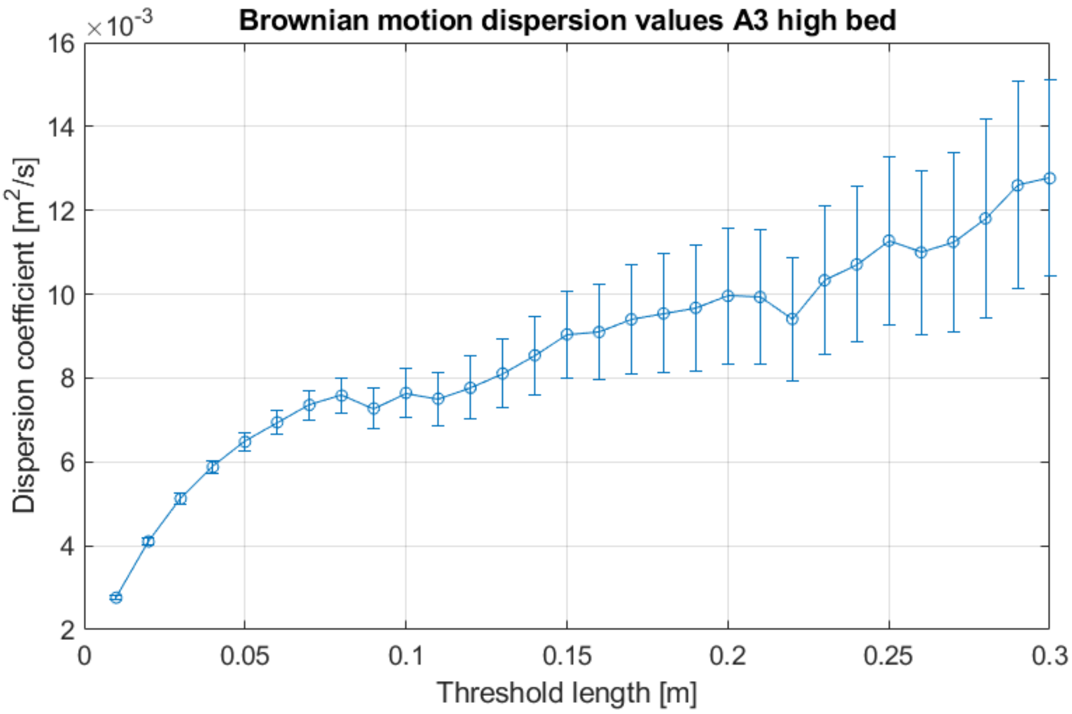

Figure E.3: Brownian motion dispersion values with 95% confidence intervals for A3 for the high bed.

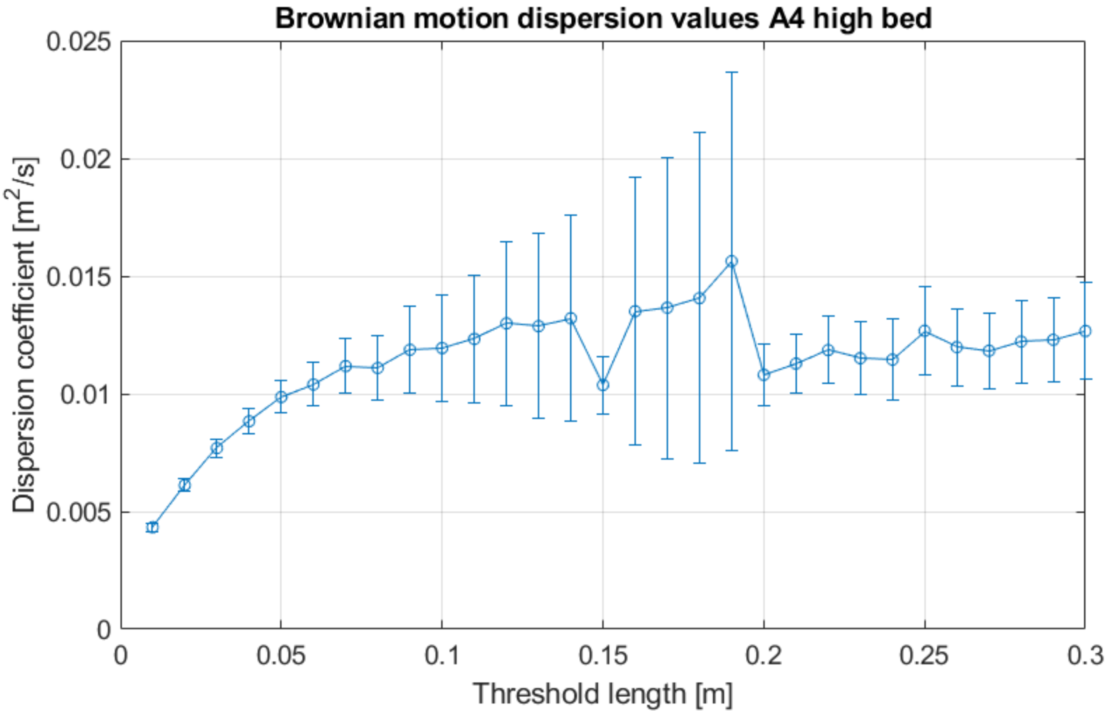

Figure E.4: Brownian motion dispersion values with 95% confidence intervals for A4 for the high bed.

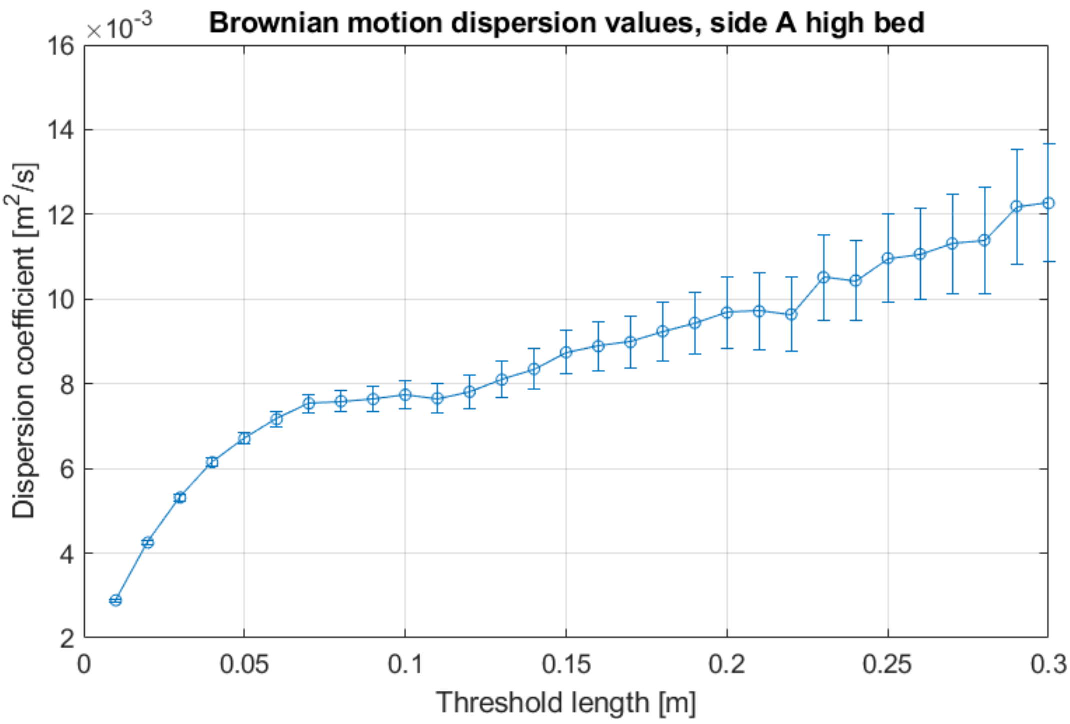

Figure E.5: Brownian motion dispersion values with 95% confidence intervals for all data on side A for the high bed.

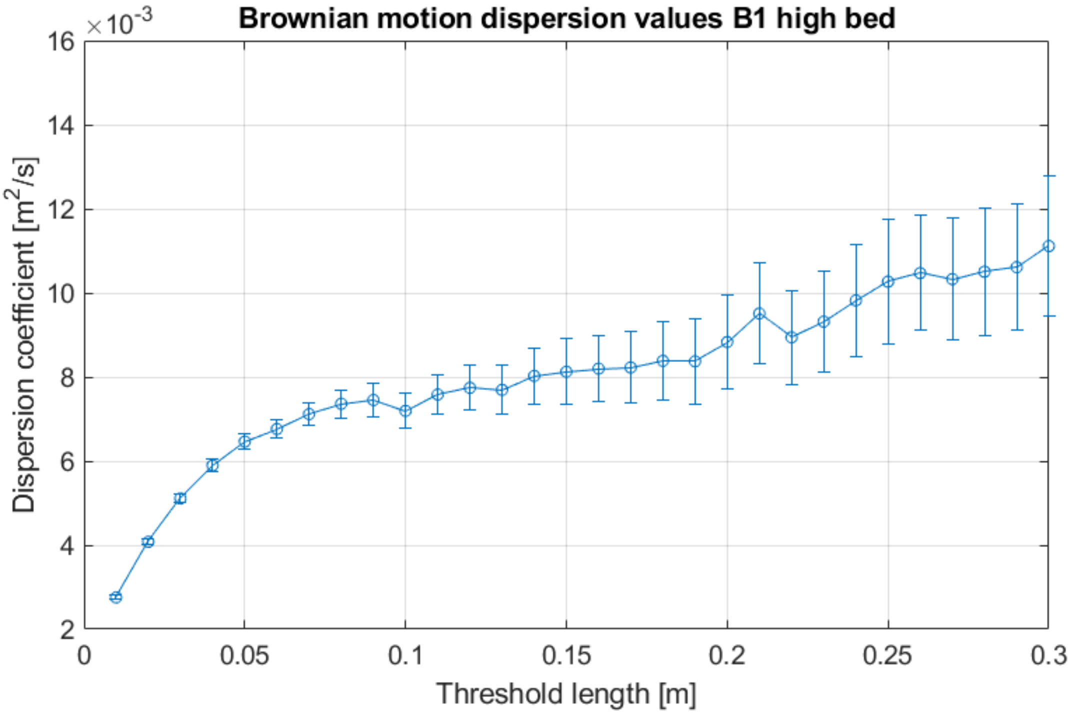

Figure E.6: Brownian motion dispersion values with 95% confidence intervals for B1 for the high bed.

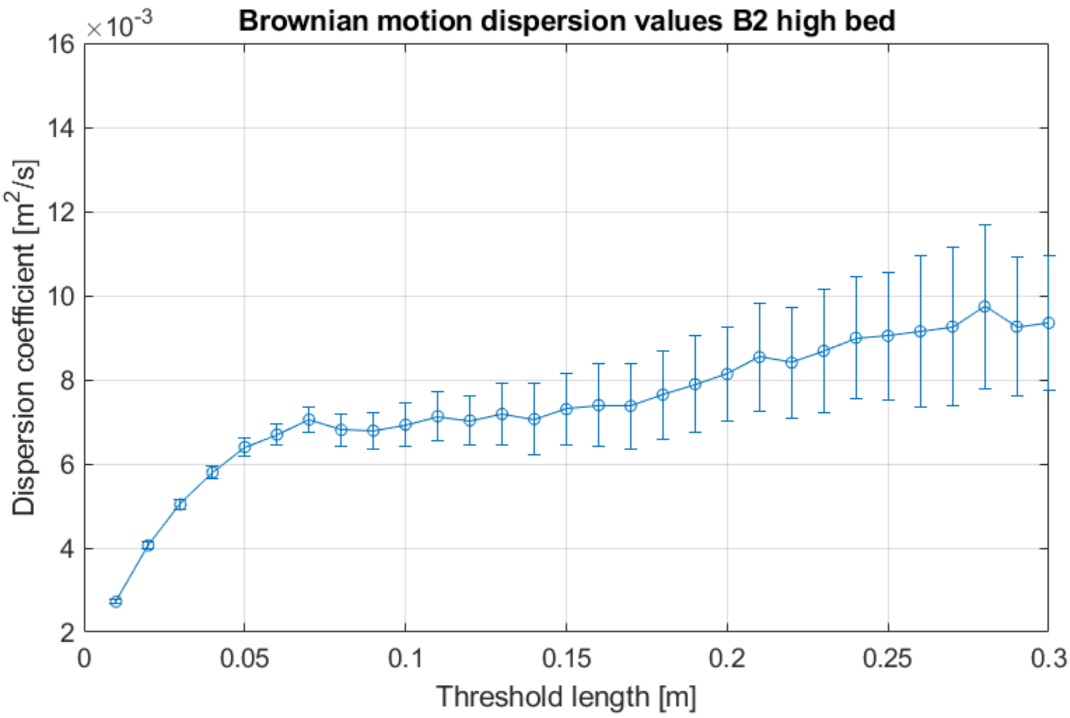

Figure E.7: Brownian motion dispersion values with 95% confidence intervals for B2 for the high bed.

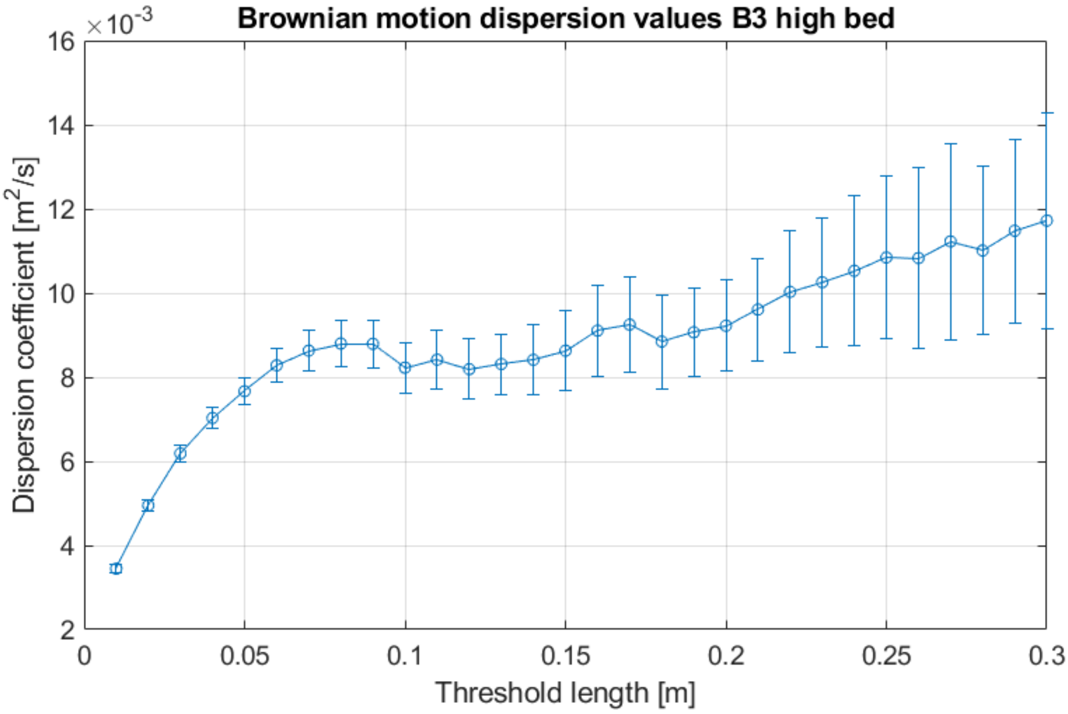

Figure E.8: Brownian motion dispersion values with 95% confidence intervals for B3 for the high bed.

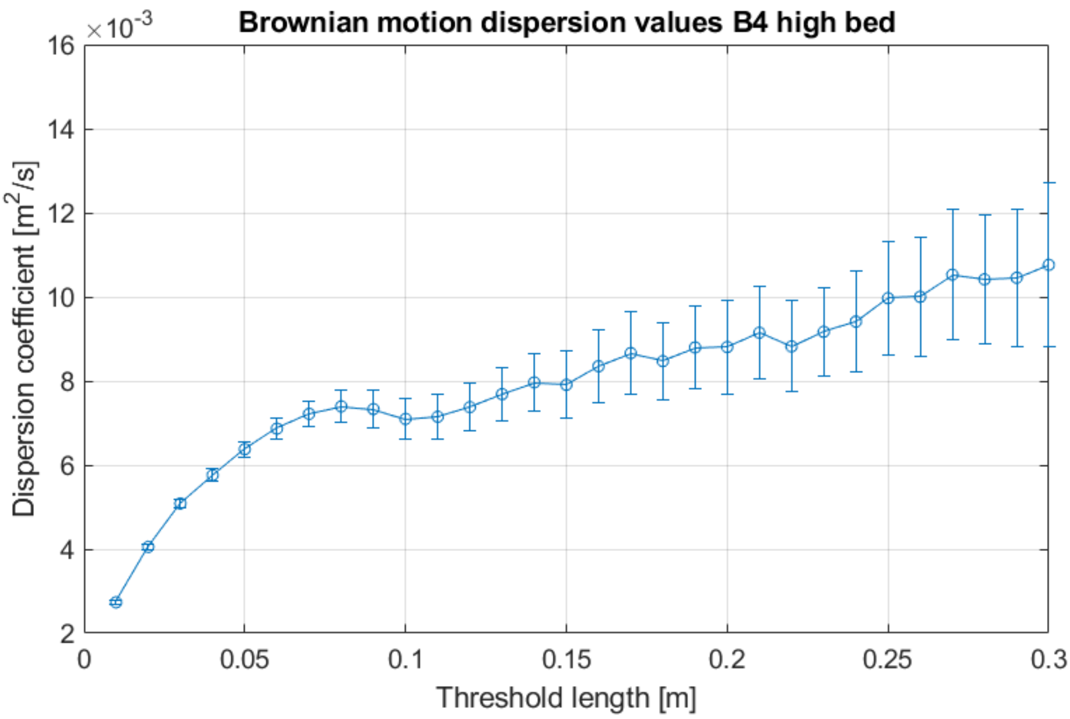

Figure E.9: Brownian motion dispersion values with 95% confidence intervals for B4 for the high bed.

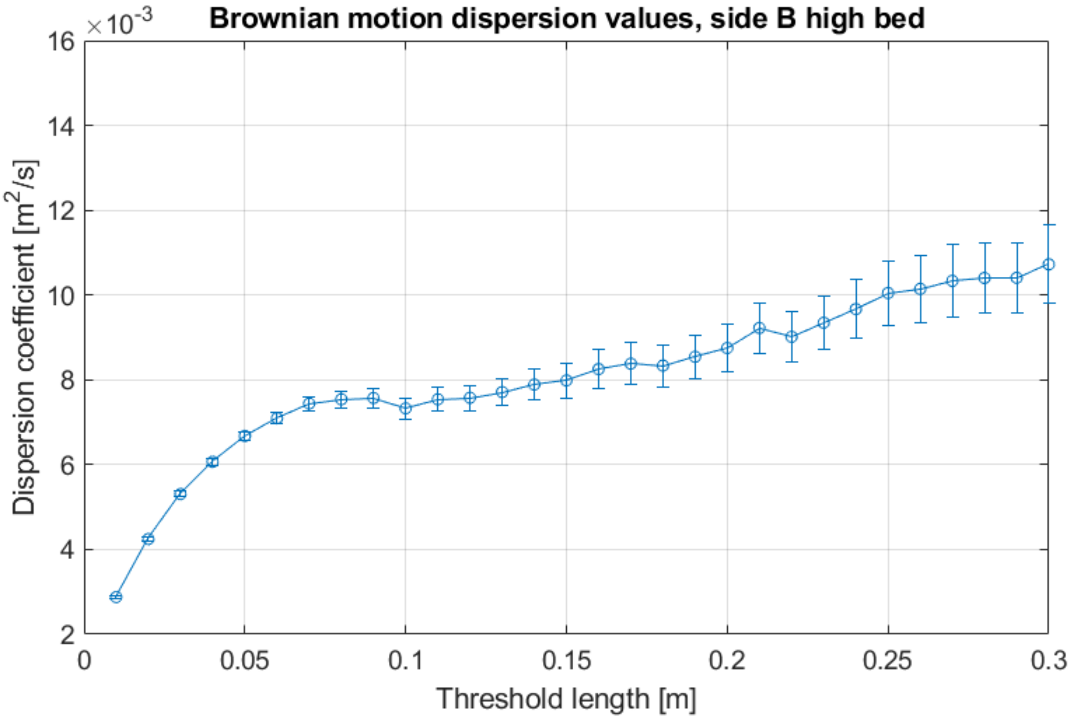

Figure E.10: Brownian motion dispersion values with 95% confidence intervals for all data on side B for the high bed.

F

Confidence intervals for mixing cell calculations for the high bed

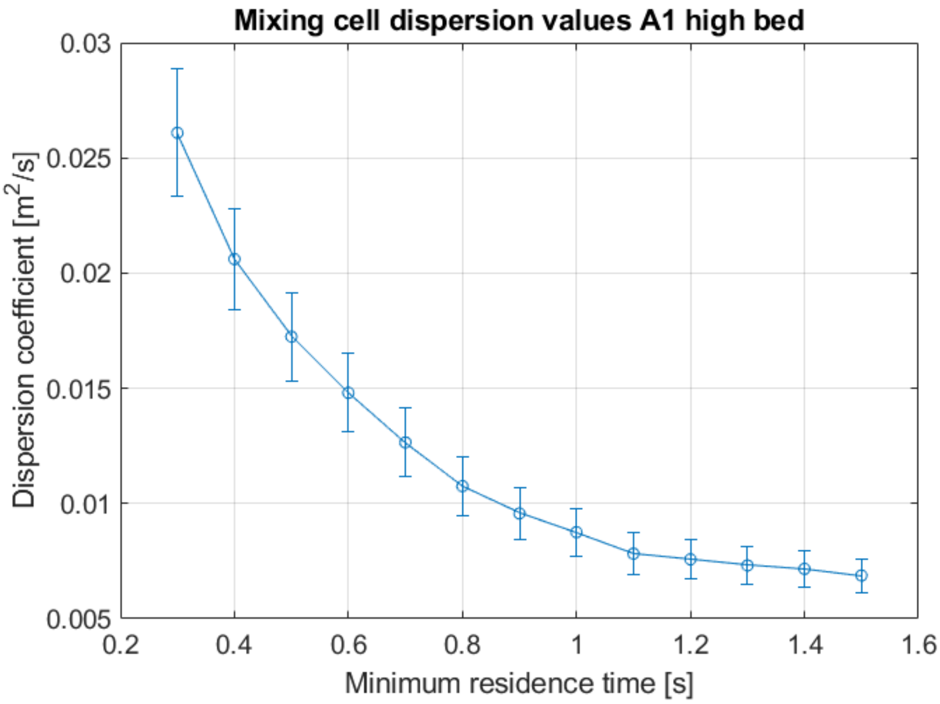

Figure F.1: Mixing cell dispersion values with 95% confidence intervals for A1 for the high bed.

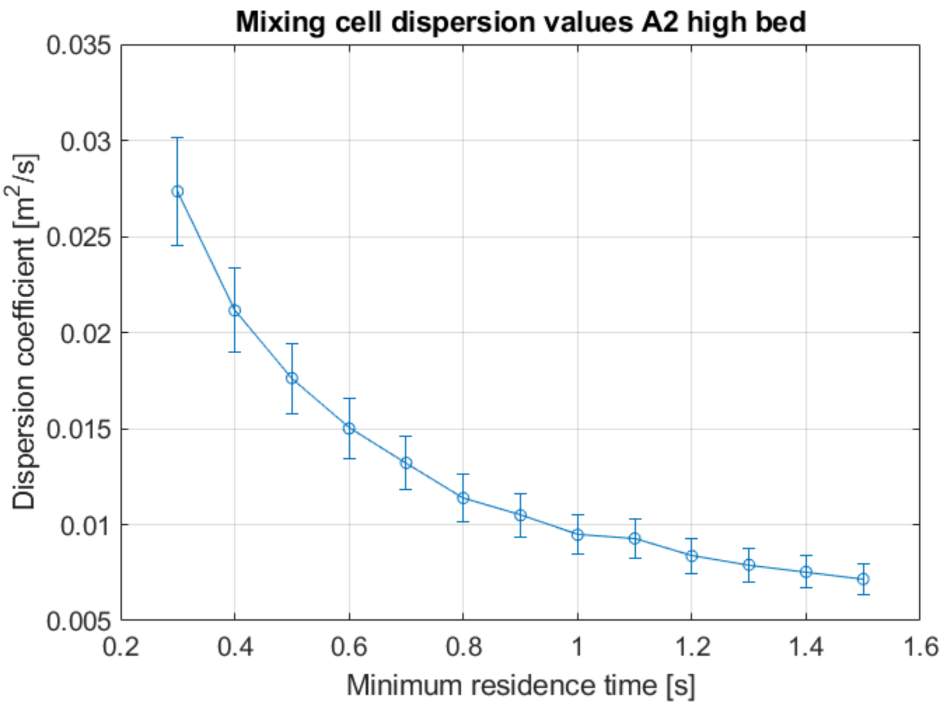

Figure F.2: Mixing cell dispersion values with 95% confidence intervals for A2 for the high bed.

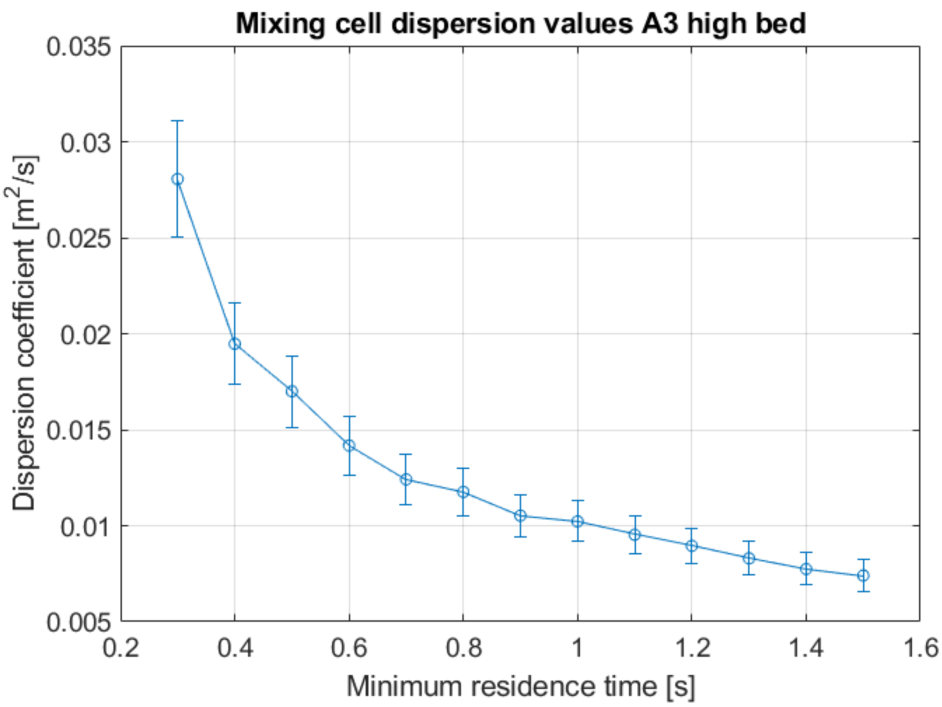

Figure F.3: Mixing cell dispersion values with 95% confidence intervals for A3 for the high bed.

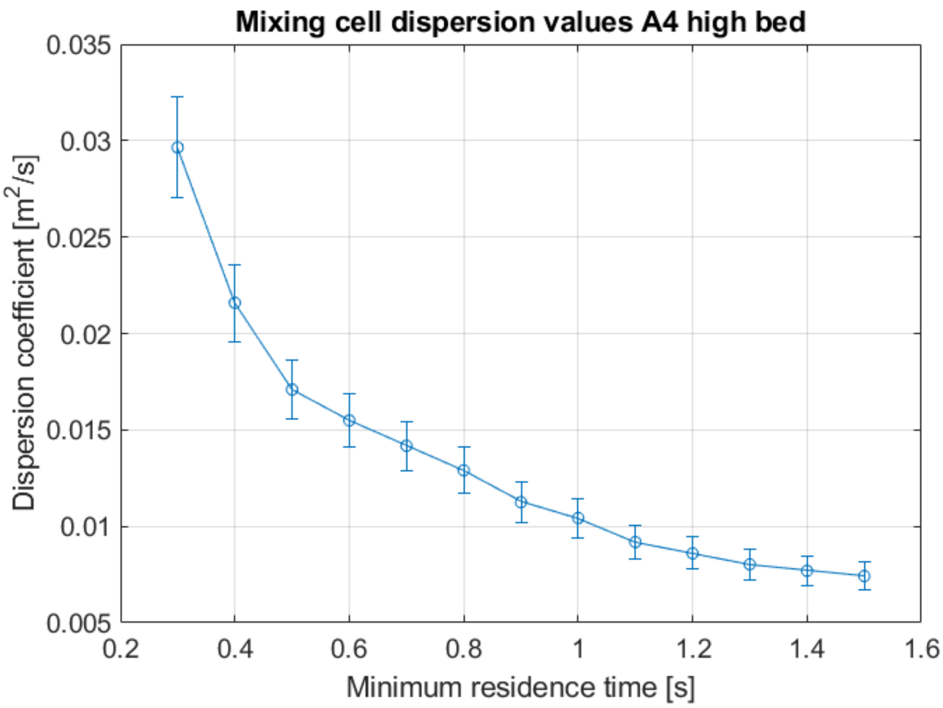

Figure F.4: Mixing cell dispersion values with 95% confidence intervals for A4 for the high bed.

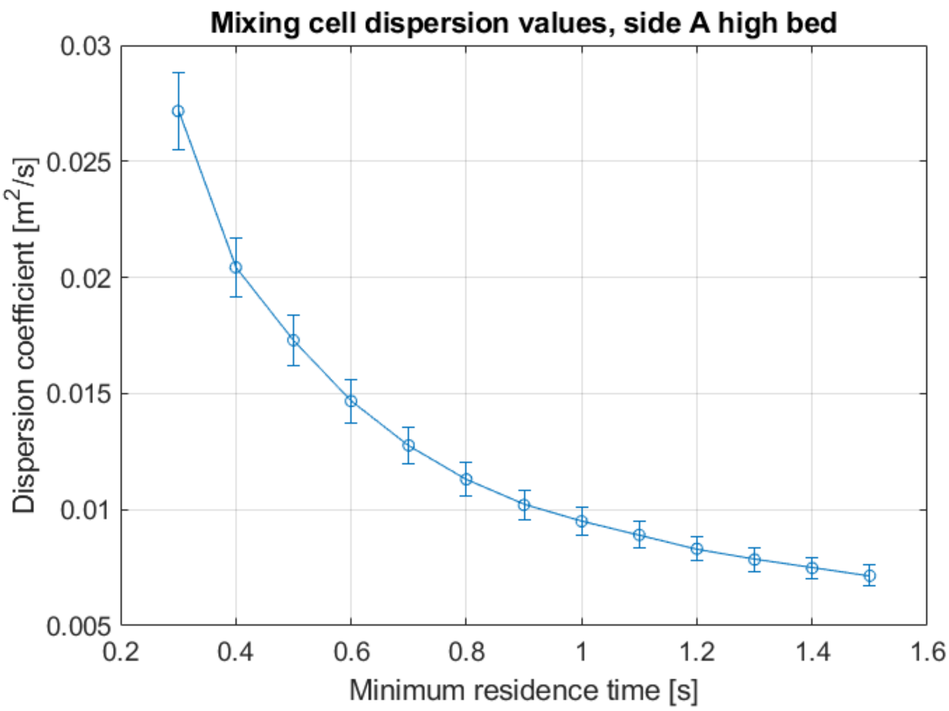

Figure F.5: Mixing cell dispersion values with 95% confidence intervals for all data on side A for the high bed.

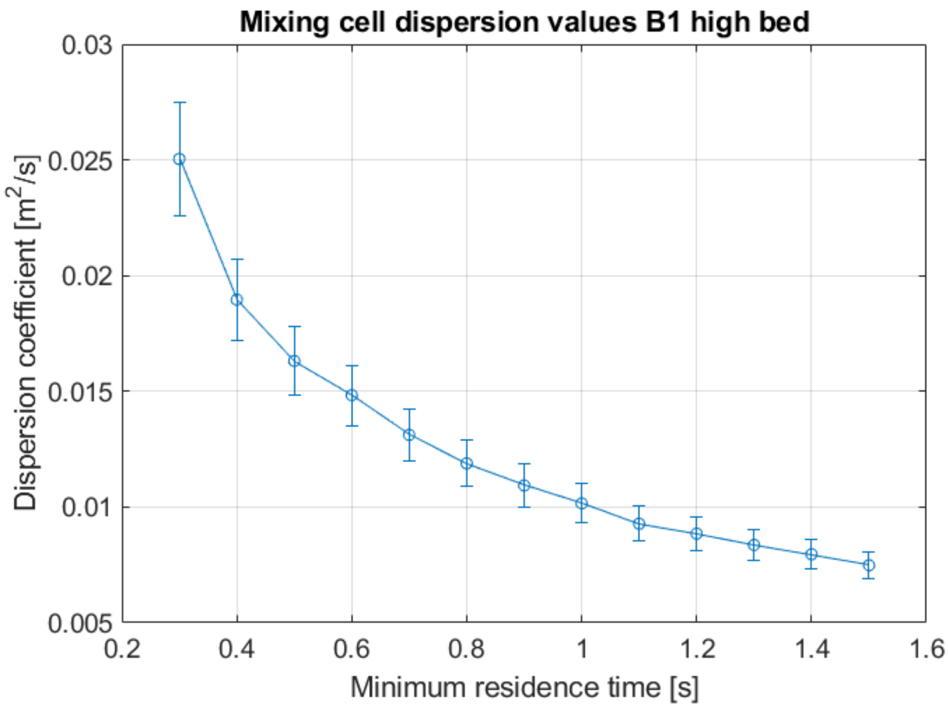

Figure F.6: Mixing cell dispersion values with 95% confidence intervals for B1 for the high bed.

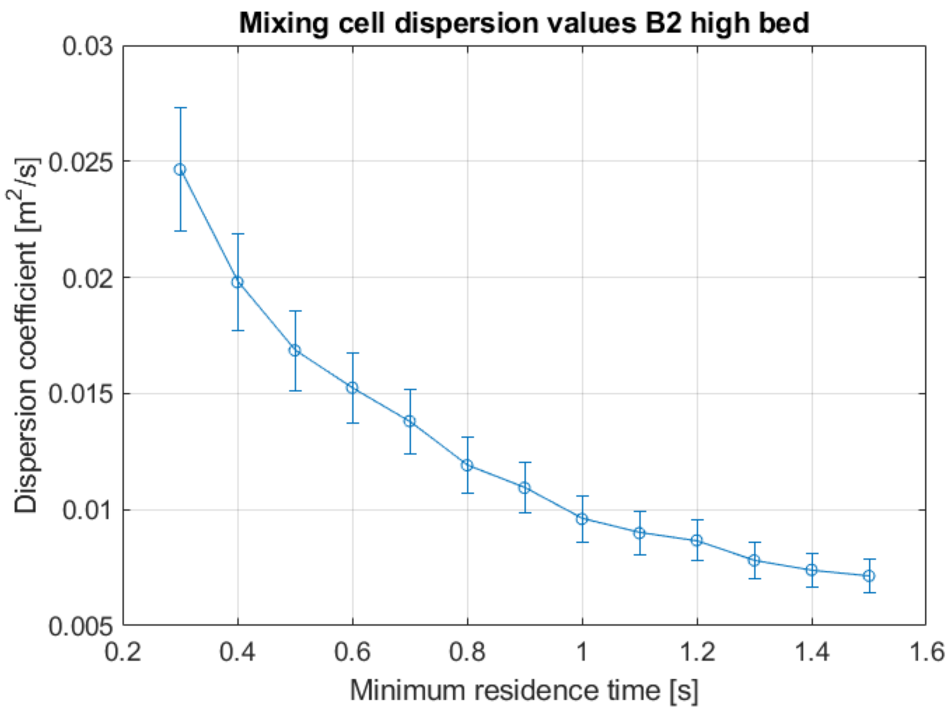

Figure F.7: Mixing cell dispersion values with 95% confidence intervals for B2 for the high bed.

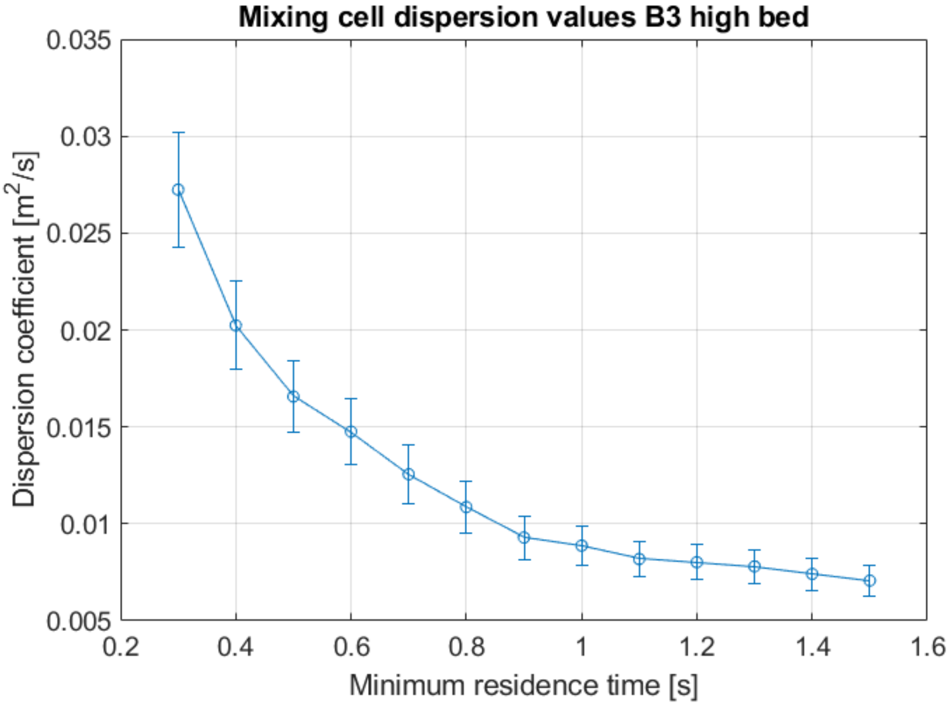

Figure F.8: Mixing cell dispersion values with 95% confidence intervals for B3 for the high bed.

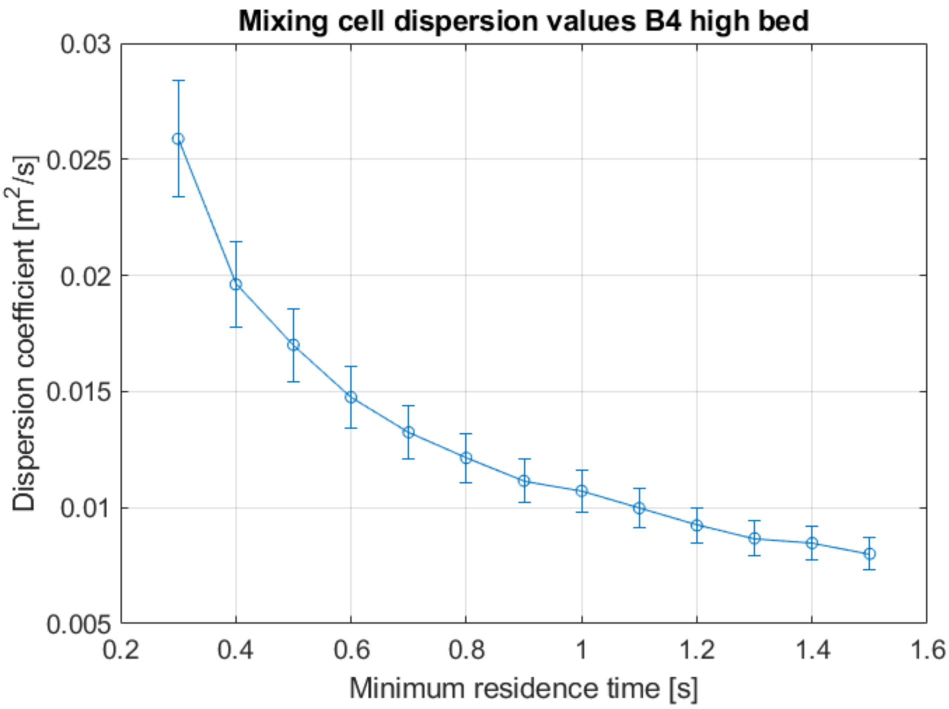

Figure F.9: Mixing cell dispersion values with 95% confidence intervals for B4 for the high bed.

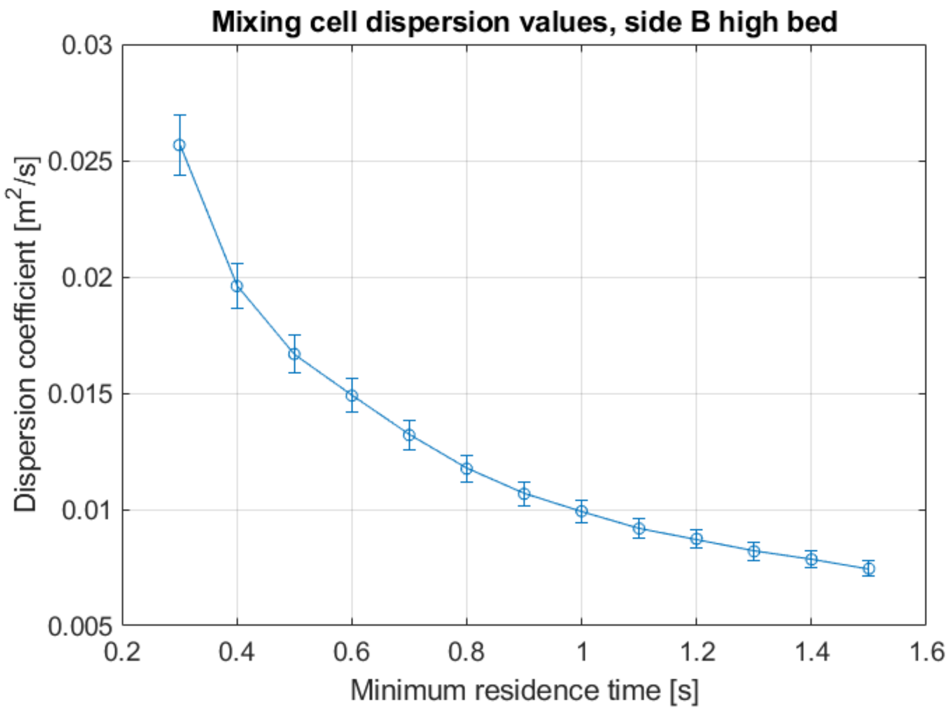

Figure F.10: Mixing cell dispersion values with 95% confidence intervals for all data on side B for the high bed.

G

Confidence intervals for Brownian motion calculations at medium bed height

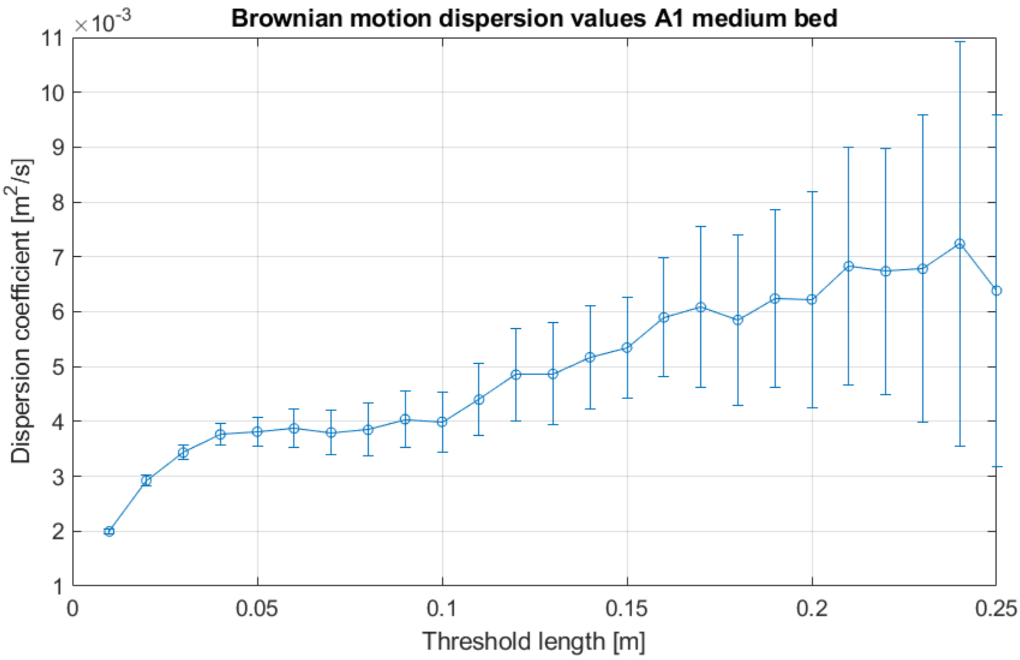

Figure G.1: Brownian motion dispersion values with 95% confidence intervals for A1 at medium bed height.

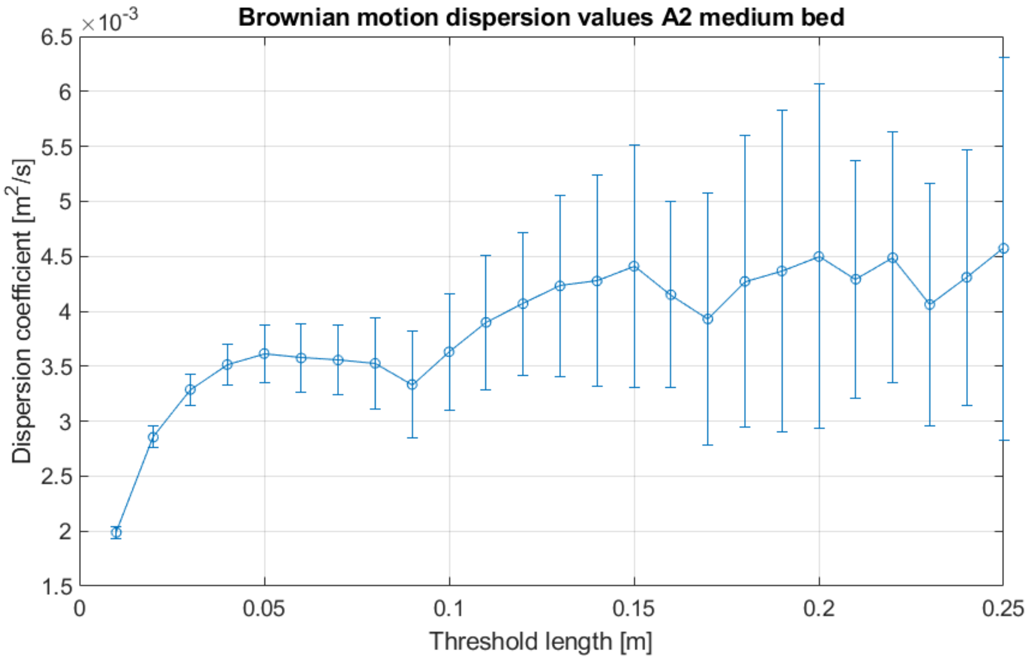

Figure G.2: Brownian motion dispersion values with 95% confidence intervals for A2 at medium bed height.

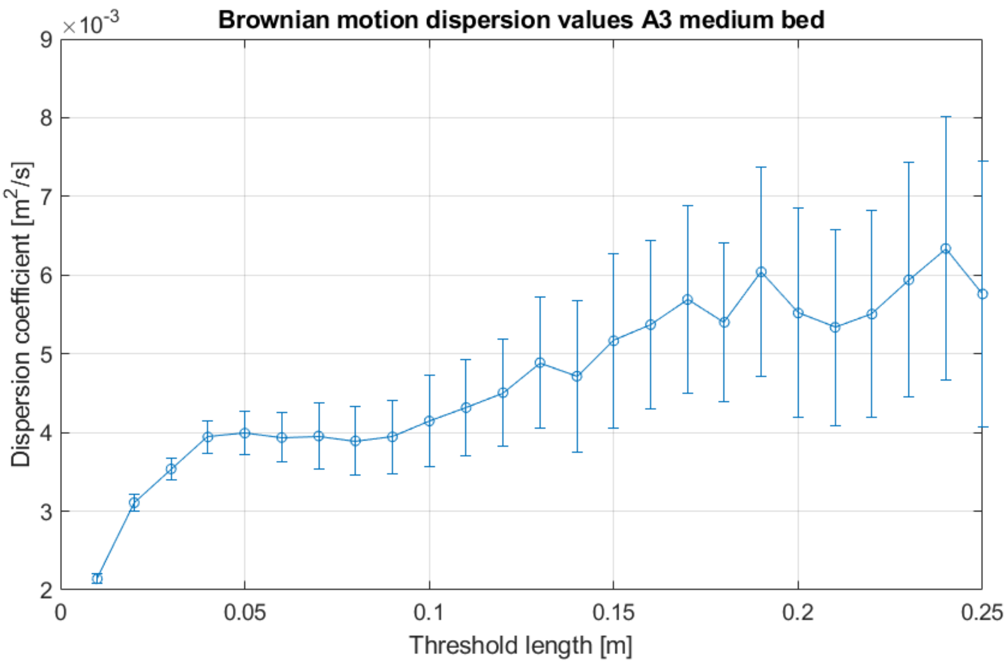

Figure G.3: Brownian motion dispersion values with 95% confidence intervals for A3 at medium bed height.

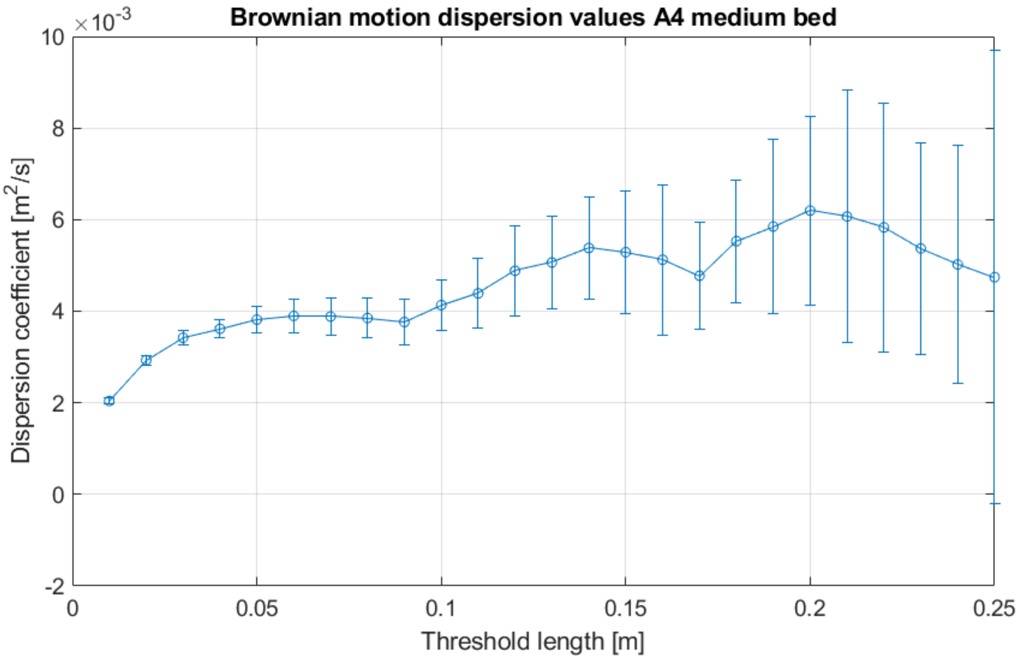

Figure G.4: Brownian motion dispersion values with 95% confidence intervals for A4 at medium bed height.

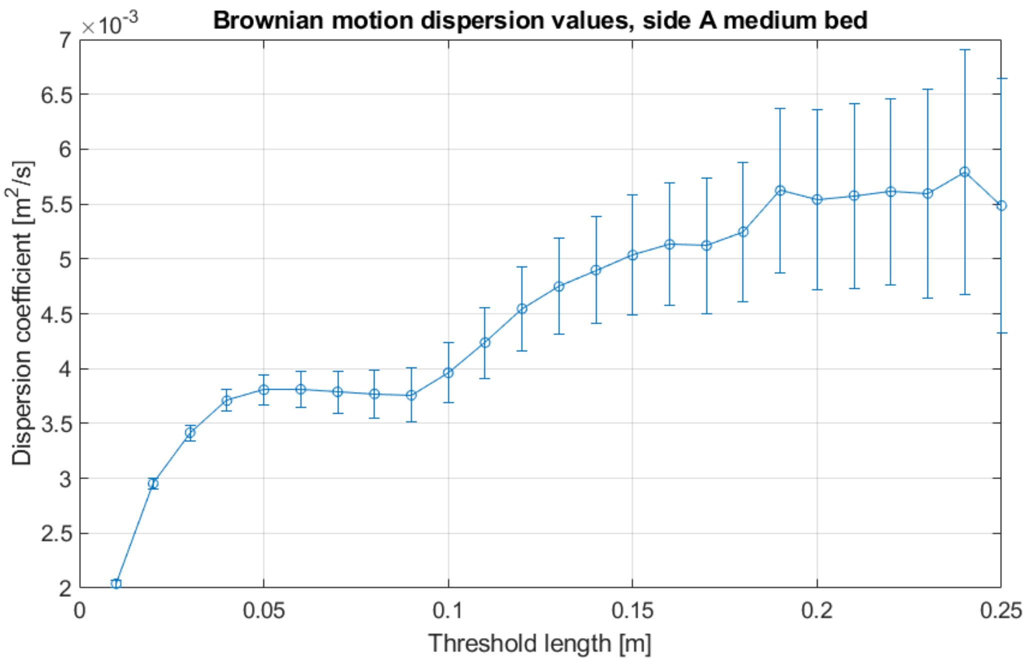

Figure G.5: Brownian motion dispersion values with 95% confidence intervals for all data on side A at medium bed height.

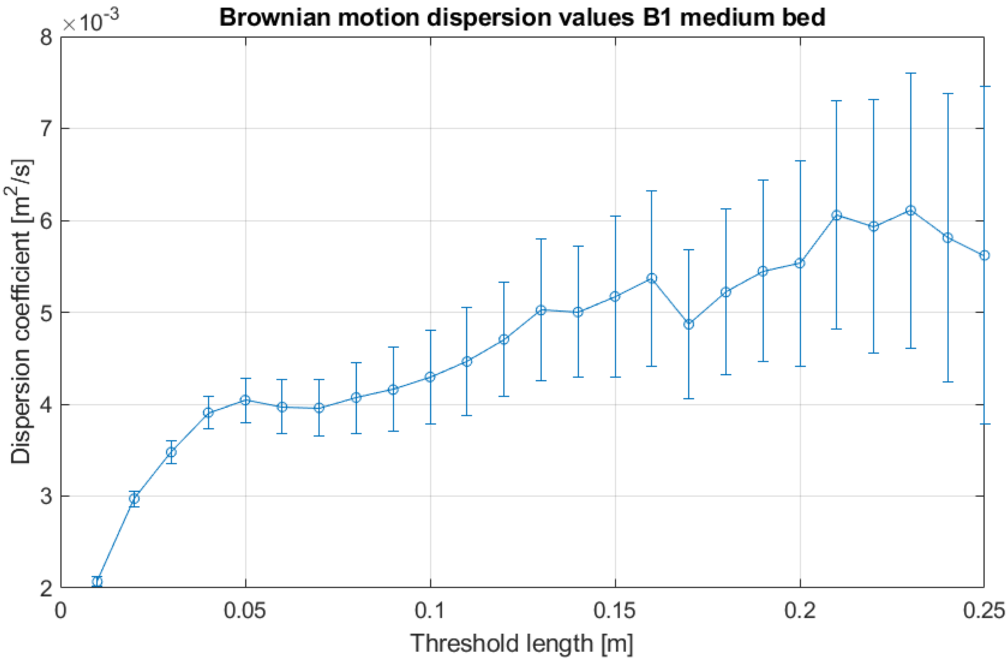

Figure G.6: Brownian motion dispersion values with 95% confidence intervals for B1 at medium bed height.

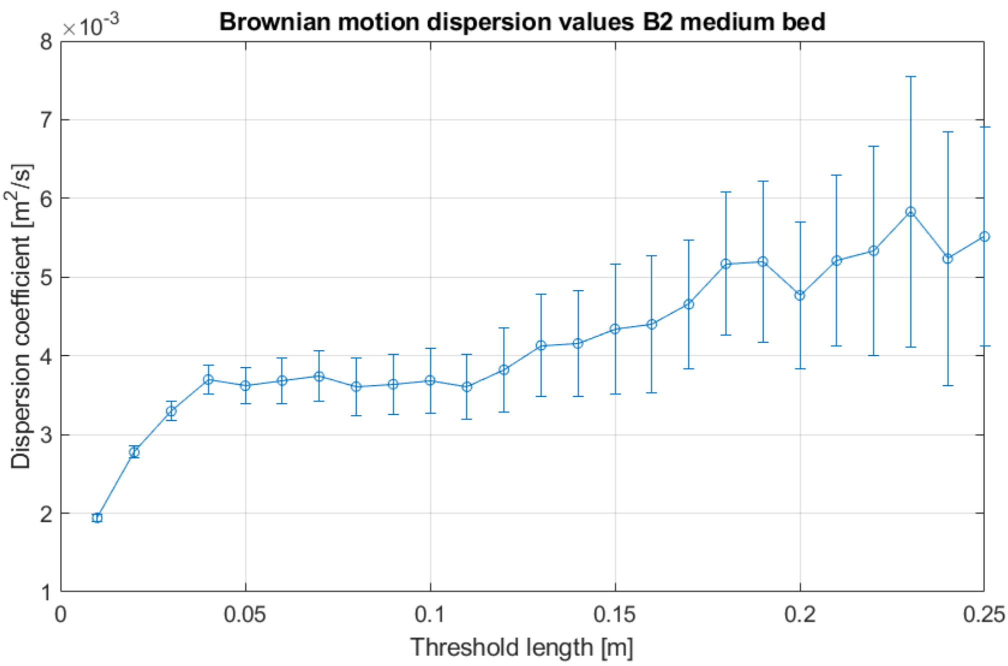

Figure G.7: Brownian motion dispersion values with 95% confidence intervals for B2 at medium bed height.

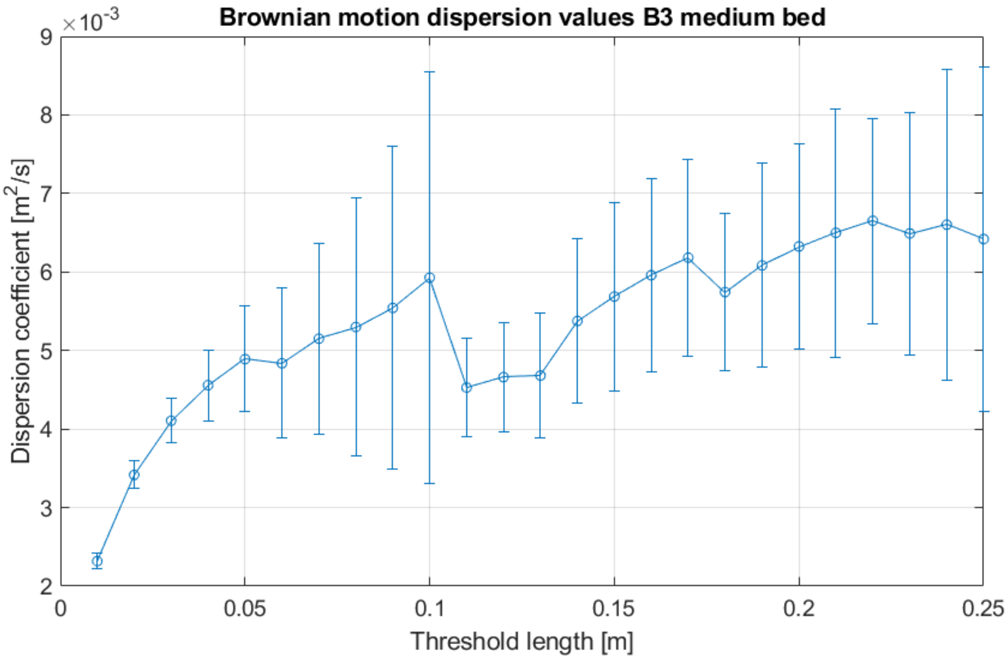

Figure G.8: Brownian motion dispersion values with 95% confidence intervals for B3 at medium bed height.

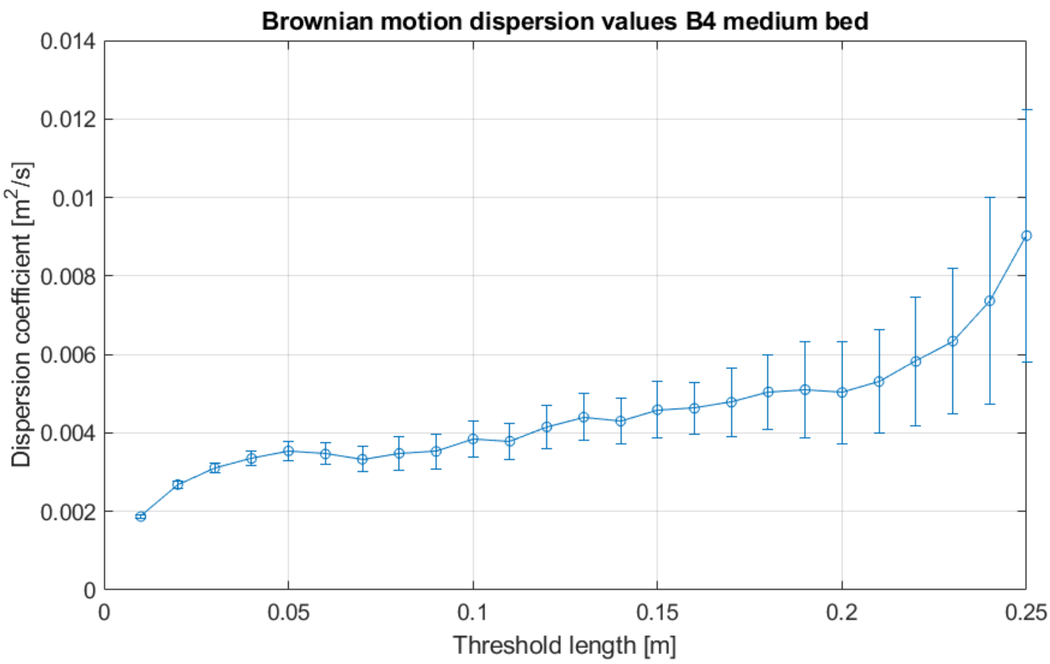

Figure G.9: Brownian motion dispersion values with 95% confidence intervals for B4 at medium bed height.

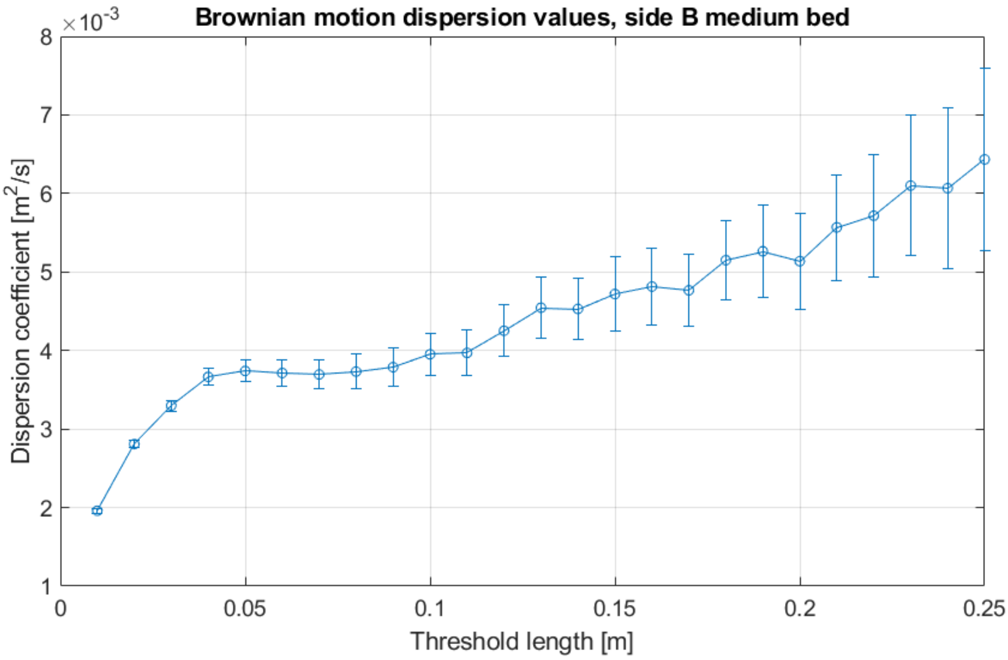

Figure G.10: Brownian motion dispersion values with 95% confidence intervals for all data on side B at medium bed height.

H

Confidence intervals for mixing cell calculations for at medium bed height

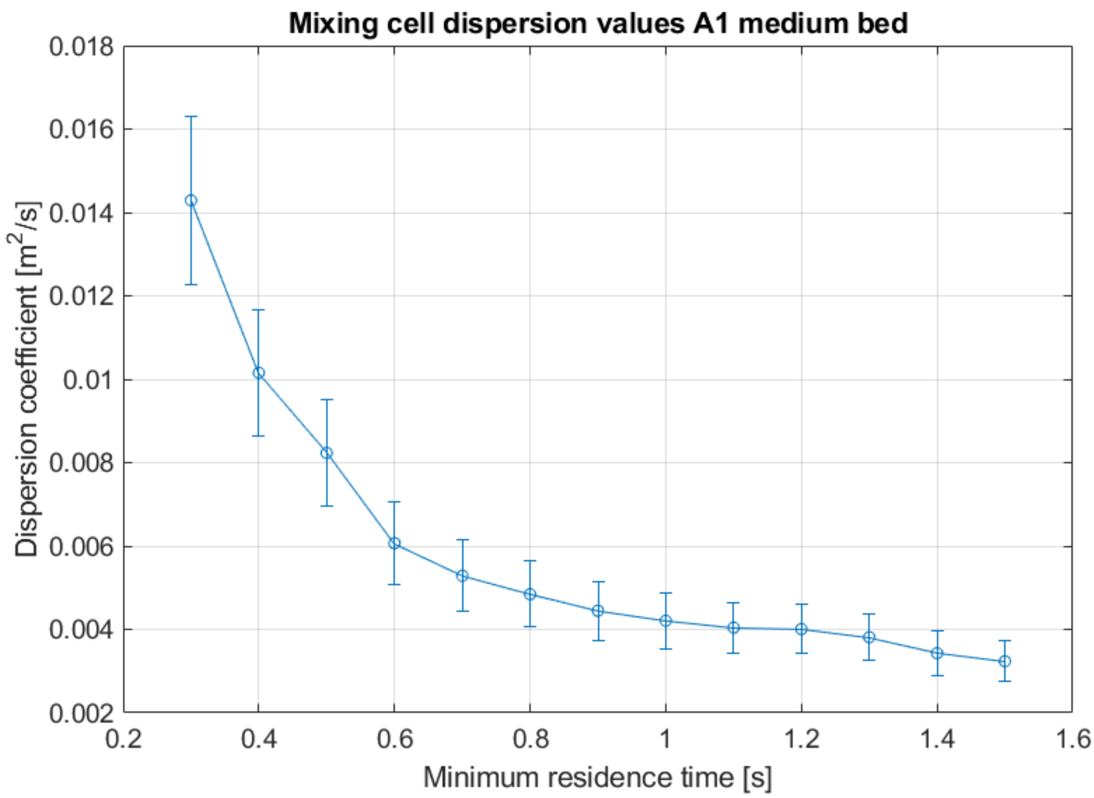

Figure H.1: Mixing cell dispersion values with 95% confidence intervals for A1 at medium bed height.

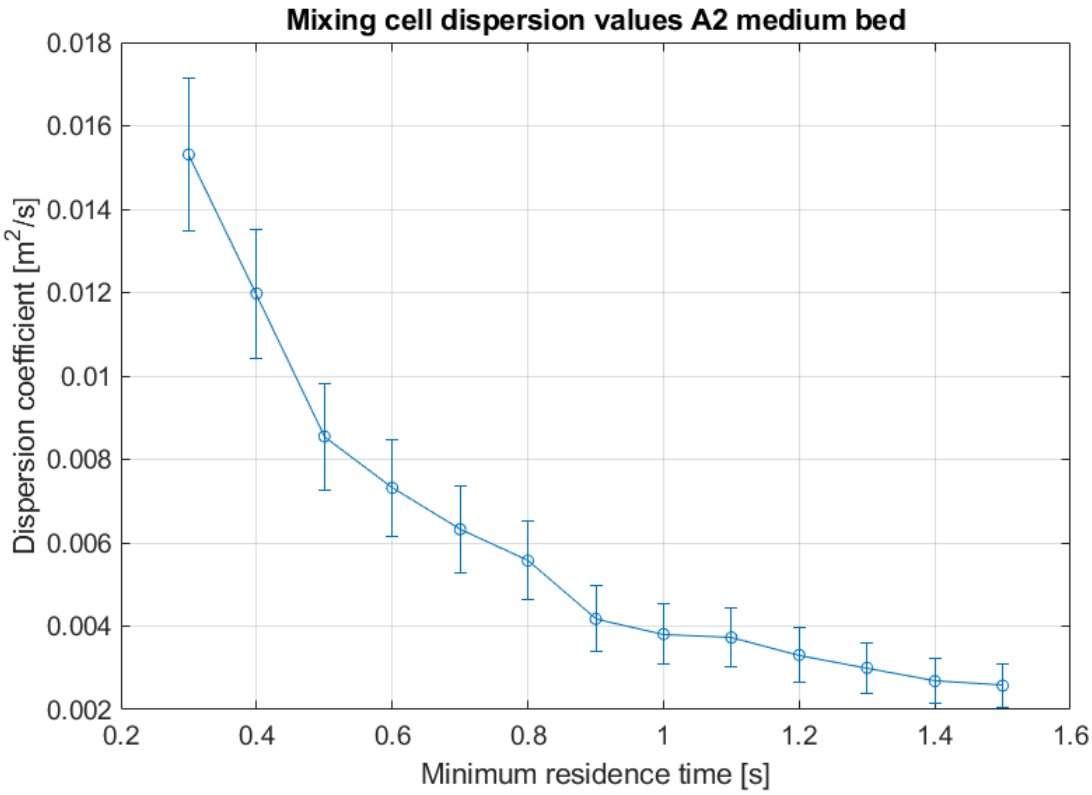

Figure H.2: Mixing cell dispersion values with 95% confidence intervals for A2 at medium bed height.

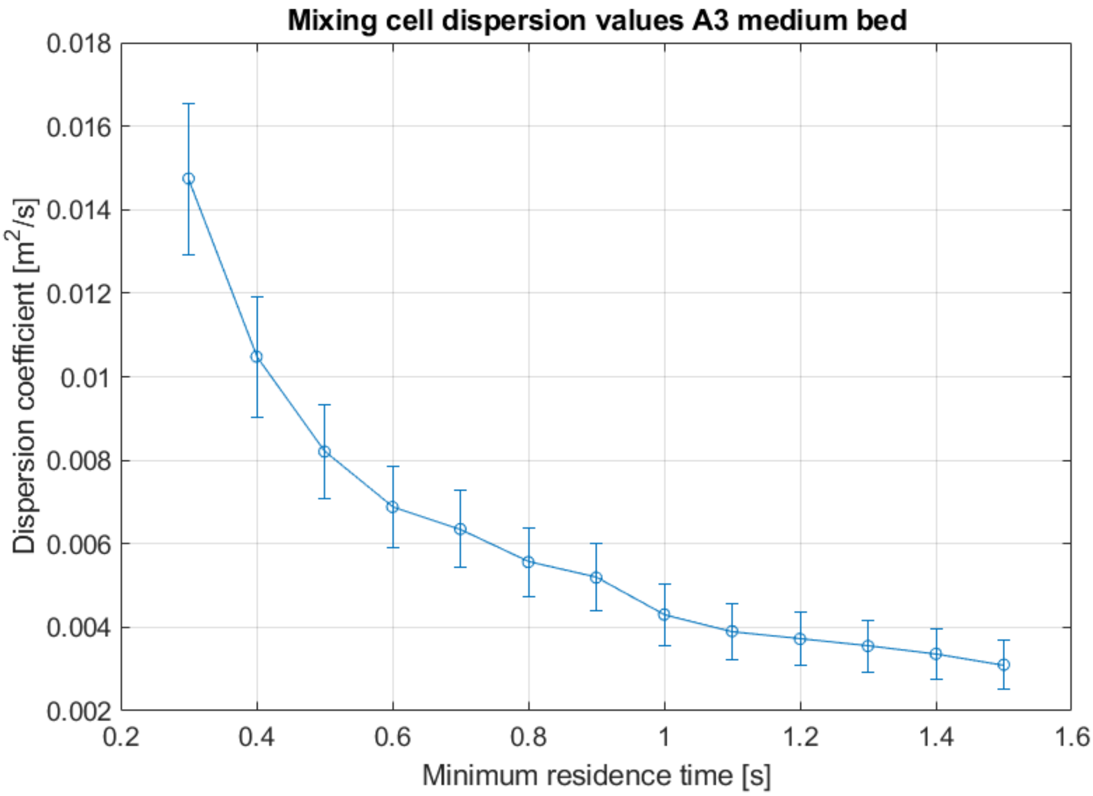

Figure H.3: Mixing cell dispersion values with 95% confidence intervals for A3 at medium bed height.

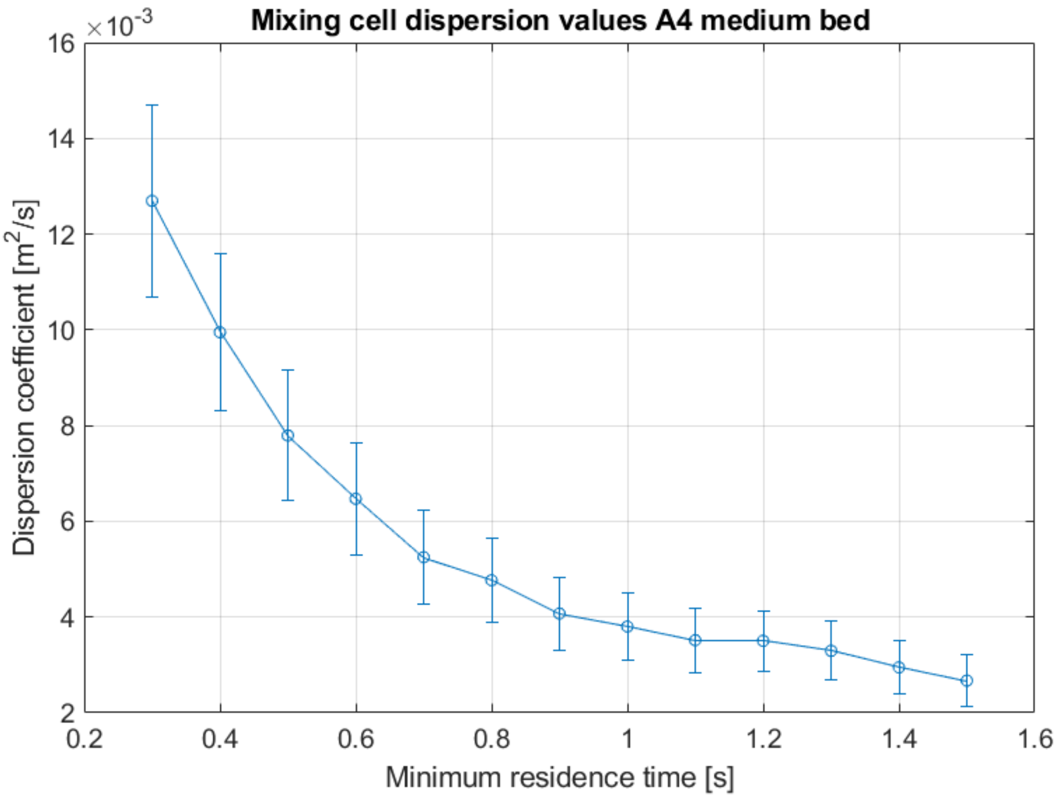

Figure H.4: Mixing cell dispersion values with 95% confidence intervals for A4 at medium bed height.

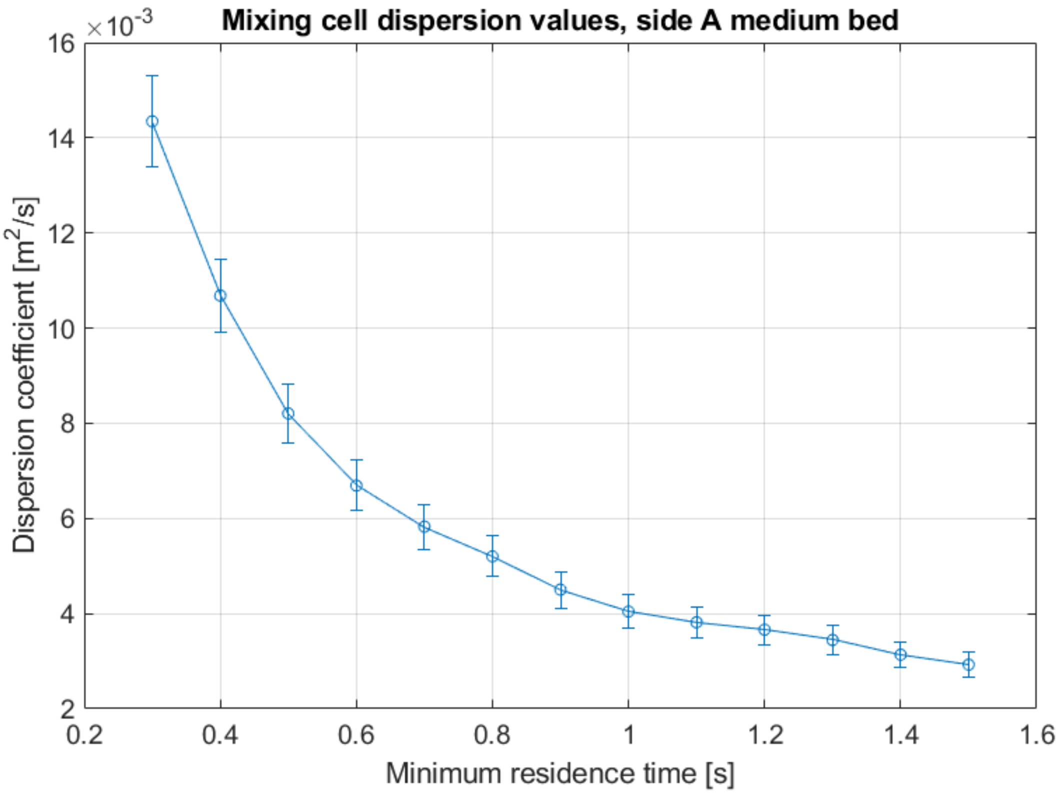

Figure H.5: Mixing cell dispersion values with 95% confidence intervals for all data on side A at medium bed high.

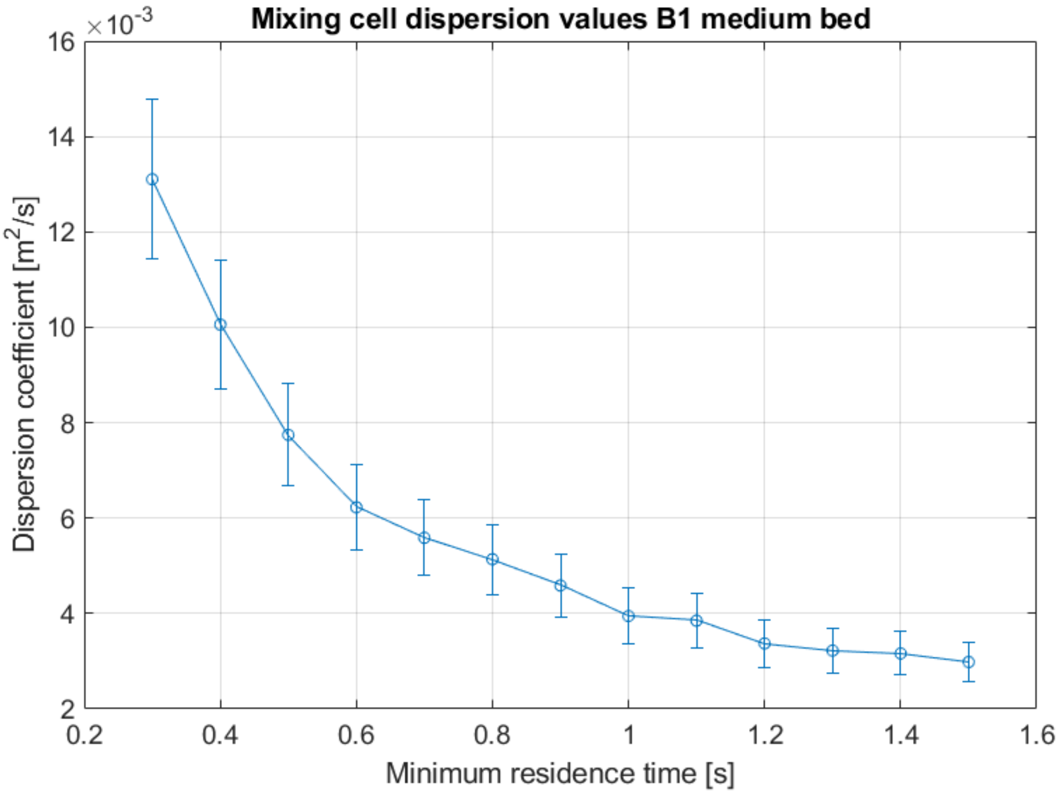

Figure H.6: Mixing cell dispersion values with 95% confidence intervals for B1 at medium bed height.

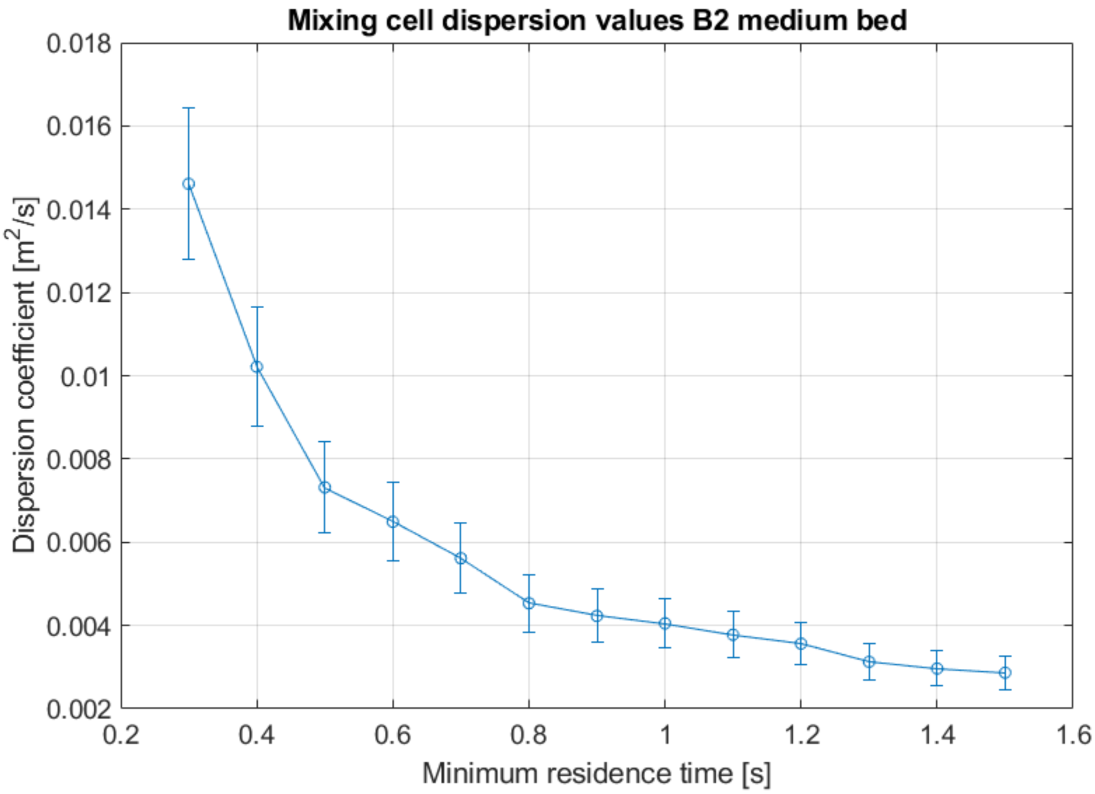

Figure H.7: Mixing cell dispersion values with 95% confidence intervals for B2 at medium bed height.

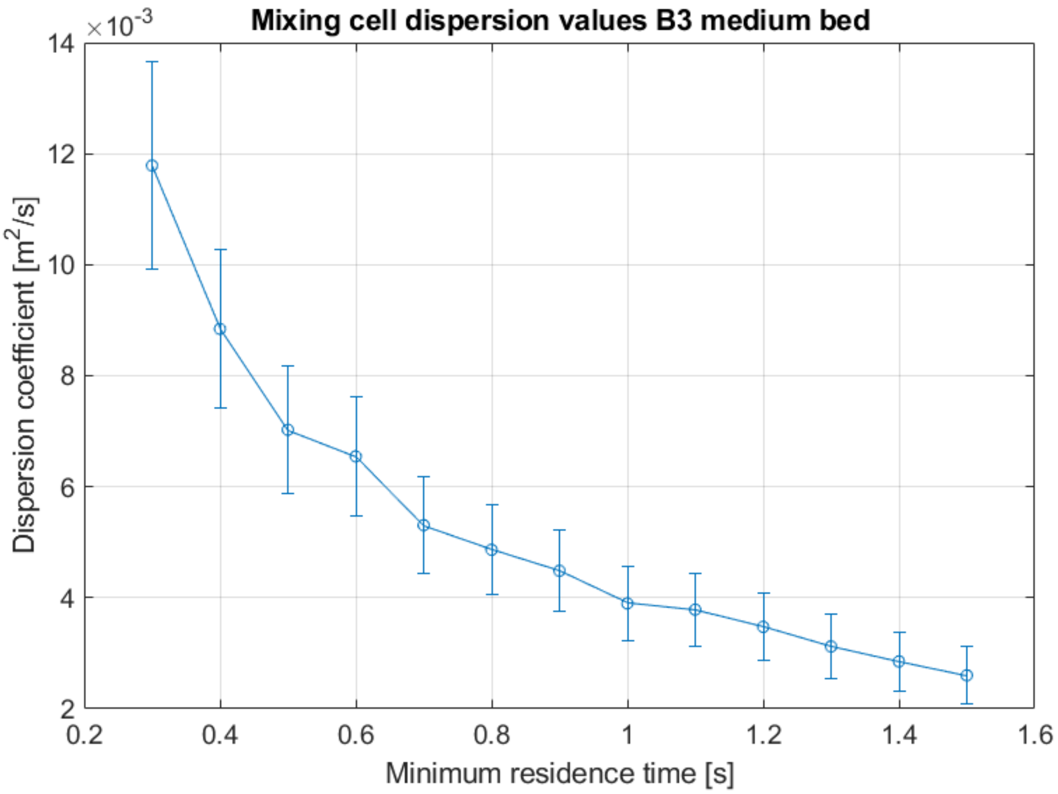

Figure H.8: Mixing cell dispersion values with 95% confidence intervals for B3 at medium bed height.

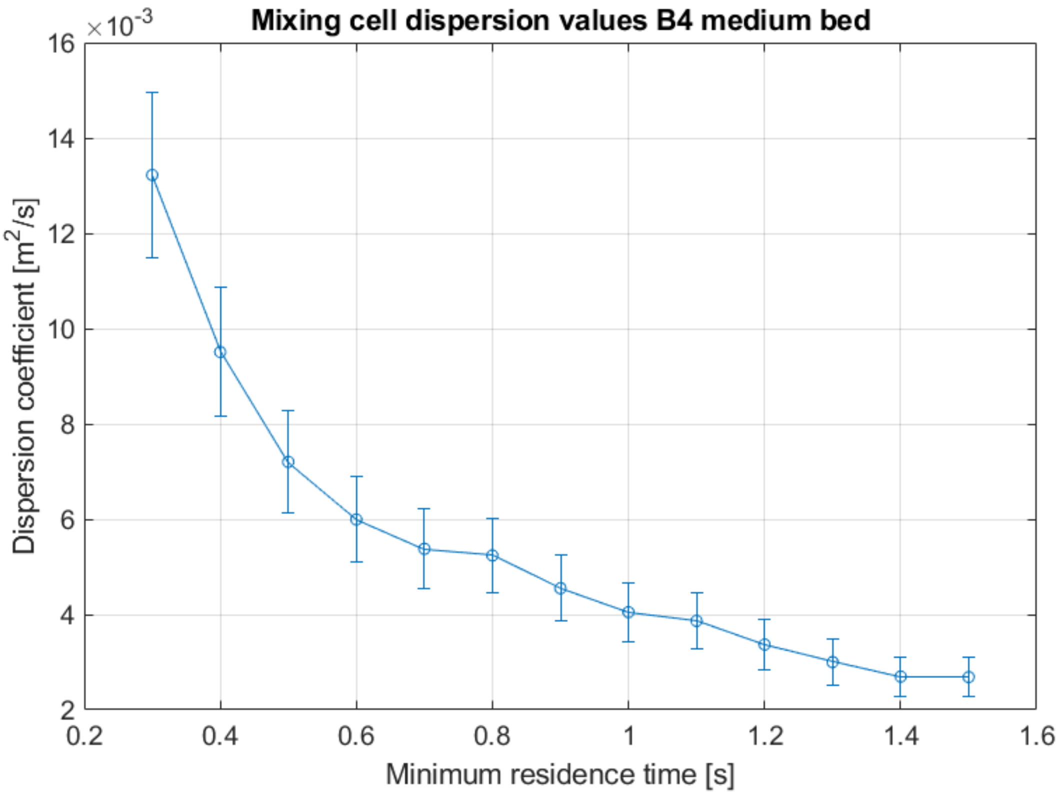

Figure H.9: Mixing cell dispersion values with 95% confidence intervals for B4 at medium bed height.

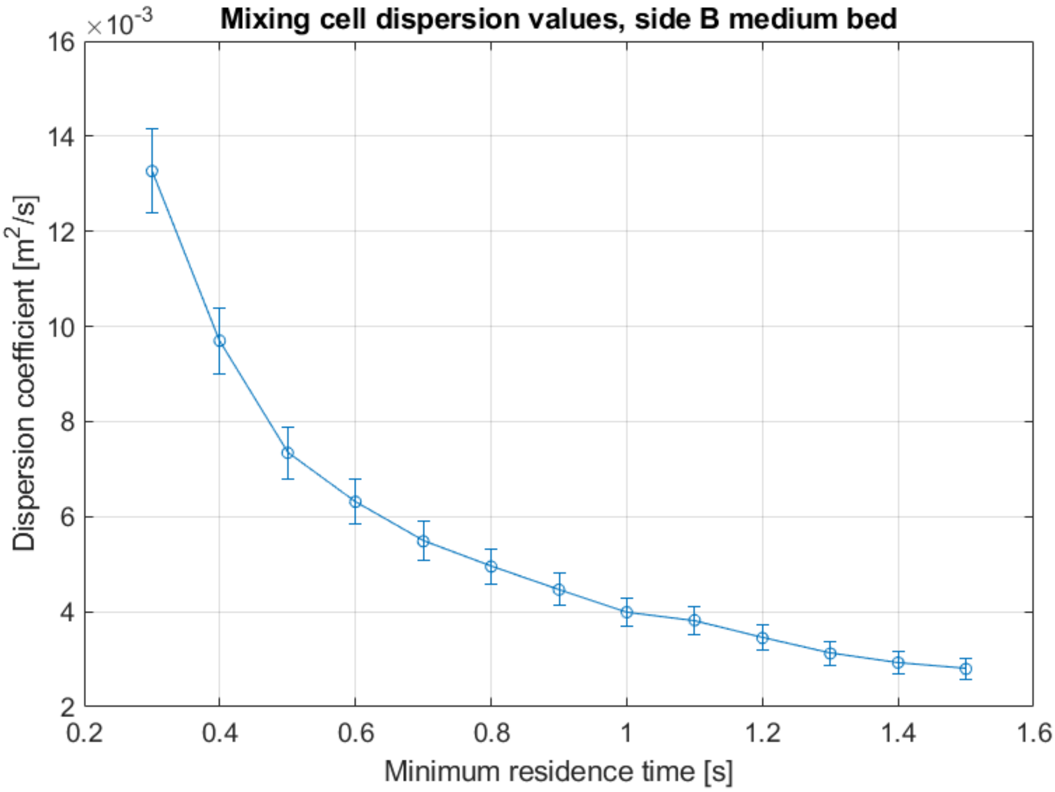

Figure H.10: Mixing cell dispersion values with 95% confidence intervals for all data on side B at medium bed height.

I

Confidence intervals for Brownian motion calculations for the low bed

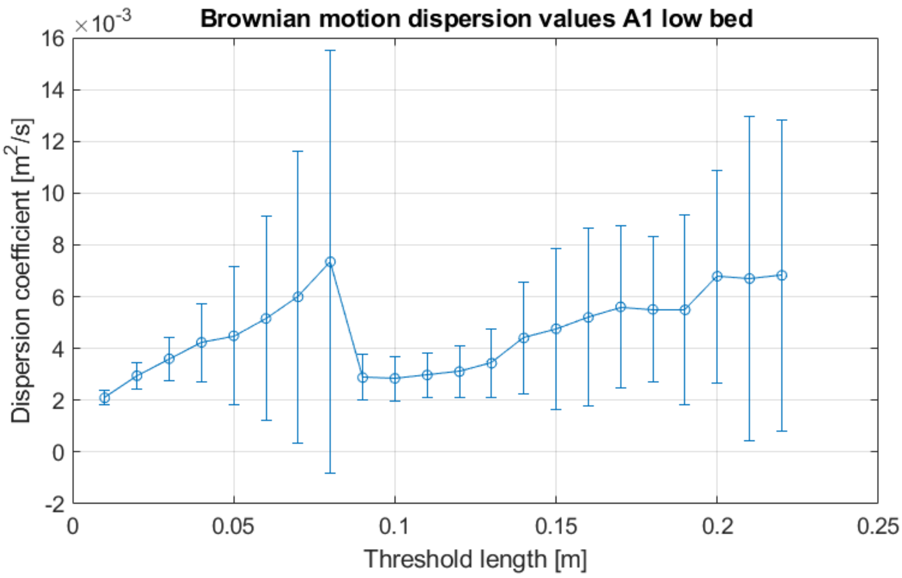

Figure I.1: Brownian motion dispersion values with 95% confidence intervals for A1 at low bed height.

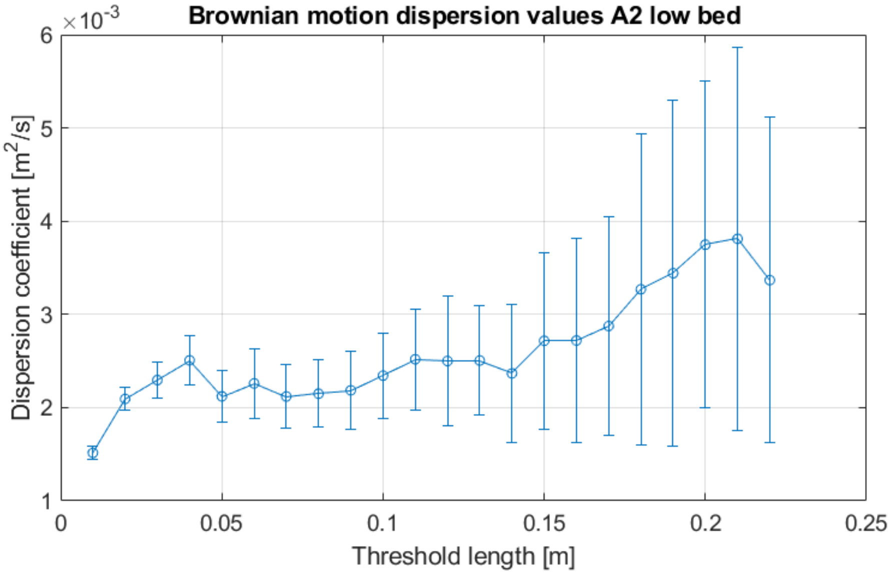

Figure I.2: Brownian motion dispersion values with 95% confidence intervals for A2 at low bed height.

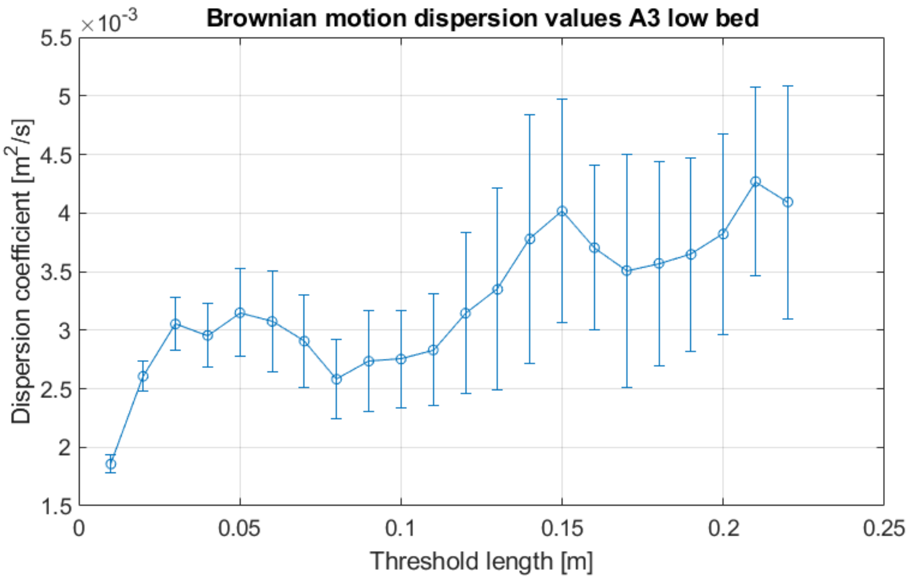

Figure I.3: Brownian motion dispersion values with 95% confidence intervals for A3 at low bed height.

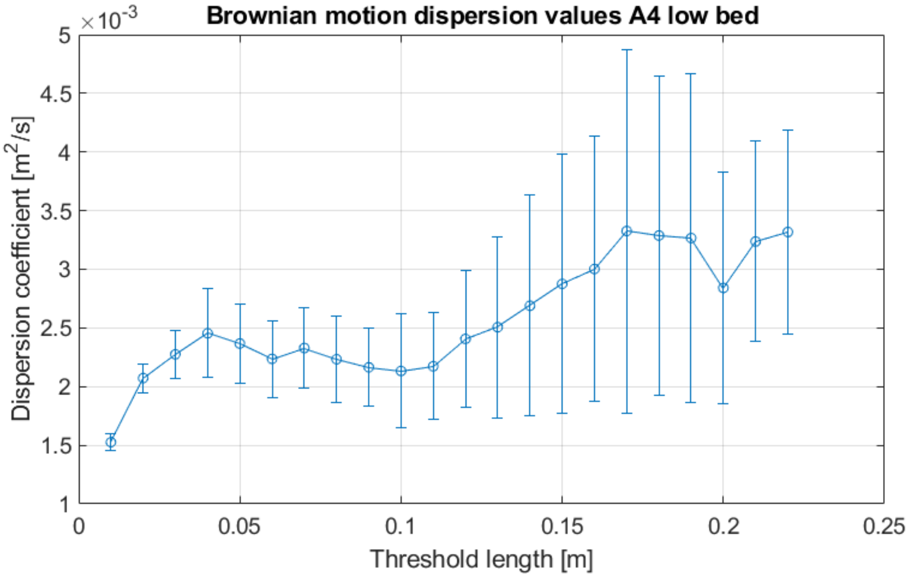

Figure I.4: Brownian motion dispersion values with 95% confidence intervals for A4 at low bed height.

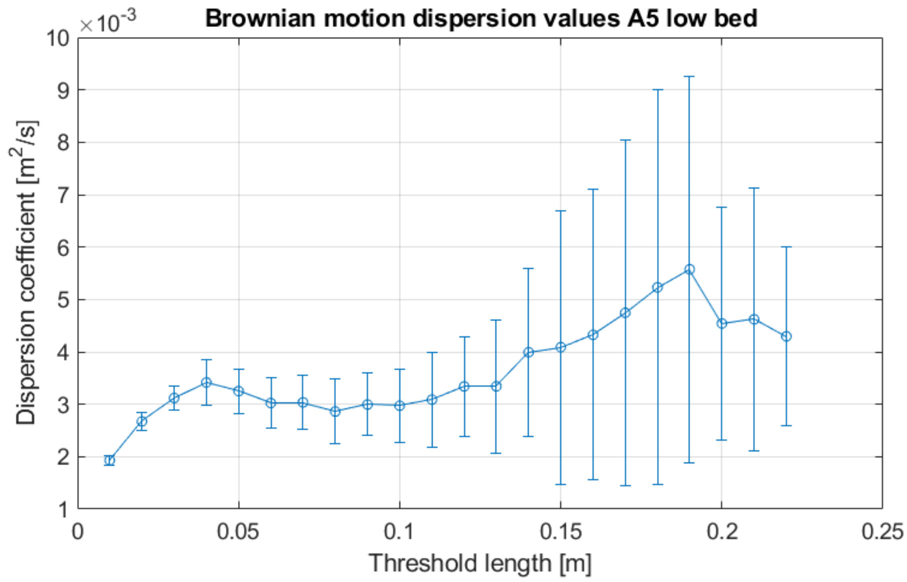

Figure I.5: Brownian motion dispersion values with 95% confidence intervals for A4 at low bed height.

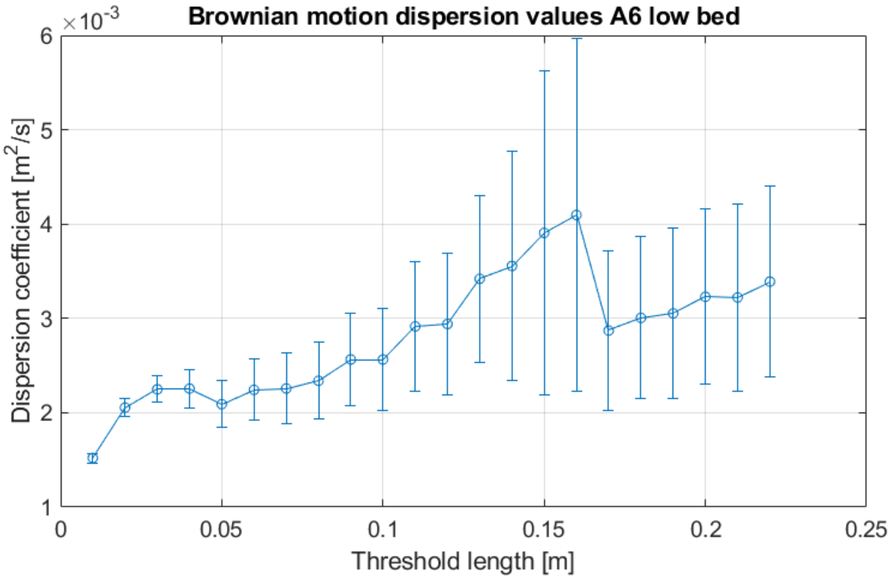

Figure I.6: Brownian motion dispersion values with 95% confidence intervals for A4 at low bed height.

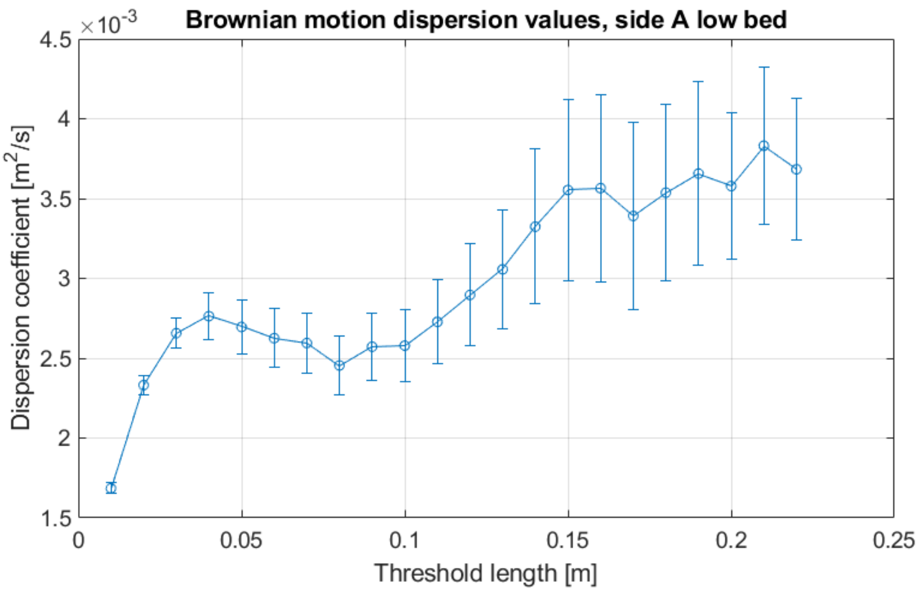

Figure I.7: Brownian motion dispersion values with 95% confidence intervals for all data on side A at low bed height.

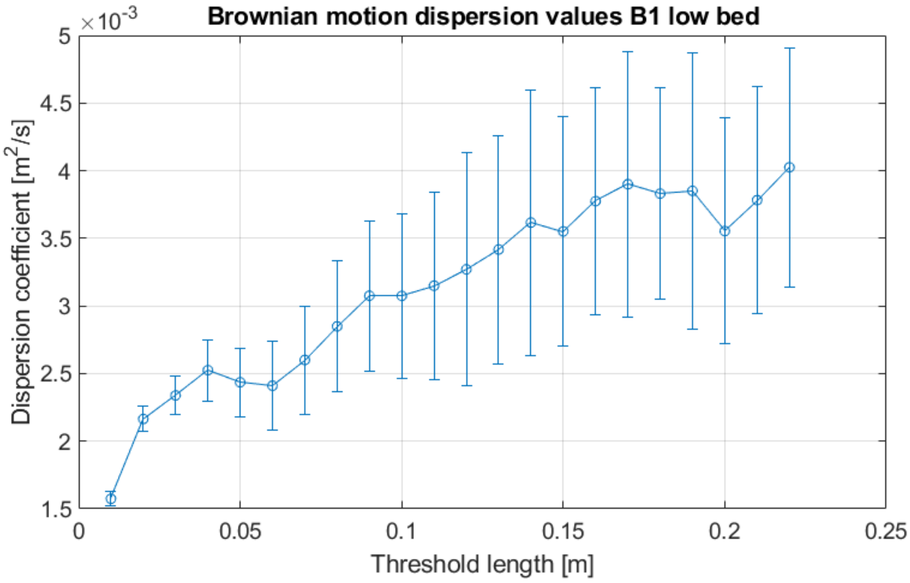

Figure I.8: Brownian motion dispersion values with 95% confidence intervals for B1 at low bed height.

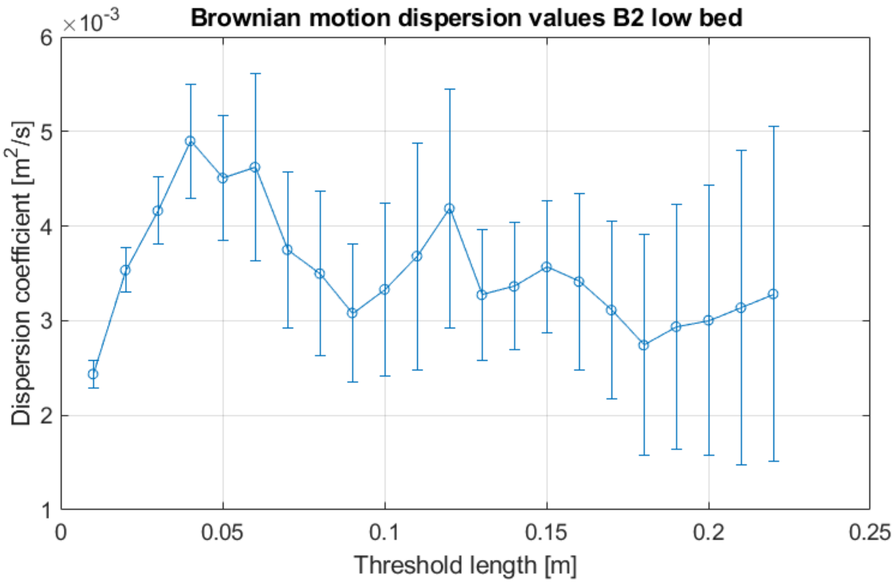

Figure I.9: Brownian motion dispersion values with 95% confidence intervals for B2 at low bed height.

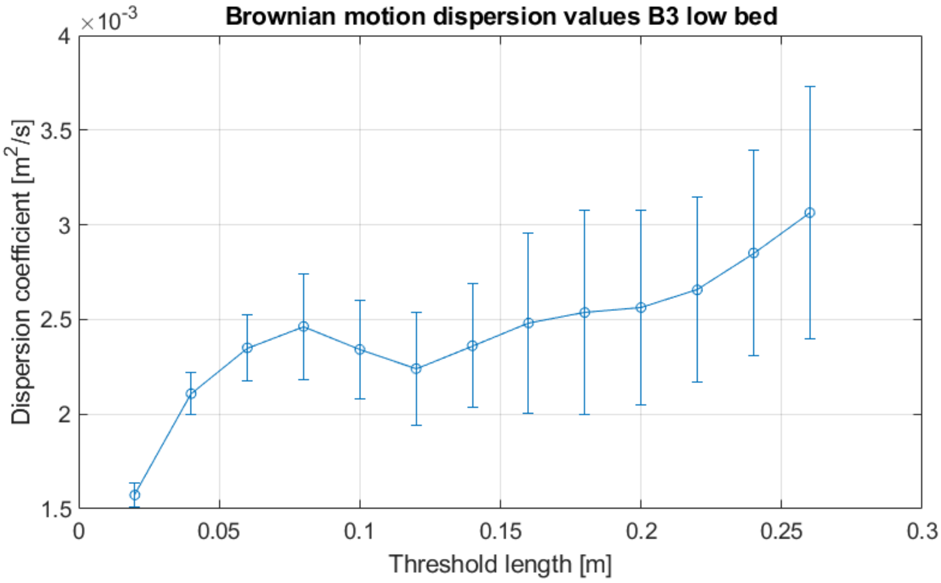

Figure I.10: Brownian motion dispersion values with 95% confidence intervals for B3 at low bed height.

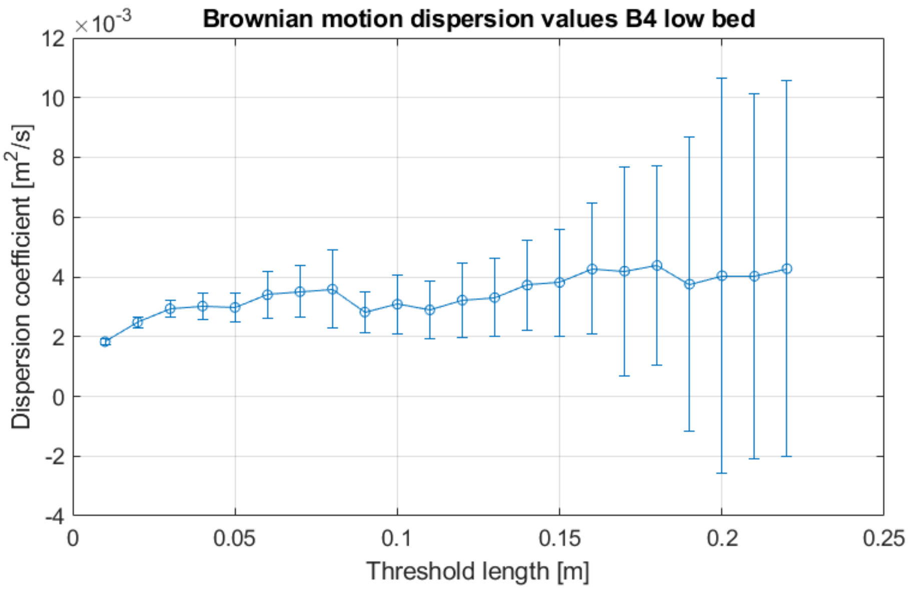

Figure I.11: Brownian motion dispersion values with 95% confidence intervals for B4 at low bed height.

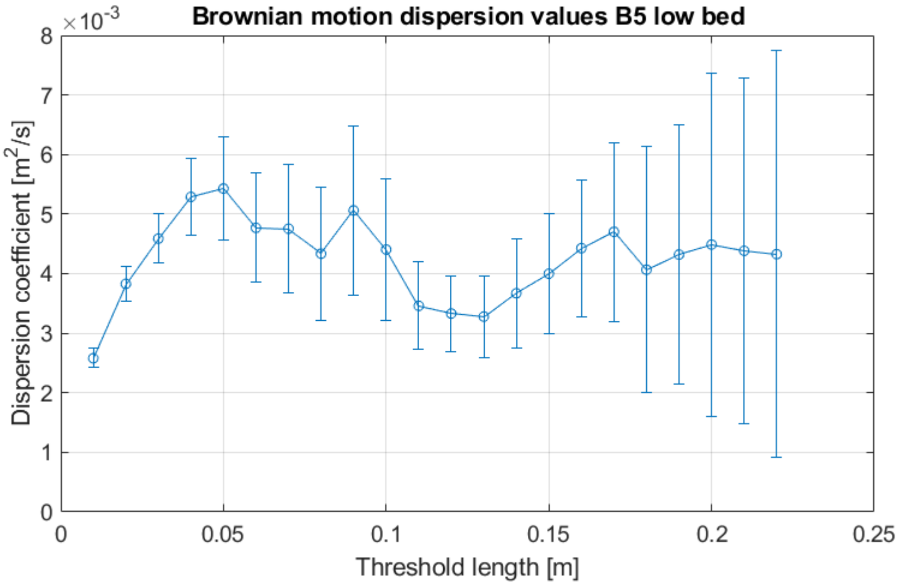

Figure I.12: Brownian motion dispersion values with 95% confidence intervals for B5 at low bed height.

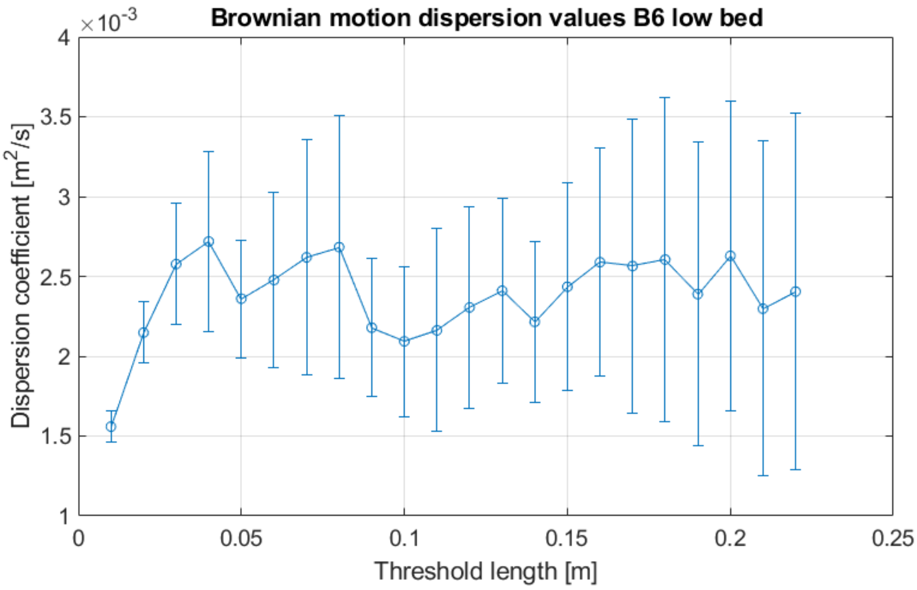

Figure I.13: Brownian motion dispersion values with 95% confidence intervals for B6 at low bed height.

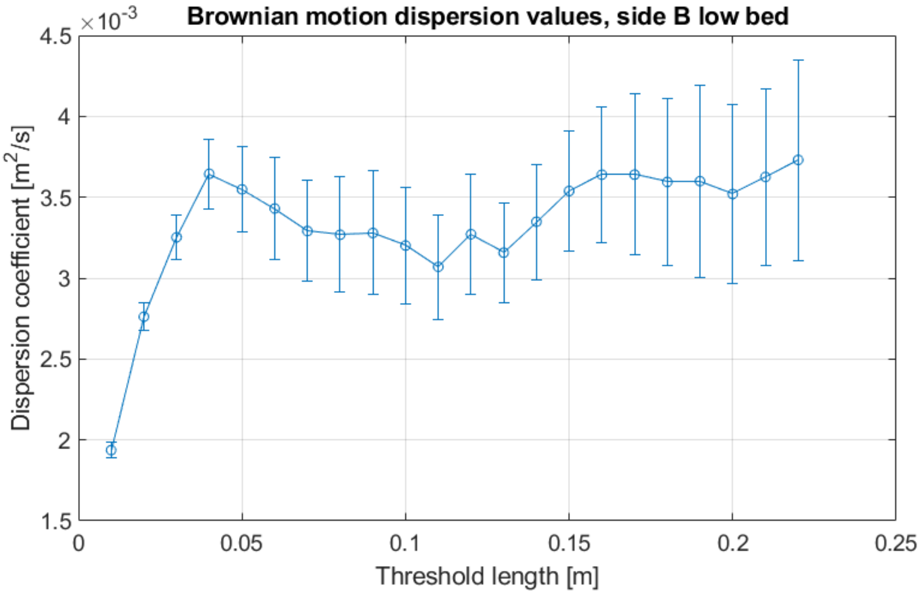

Figure I.14: Brownian motion dispersion values with 95% confidence intervals for all data on side B at low bed height.

J

Confidence intervals for mixing cell calculations for the low bed

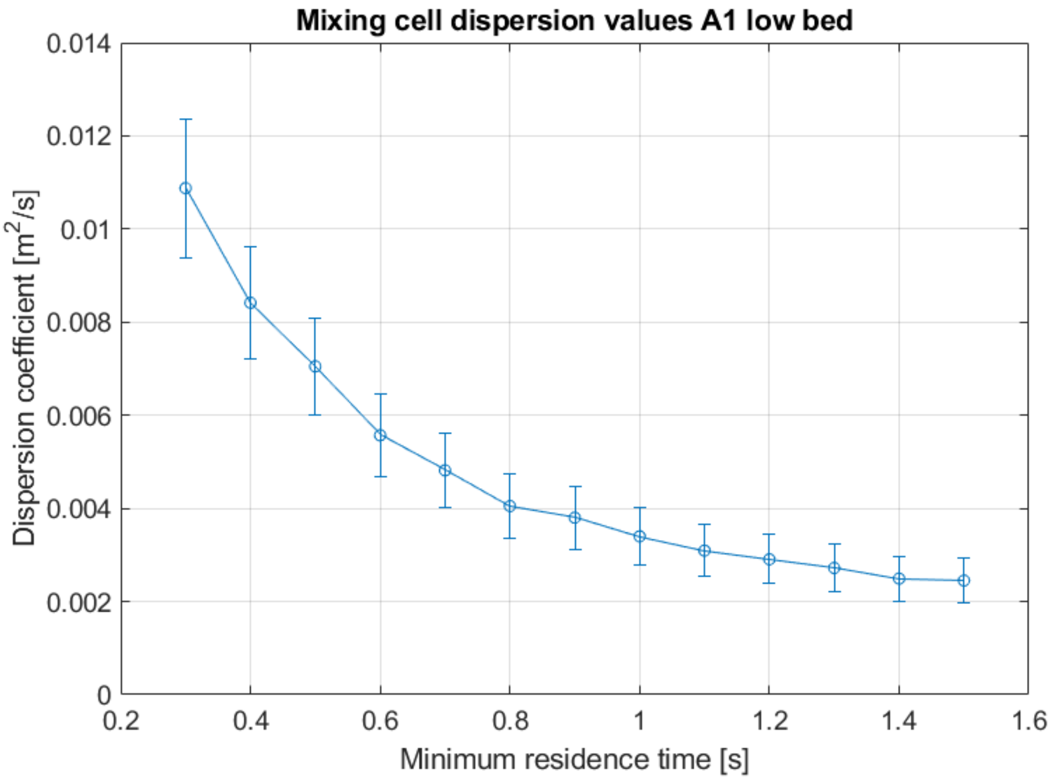

Figure J.1: Mixing cell dispersion values with 95% confidence intervals for A1 at low bed height.

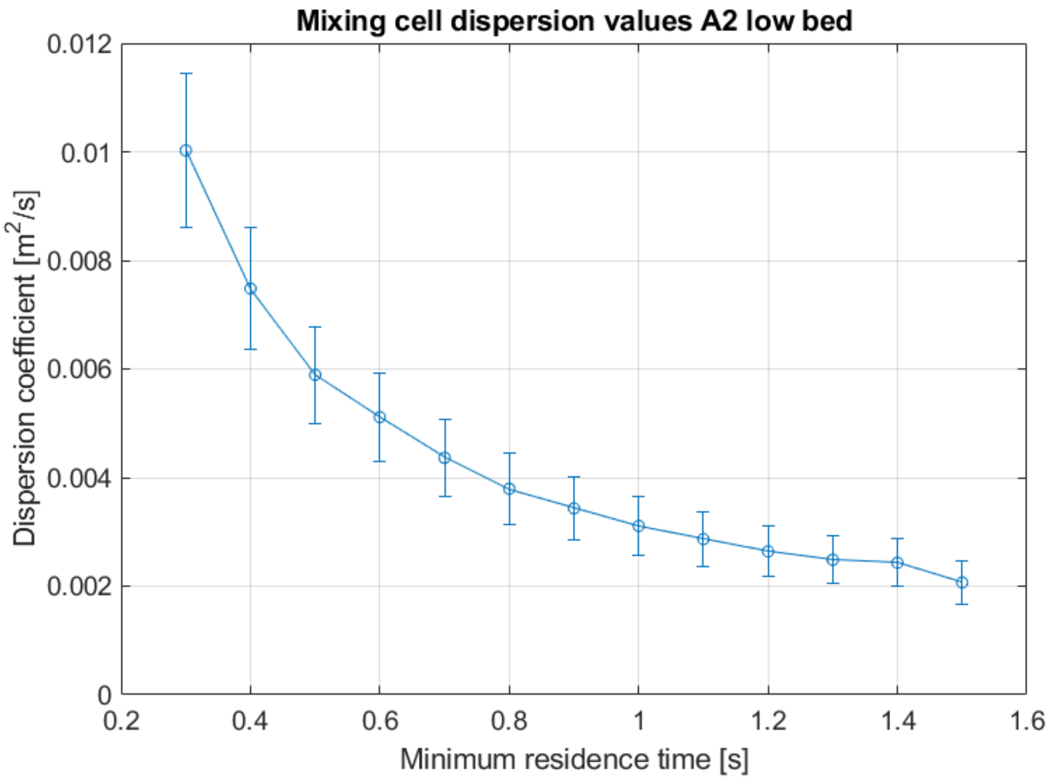

Figure J.2: Mixing cell dispersion values with 95% confidence intervals for A2 at low bed height.

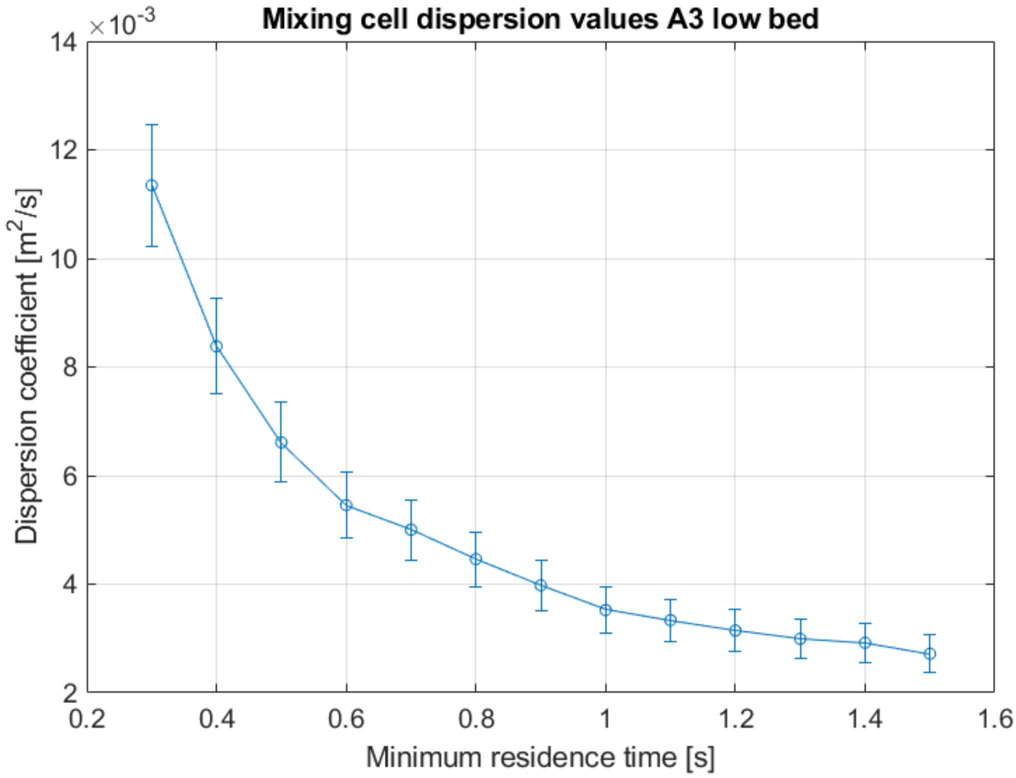

Figure J.3: Mixing cell dispersion values with 95% confidence intervals for A3 at low bed height.

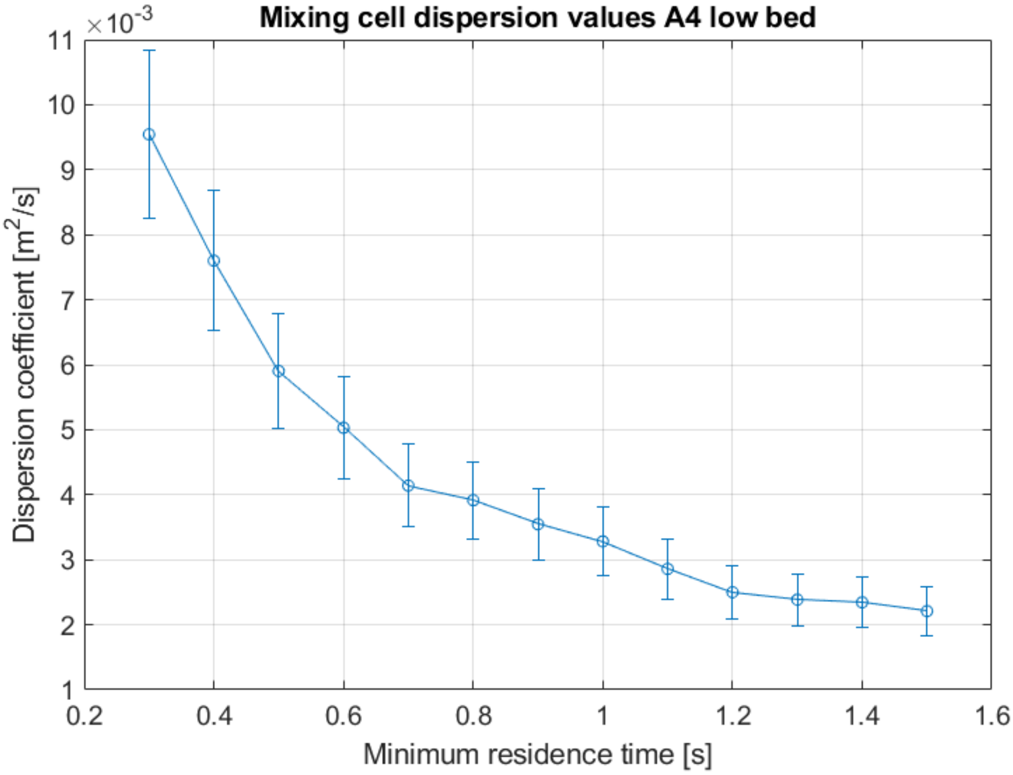

Figure J.4: Mixing cell dispersion values with 95% confidence intervals for A4 at low bed height.

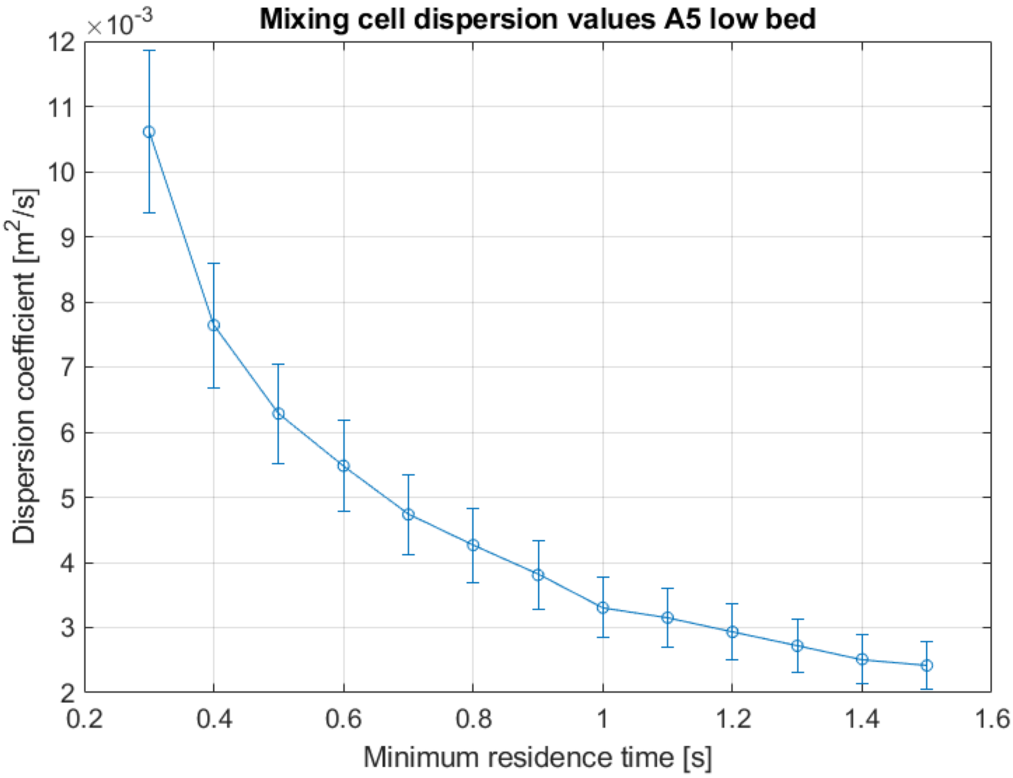

Figure J.5: Mixing cell dispersion values with 95% confidence intervals for A5 at low bed height.

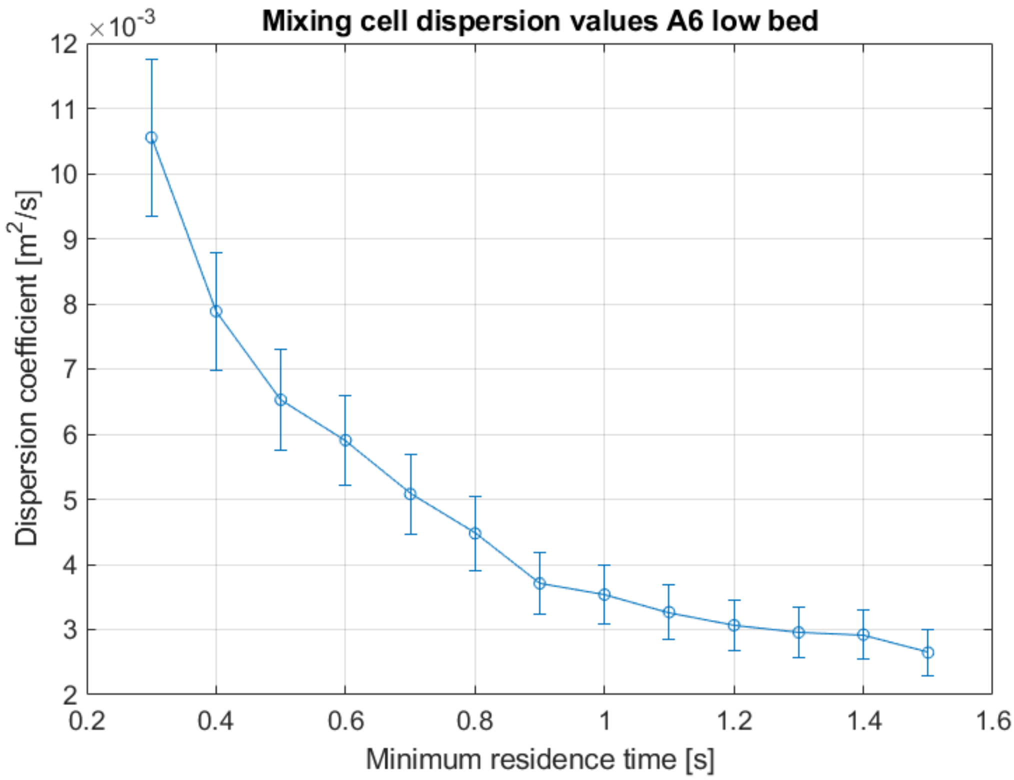

Figure J.6: Mixing cell dispersion values with 95% confidence intervals for A6 at low bed height.

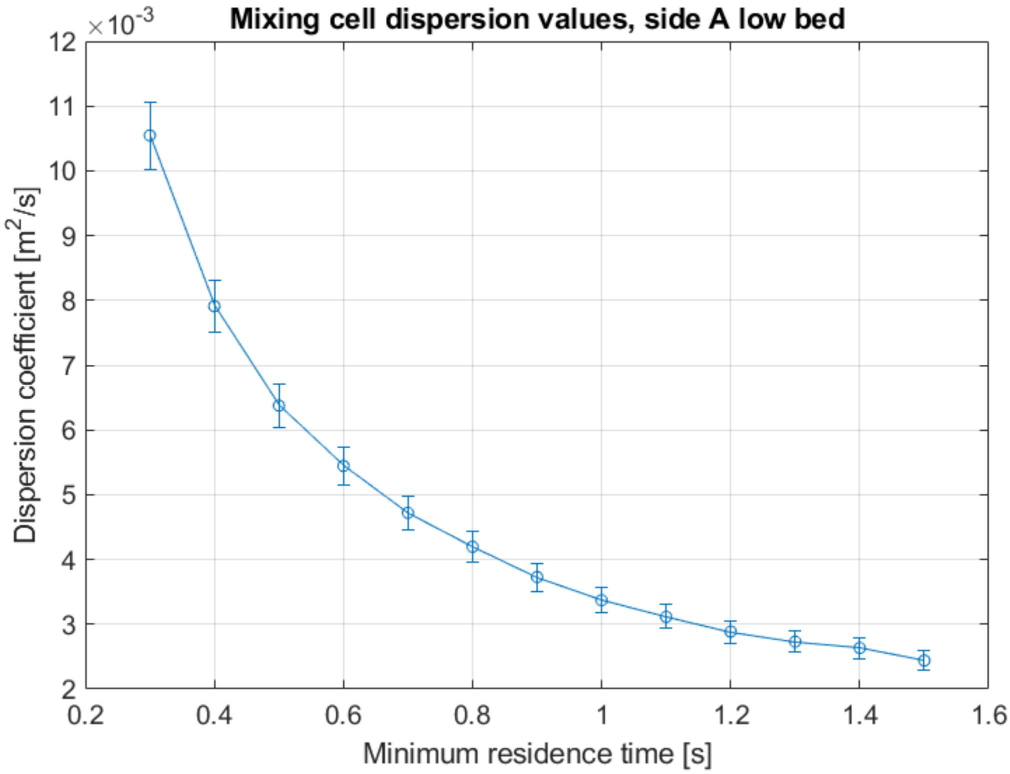

Figure J.7: Mixing cell dispersion values with 95% confidence intervals for all data on side A at low bed high.

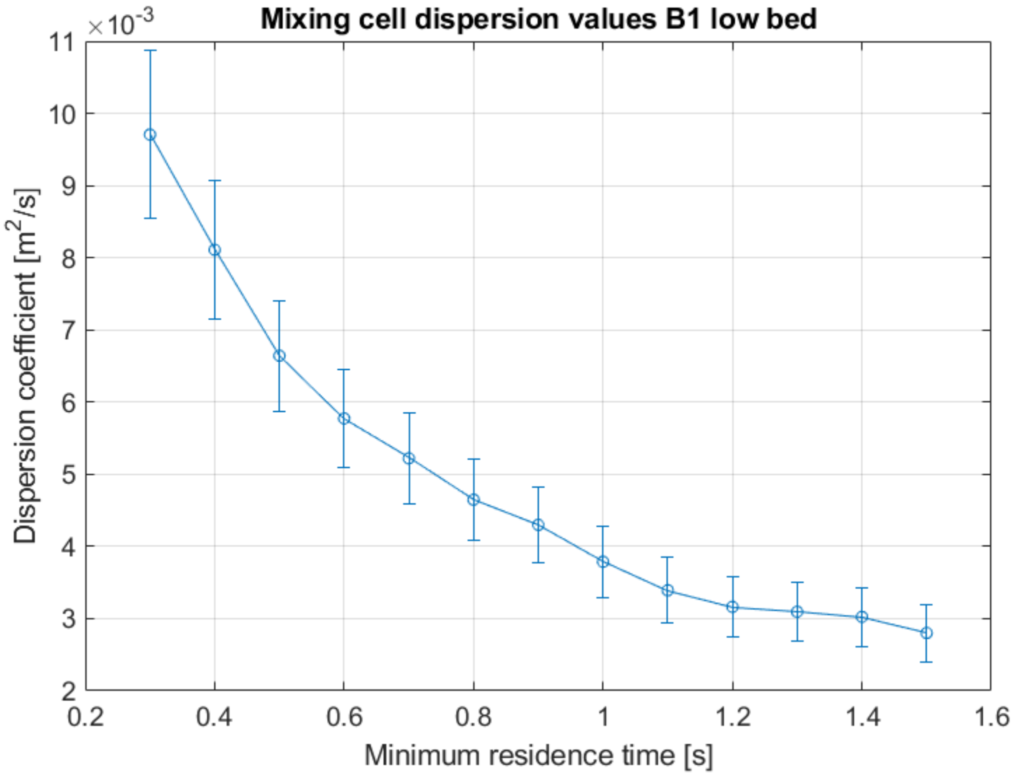

Figure J.8: Mixing cell dispersion values with 95% confidence intervals for B1 at low bed height.

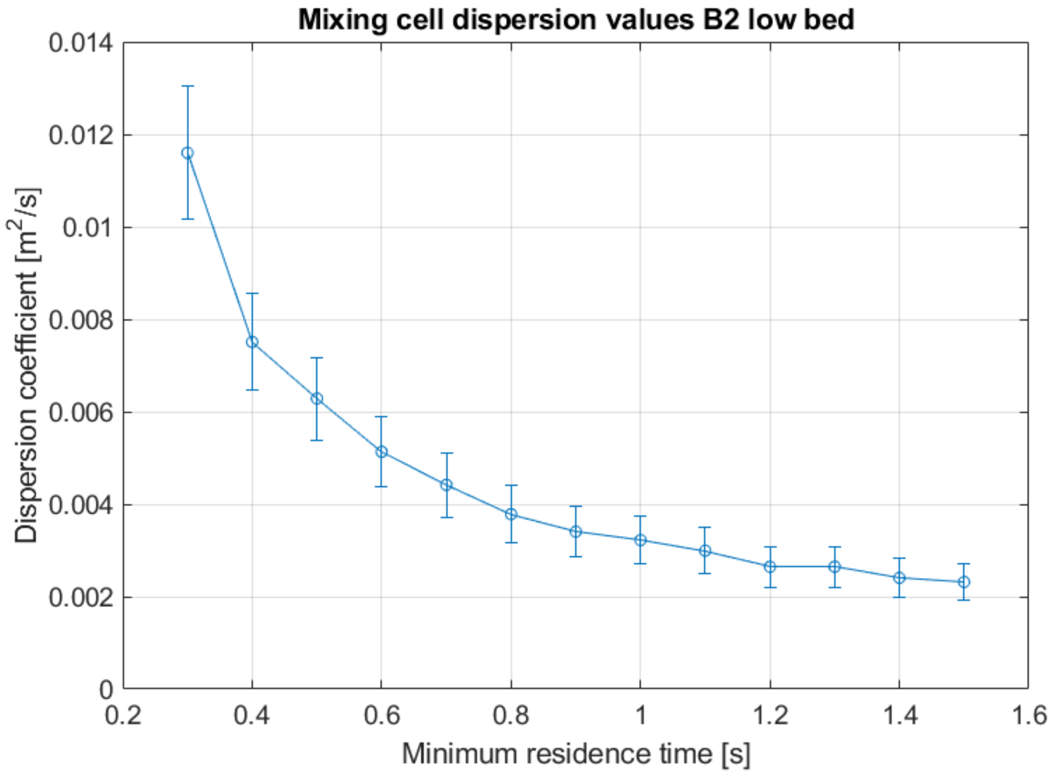

Figure J.9: Mixing cell dispersion values with 95% confidence intervals for B2 at low bed height.

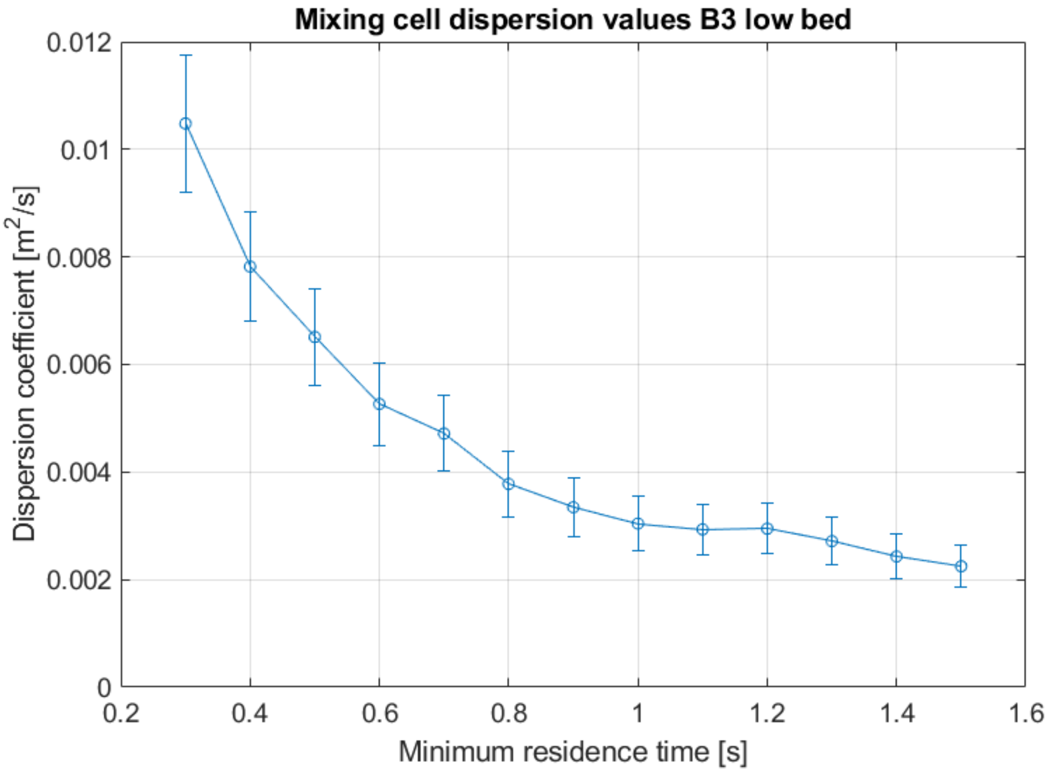

Figure J.10: Mixing cell dispersion values with 95% confidence intervals for B3 at low bed height.

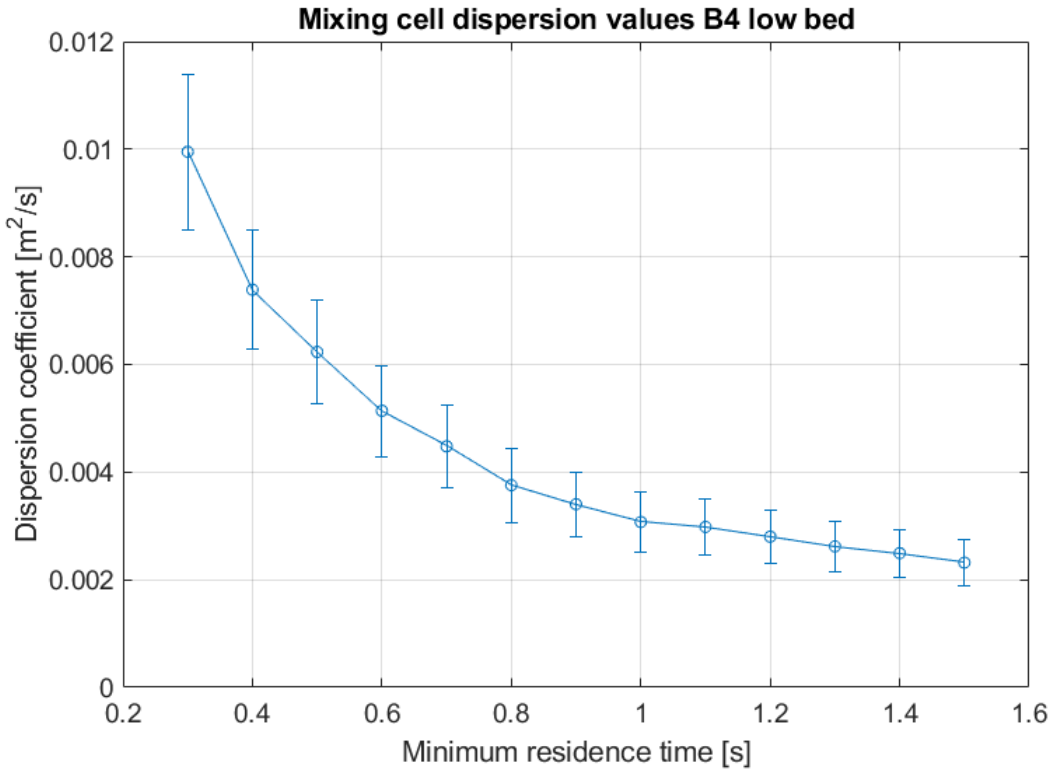

Figure J.11: Mixing cell dispersion values with 95% confidence intervals for B4 at low bed height.

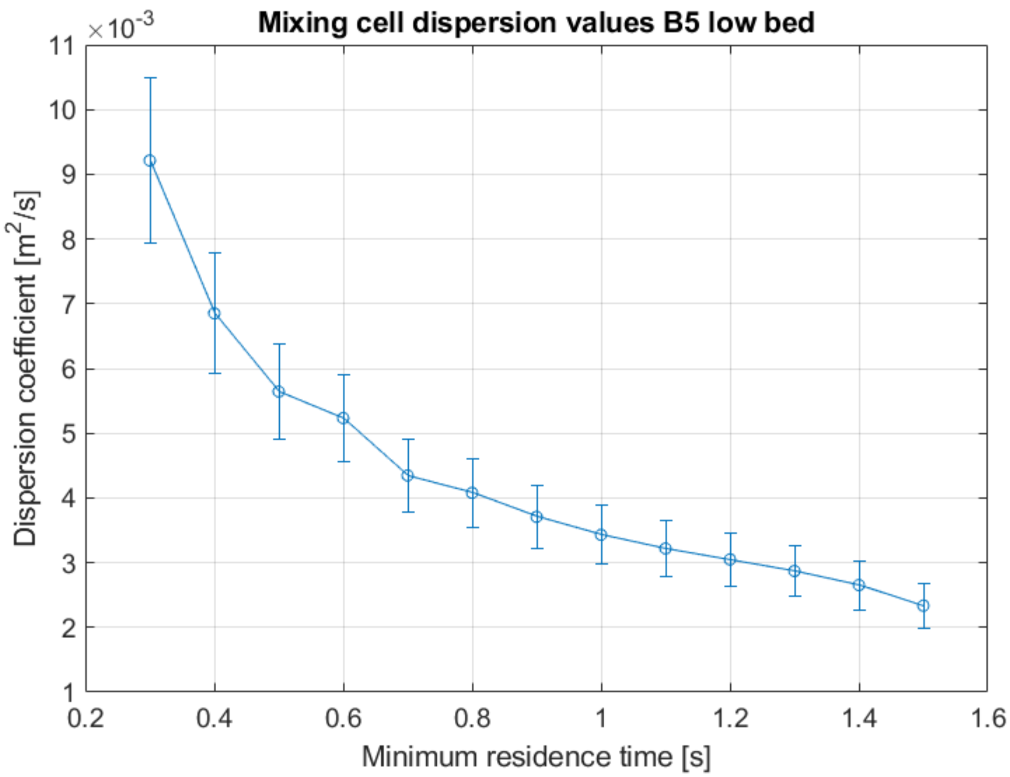

Figure J.12: Mixing cell dispersion values with 95% confidence intervals for B5 at low bed height.

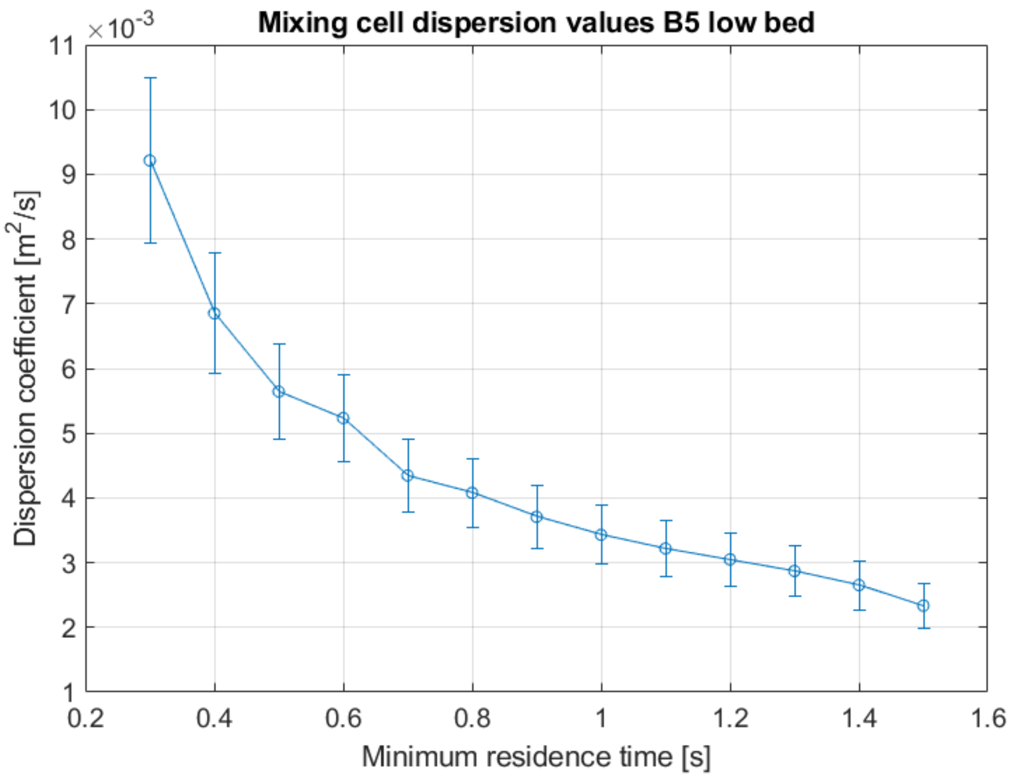

Figure J.13: Mixing cell dispersion values with 95% confidence intervals for B5 at low bed height.

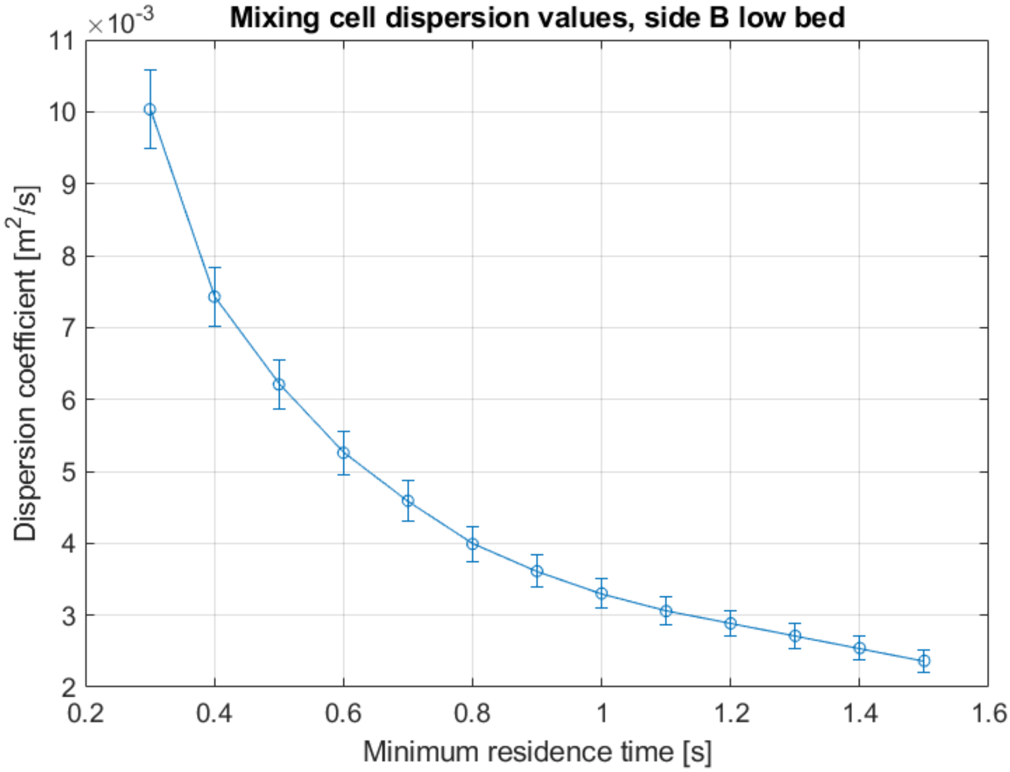

Figure J.14: Mixing cell dispersion values with 95% confidence intervals for all data on side B at low bed height.

DEPARTMENT OF SOME SUBJECT OR TECHNOLOGY
CHALMERS UNIVERSITY OF TECHNOLOGY
Gothenburg, Sweden
www.chalmers.se

AVANCEZ
1829

CHALMERS
UNIVERSITY OF TECHNOLOGY